FABRICATION OF DNA/RNA TEMPLATED CONDUCTIVE METAL WIRES FOR DYE-SENSITIZED SOLAR CELL APPLICATIONS

SEHAR SHAKIR

FACULTY OF SCIENCE
UNIVERSITY OF MALAYA
KUALA LUMPUR

2018

FABRICATION OF DNA/RNA TEMPLATED CONDUCTIVE METAL WIRES FOR DYE-SENSITIZED SOLAR CELL APPLICATIONS

SEHAR SHAKIR

THESIS SUBMITTED IN FULFILMENT OF THE REQUIREMENTS FOR THE DEGREE OF DOCTOR OF PHILOSOPHY

DEPARTMENT OF PHYSICS
FACULTY OF SCIENCE
UNIVERSITY OF MALAYA
KUALA LUMPUR

2018

UNIVERSITY OF MALAYA

ORIGINAL LITERARY WORK DECLARATION

Name of Candidate: **Sehar Shakir**

Registration/Matric No: **SHC140064**

Name of Degree: **Doctor of Philosophy**

Title of Thesis:

FABRICATION OF DNA/RNA TEMPLATED CONDUCTIVE METAL WIRES FOR DYE-SENSITIZED SOLAR CELL APPLICATIONS

Field of Study: EXPERIMENTAL PHYSICS

I do solemnly and sincerely declare that:

(1) I am the sole author/writer of this Work;
(2) This Work is original;
(3) Any use of any work in which copyright exists was done by way of fair dealing and for permitted purposes and any excerpt or extract from, or reference to or reproduction of any copyright work has been disclosed expressly and sufficiently and the title of the Work and its authorship have been acknowledged in this Work;
(4) I do not have any actual knowledge, nor do I ought reasonably to know that the making of this work constitutes an infringement of any copyright work;
(5) I hereby assign all and every right in the copyright to this Work to the University of Malaya ("UM"), who henceforth shall be the owner of the copyright in this Work and that any reproduction or use in any form or by any means whatsoever is prohibited without the written consent of UM having been first had and obtained;
(6) I am fully aware that if in the course of making this Work, I have infringed any copyright whether intentionally or otherwise, I may be subject to legal action or any other action as may be determined by UM.

Candidate's Signature Date:

Subscribed and solemnly declared before,

Witness's Signature Date:

Name:

Designation:

FABRICATION OF DNA/RNA TEMPLATED CONDUCTIVE METAL WIRES FOR DYE-SENSITIZED SOLAR CELL APPLICATIONS

ABSTRACT

In this work, fabrication of deoxyribonucleic acid (DNA) and ribonucleic acid (RNA) templated metal wires on substrates were presented and their use as modified counter electrode (CE) in dye sensitized solar cells (DSSCs) has been studied. This research demonstrates a novel and controllable scribing method to fabricate DNA/RNA templated submicron to nanoscale metal wires employing natural capillary force action and the coffee-ring effect. Cyclic voltammetry (CV) measurements showed that DNA/RNA templated metal wires on Si, ITO and Platinum (Pt)/ITO substrates exhibited higher electro-catalytic activity with improved conductivity than conventional Pt/ITO CEs due to the synergistic effect of Pt and metal wire network on ITO. DSSCs designed using TiO_2 photoanode, N719 dye, I^-/I_3^- electrolyte and modified electrodes show higher power conversion efficiency under AM 1.5, 100 $mWcm^{-2}$ illumination compared to cells assembled using the same parameter but conventional (Pt/ITO) CE. Moreover, to enhance photoabsorption and electron generation in DSSCs and to develop compatible photoanodes with our modified CEs, TiO_2-based photoanodes were developed using aerosol-assisted chemical vapor deposition (AACVD) and electrophoretic deposition (EPD). The effect of magnesium doping in AACVD developed films at various concentrations and surface modification of EPD films using tin (Sn) were analyzed. A detailed morphological and structural analysis of the films developed using AACVD and EPD has been presented. The overall efficiency improvements were observed when the modified CEs and modified photoanodes were used. Various characterization techniques were employed to analyze the fabricated metal wires and deposited TiO_2 electrodes including X-ray diffraction for phase purity, crystallinity and crystallite size determination, X-ray photon spectroscopy for determination of valence state of the metal

wires, CV for determination of catalytic activity of the CEs, current density-voltage (J-V) characteristics for analyzing the performance of the DSSCs etc. Various DSSCs were formed and the maximum efficiency of 6.68 % was achieved in DSSC fabricated using DNA templated Au wires on Pt/ITO substrates as CE and 2 mol% Mg doped AACVD TiO_2 film on ITO as photoanode.

Keywords: DNA/RNA templating, Scaffolding, DSSCs, Photonaode, Counter electrode.

FABRIKASI DNA / RNA WAYAR KONDUKTIF LOGAM TEMPA UNTUK APLIKASI PEWARNA SEL SOLAR SENSITIF

ABSTRAK

Dalam kerja ini, fabrikasi DNA/RNA templat dibuat pada wayar logam di atas silikon (Si) dan substrat indium besi oksida (ITO) telah dibentangkan dan penggunaannya sebagai elektrod balas diubahsuai (CE) dalam sel solar dye sensitif (DSSCs) telah dikaji. Pengukuran voltammetri kitaran (CV) menunjukkan bahawa dawai logam templat DNA/RNA pada substrat Si, ITO dan Platinum(Pt)/ITO memperlihatkan aktiviti elektro-katalitik yang lebih baik dengan kekonduksian yang lebih tinggi daripada elektrod balas Pt/ITO konvensional kerana kesan sinergi Pt dan rangkaian wayar logam pada ITO. DSSC yang direka menggunakan TiO_2 photoanode, N719 pewarna, I^-/I_3^- elektrolit dan elektrod yang diubahsuai menunjukkan kecekapan penukaran kuasa yang lebih tinggi di bawah pencahayaan AM 1.5, 100 $mWcm^{-2}$ berbanding dengan sel yang dipasang menggunakan parameter yang sama tetapi konvensional (Pt/ITO) CE. Tambahan pula, untuk meningkatkan penyeropan foto dan generasi electron di DSSCs dan untuk membangunkan fotoanod yang serasi dengan CE yang diubah suai, fotoanod berasaskan TiO_2 telah dibangunkan menggunakan pemendapan wap kimia yang dibantu aerosol (AACVD) dan pemendapan electrophoretik (EPD). Kesan doping magnesium dalam filem AACVD yang dibangunkan di pelbagai kepekatan dan pengubahsuaian permukaan filem EPD menggunakan besi (Sn) dianalisis. Analisis morfologi dan struktur terperinci bagi filem-filem yang dibangunkan menggunakan AACVD dan EPD telah dibentangkan. Peningkatan kecekapan keseluruhan diperhatikan apabila elektrod balas dan fotoanod diubahsuai digunakan. Pelbagai teknik pencirian digunakan untuk menganalisis wayar logam fabrikasi dan elektrod TiO_2 yang didepositkan termasuk pembelahan sinar-X untuk ketulenan fasa, kristalografi dan penentuan saiz kristal, spektroskopi photon X-ray bagi penentuan keadaan valensi wayar logam, CV untuk penentuan pemangkin aktiviti CE,

ciri-ciri kepadatan axis-voltan (J-V) untuk menganalisis prestasi DSSC dan sebagainya. Pelbagai DSSC telah ibinadan kecekapan maksimum sebanyak 6.68 % telah dicapai dalam DSSC yang direka menggunakan wayar Au di atas Pt/ITO DNA sebagai CE dan 2 mol% Mg doped AACVD TiO_2 filem pada ITO sebagai fhotoanod.

Kata kunci: Templat DNA/RNA, Scaffold, DSSC, Fotonaode, Elektrod balas.

ACKNOWLEDGEMENTS

All praises are to Allah Almighty, who is the creator of this world. It's all due to His blessings that enabled me to work and successfully complete my research. To my supervisor, Assoc. Prof. Dr. Vengadesh Periasamy, please accept my overwhelmed and sincere gratitude for accepting me as your PhD student. No words can express your support and constant help to achieve my dream. I feel blessed to have a supervisor like him. He has helped me with his expertise, support, directions, guidance, kindness, unlimited assistance, motivation and his keen attention.

To my parents and my parents in law for playing a vital role and standing by my side with their endless encouragement. Thank you for your encouragement and your support. My husband, who has always understood me, encouraged me and became my support system. Thank you for understanding me during my worst days. My sisters, my nephew and my niece for supporting me with their laughter, their kind love and care. I am indebted to all of you.

I deem it my utmost pleasure to avail this opportunity to express the heartiest gratitude and a deep sense of obligation to the head of the department and all professors of the Physics department, especially Prof. Dr. Hasan Abu Kassim, Assoc. Prof. Dr. Ramesh Kasi and Dr. Goh Boon Tong, for the technical and academic support. I am thankful to Dr. Kamran Yunus, Department of Chemical Engineering and Biotechnology, University of Cambridge, UK, for his guidance and technical support. I gladly express my regards to Dr. Gnana Kumar, Department of Physical Chemistry, Madurai-Kamaraj University, Madurai, India for his sincere support. I am thankful for the support and help of my research mates, Nastaran, Sara, Siti, Mus, Yiing Yee and Afsaneh.

TABLE OF CONTENTS

LIST OF FIGURES

LIST OF TABLES

LIST OF SYMBOLS AND ABBREVIATIONS

Å	:	Angstrom
α	:	alpha
β	:	beta
Ω	:	Ohm (Resistance)
θ	:	Reflection angle (Theta)
τ	:	tau
λ	:	Wavelength
AACVD	:	Aerosol assisted chemical vapor deposition
AFM	:	Atomic force microscopy
BET	:	Brunauer–Emmett–Teller
BJH	:	Barrett-Joyner-Halenda
CB	:	Conduction band
CE	:	Counter electrode
CV	:	Cyclic voltammetry
DNA	:	Deoxyribonucleic acid
DSSC	:	Dye sensitized solar cells
E	:	Energy
e^-	:	Electron
E.g	:	Exempli gratia
EDX	:	Energy dispersive X-ray
EPD	:	Electrophoretic deposition
E_g	:	Band gap
eV	:	Electron volt
FESEM	:	Field emission scanning electron microscopy
FTIR	:	Fourier transform infrared
FTO	:	Fluorine tin oxide
ITO	:	Indium tin oxide
HUMO	:	Highest unoccupied molecular orbital
IR	:	Infrared
J	:	Current density
min	:	minute
mL	:	milliliter
mM	:	millimolar

mol	:	mole
mp	:	melting point
nm	:	nanometer
NPs	:	Nanoparticles
rct	:	charge transfer resistance
RNA	:	Ribonucleic acid
UV	:	Ultraviolet
V	:	Voltage
VB	:	Valence band
Vis	:	Visible
XPS	:	X-ray photoelectron spectroscopy
XRD	:	X-ray diffraction

CHAPTER 1: INTRODUCTION

1.1 Background of Study

1.1.1 Sub-Micron to Nanoscale Metal Wires on Substrates

The fabrication of sub-micron to nanoscale materials depend on the reaction, assembly and growth of metal atoms, clusters or molecules to form one dimensional (1-D), two dimensional (2-D) or three dimensional (3-D) materials. Sub-micron to nanoscale materials are characterized by their sizes and number of dimensions. A sub-micron size material is defined as material with size less than a micron (<1 μm) and a nanosize material is defined as material with size less than 100 nm (1-100 nm) in at least one spatial direction (Bai et al., 2017; Cao, 2004). There is remarkable difference in the properties of materials in their bulk phase and their nanometer scale counterparts (Moras et al., 1996). The sub-micron to nanometer scale material exhibit unexpected properties for a range of 0-D, 1-D and 2-D (Cheng et al., 2009; N. Wang et al., 2008). Electrical, chemical and optical properties remain almost the same for a bulk material, but when the material is reduced to sub-micron to nanoscale regime (1-500 nm), these properties are highly influenced by the size of the material and hence these properties can be tuned due to their size dependence.

There are two main factors responsible for the dependence of material properties on its size; the electronic band structure quantization and the surface to volume ratio (corresponds to the atoms residing on the surface) (Dey et al., 2015; Ehira & Egami, 1995; Roduner, 2006). As the size is reduced, electronic band quantization and surface to volume ratio increases, thereby, influencing the physio-chemical properties of sub-micron to nanoscale materials. The atoms in the bulk are less energetic than the atoms on the surface because atoms in bulk have higher coordination number and are strongly bound to the lattice as compared to atoms on the surface. For example, the melting

temperature of bulk metal materials is higher than that of their sub-micron to nanoscale counterparts. This is because with the decrease in size, surface to volume ratio increases, thereby, increasing the surface tension due to the presence of high energy surface atoms. This favors the conversion of solid into liquid phase hence, lowering the melting temperature (Dey et al., 2015).

To explain the electronic band structure quantization (quantum confinement), it is important to classify electronic structures of insulators, semiconductors and bulk metals. A schematic illustration of electronic structures is shown in Figure 1.1. The valence band (VB) and conduction band (CB) of solids are akin to the HOMO (highest occupied molecular orbital) and LUMO (lowest unoccupied molecular orbital) of a molecule. The VB is the highest occupied electronic state of the material and the CB is the next available state for the electron after valence band is totally filled. The energy difference between the empty CB and a filled VB is called the band gap (E_g) of the material. When the E_g is too high, it is difficult for an electron to overcome this energy to reach to the CB and such a material is an insulator (no free electron movement). If E_g is small enough that some electrons can overcome and move to the CB, such a material is a semiconductor. In a metal, the band gap doesn't exist or is too small and the electrons are free to move between CB and VB thereby, conducting electricity. As the material is scaled down from bulk to sub-micron to nanoscale size, a corresponding change in electronic energy level spacing occurs. For example, modifying the structure of CdS nanoparticles can lead to the tuning of electronic structure of material. By maneuvering the size of CdS nanoparticles from 2 to 5 nm, the band gap could be adjusted from 4.5 to 2.5 eV (Moras et al., 1996). The change is illustrated in Figure 1.2. Electronic structure of sub-micron to nanoscale materials is somewhere between the molecular band and bulk structures. The band structure is not continuous in sub-micron to nanoscale materials.

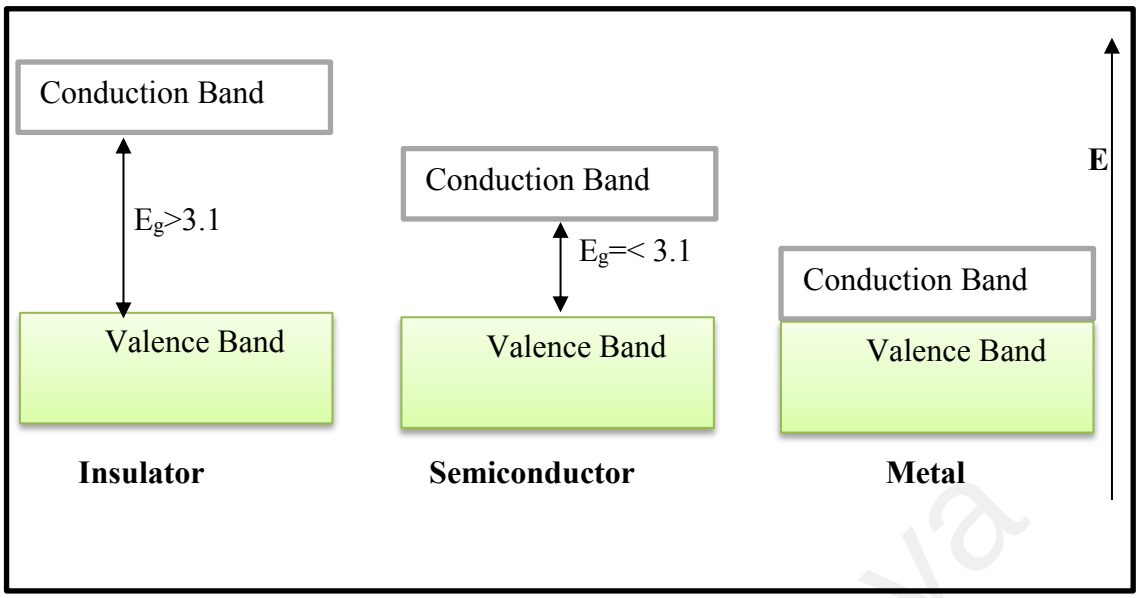

Figure 1.1: Schematic illustration of electronic structure of solids. The VB is filled with electrons and the CB is partially filled for semiconductors and metals. CB is empty for insulator due to high energy gap.

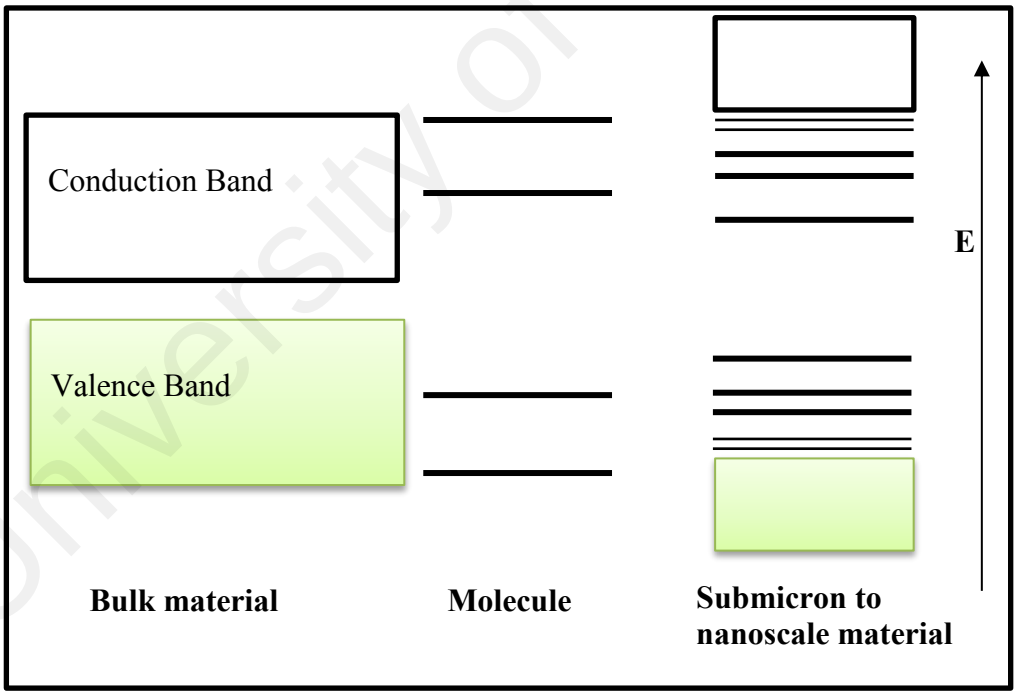

Figure 1.2: Schematic illustration of change in band structure. Formation of discrete energy levels in submicron to nanoscale materials on structure quantization.

Another important factor affecting the properties of the materials is the shape and structure of the material. In the end of 19th century, significant influence of fine structure on the properties of materials was observed with the work on mechanical properties of iron (Fe) alloys (Gleiter, 1992). It was observed that allotropic transformation of Fe alloys formed fine scale microstructure giving the alloy its hardness. Correlation between properties and microstructure was then observed for non-ferrous materials as well. The mechanism of the correlation was investigated after high resolution characterization techniques like field ion and electron microscopy became available. Another breakthrough happened with the development of nanomaterials when it was observed that new electronic and atomic structures were generated with modifications in the structure of the solids (Kvítek et al., 2013). For example, Narayanan et al. (2004) observed that the catalytic activity varied for differently shaped Platinum (Pt) nanocrystals (tetrahedral, near spherical and cubic) (Narayanan & El-Sayed, 2004).

So far we have discussed the correlation of shape and size of the materials on its properties. The size and structure of materials can be tailored for a particular application, e.g. materials based on nanowires, quantum dots and quantum wells, etc. In this research, the work was focused on the fabrication of nucleic acid templating of conducting sub-micron to nanoscale size metal wires for applications in Dye Sensitized Solar Cells (DSSCs). In order to prepare conductive metal wires, size scaling may become detrimental beyond a certain limit as conductivity is reduced with a reduction in the number of charge carriers. The drive is; (a) to understand fabrication and growth of metal wires using DNA and RNA templating and the coffee-ring effect, (b) to fabricate the metal wires in submicron to nanoscale regime retaining bulk-like properties of the metal wires, (c) to use the fabricated metal wires on various substrates as modified CEs in DSSCs and (d) to analyze the performance of the CEs and their respective DSSCs.

1.1.2 Template based Synthesis and DNA as a Nanomaterial

Template based synthesis became a research interest when Martin's group reported the pioneering work of metal microtubule synthesis by templating in 1994 (Brumlik et al., 1994; Martin, 1994). There are various templates available for the fabrication of metal wires (Reyes et el., 2016). Recently, biomolecules like self-assembled proteins, viruses, bacteria etc. have emerged as fascinating bio-templates due to their sophisticated chemistries and special structural features, which are advantageous and beneficial characteristics for novel sub-micron to nanoscale material development (Gazit, 2007; Niu et al., 2007). Bio-template synthesis involves the use of biological building blocks as biological tools, templates and scaffolds for fabricating various non-biological nanostructures (Taton, 2003). Among these bio-templates, DNA molecules hold much importance as a template from the material science point of view. Seeman et al. (1998) reported that complementary DNA strands possessed specific recognition which allowed their arrangement into well-arranged structures at nanoscale (Seeman, 1998, 2005). The polynucleotide chain of DNA has a length of 0.34 nm per nucleoside subunit and a diameter of 2 nm. Moreover, DNA molecules are chemically robust and due to their increased demand in molecular biology applications, the cost of synthesis of DNA has significantly reduced. It has been reported in literature that DNA-templated metallic nanowires tend to have different structural properties from nanowires fabricated by other techniques (Gu et al., 2005). These characteristics of DNA make them an interesting nanomaterial and bio-template for fabrication of metal structures.

RNA and DNA molecules have many common structural properties and RNA had been studied as a bio-template (Eber et al., 2015; Kumar & Gupta, 2017; Tsukamoto, Muraoka et al., 2007). However, no work on the RNA templated fabrication of metal wires has been reported before.

1.2 Industrial Applications

As explained earlier, the structure shape and size of wires highly affect material properties and hence their applications. The structure of metal wires offers very little room for defects allowing unimpeded flow of electrons (Mikolajick et al., 2013). The diameters of nanowires are negligible, however, their lengths could be maneuvered to hundreds of micrometers. Only known materials possessing such extreme diameter to length ratios are the nanowires making them unique. Facile and economical fabrication of metal nanowires can open doors for new generation nano-electronics. Controllable writing methods of metal nanowire fabrication could enable fabrication of microchips and revolutionize nano-circuit manufacturing. Such circuits could have numerous industrial applications apart from solar cell applications e.g. nanowires for the development of super capacitors and flexible capacitors for wearable electronics as energy storage provider (Zhou et al., 2015). Piezoelectric nano-generators and sensors powered by zinc oxide nanowires could allow development of self-contained and small sensors which can be driven employing mechanical energy like win or tides (Wang et al., 2006).

Nanowires, owing to a resonance effect, can concentrate sunlight enabling more photons of sunlight to electricity conversion producing highly efficient solar cells (Kupec et al., 2010). Moreover, employing self-assembly techniques to arrange nanowires on a substrate such as semiconducting nanowire on gold nanoparticles can replace Si based substrates. Battery anodes fabricated using silicon nanowires on stainless steel substrates could show power density more than 10 times as compare to the power density of conventional lithium ion batteries. The replacement of bulk Si with Si nanowires solves the problem of Si cracking on electrodes (Chan et al., 2008). Controlled writeable nanowires can be used to build transistors without p-n junction, dense memory devices, nano-robots for medical purposes to deliver medicine to the narrowest areas of the body (Ben-Romhane N et al., 2014; Colinge J. P et al., 2010; Saaeh Y and Vyas D, 2014).

1.3 Application in DSSCs

1.3.1 Drive Towards Renewable Energy

In recent times, energy crisis, greenhouse gas (GHG) emissions and climate change are the most threatening issues for mankind. There is a dire need of adopting new policies that should utilize alternative energy sources rather than fossil fuels and provide sustainable solution to balance the requirement for affordable energy with the pressing issue of climate change. Global warming causes a temperature increase of 0.13 °C per decade. Apart from global warming, there are other adverse effects of the gases formed during burning of fossil fuels e.g. pollution, acid rain, etc. These effects have been mild till now but if the GHG emissions continue at the present rate, the consequences will become severe. Another issue with the use of fossil fuel is its rapid depletion causing it to vanish.

In order to meet present and future energy requirements and to produce clean energy, use of alternative energy resources like solar photovoltaic, solar thermal, biofuels and clean coal technologies should be employed. Among renewable resources, solar energy seems to be an attractive clean energy source that can help to meet our energy requirements and reduce the consequences of global warming. The sun is expected to shine for billions of years, well beyond the existence of Earth. Taking advantage of the abundant solar energy is one of the best ways of reducing the use of fossil fuels and therefore, driving down carbon emissions. Even though solar energy has a large potential to reduce emissions and provide substantial amounts of power to consumers, solar energy is accounted for a very small percentage of the total energy produced by alternative energy sources due to high capital cost. More energy from sun strikes earth in 1 hour (4.3×10^{20} J) than all of the energy consumed by humans in an entire year.

1.3.2 Introduction to Solar Cells

A solar cell is a device that converts solar radiations, with specific wavelengths, into electricity. The concept of a solar cell is related to the discovery of the photoelectric effect. Einstein explained the photoelectric effect in 1905 and received a Nobel Prize in 1921 but it was first discovered by A.E Becquerel in 1839. Photoelectric effect is the phenomenon of generation of photoelectrons or current when a piece of metal is irradiated by light. Light provides photon energy ($h\upsilon$) to the electrons in atoms of the metal which excites them and hence produce the current flowing through the metal (Willett, 2004). After the discovery of photoelectric effect, it took more than 30 years to develop the first semiconductor p-n junction solar cell. This cell was developed by Russel Ohl in 1941 and lead to the development of the first Si solar cell by Chapin in 1957. The cost of these cells was very high with very low efficiency and they were only used in space applications. Negligible attention was given to the discovery of solar cells until 1970 when the world globally faced the oil crisis.

1.3.3 Working Principles of Photovoltaic Cells

Photovoltaic devices work on the phenomena of charge separation occurring at the interface of two different materials. These materials have different conduction mechanism. Solar photovoltaic can be defined as the direct conversion of solar radiation into electric current. The materials that exhibit photoelectric effect absorb energy in the form of photons of light and release free electrons. The separation or flow of these free electrons causes electric current to be generated.

The working of a solar cell can be divided into three simple steps; (1) absorption of light, (2) charge separation and (3) charge collection. The chemical and physical processes behind these basic steps are different in different types of cells and depend on

the materials used. Efficiency of each of these steps affects the efficiency of the solar cell. Efficiency can be maximized by selecting compatible materials for cell design.

1.3.4 Generations of the Solar Cells

Photovoltaic technology has been dominated by high cost-high efficiency, Si based p-n junction solar cells, which are the first generation solar cells. The second generation solar cells consist of Cadmium Telluride solar cells (CdTe), micromorph tandem solar cells, and Copper Indium Gallium Diselenide solar cells (CIS or CIGS) (Aberle, 2009; Jackson et al., 2011; Liu et al., 2017; Xu et al., 2006). Second generation solar cells are considered as low efficiency-low cost solar cells. However in recent times, their efficiency has been enhanced up to 21.3 % (Liu et al., 2017). The drawback of these solar cells is that they contain toxic materials not suitable for the environment. It is highly desirable to produce low cost-high efficiency solar cells. This drive gave birth to emergence of third generation solar cells (Grätzel, 2003). Third generation solar cells consist of Quantum Dot Solar Cells and DSSCs. DSSCs have a record efficiency of 14.1 % and theoretical efficiency of 32 % (Grätzel, 2003). Tandem DSSCs have a tendency to reach efficiency up to 46 % (Grätzel, 2003). DSSC technology is a relatively new technology and long-term performance of these cells have been questioned. However, with further improvements in its stability and efficiency, it can compete with Si based solar cells.

1.3.5 Dye Sensitized Solar Cells

Until 2001, crystalline solar cell technology remained dominant. Crystalline and amorphous solar cells constituted about more than 99 % of the manufactured solar cells. However, work was being done to increase efficiency of the other cells like multi-junction and thin film solar cells for commercialization (Goetzbergeret al., 2003). In 1972, Fujishima, a PhD student, under supervision of Honda, found that exposing TiO_2

electrode to light could split water. This photocatalytic water decomposition was later called as Honda-Fujishima effect (Fujishima, 1972). However, there were some limitations that restricted the conversion efficiency of cells using such electrodes such as the large bandgap of TiO_2 makes it absorb in ultraviolet region of the electromagnetic radiation only. This led researchers to explore alternative metal oxides having appropriate properties. Use of GaAs electrodes gave acceptable efficiencies but problems with photo-corrosion degradation prevailed and by 1980s, the interest in photo-electro-chemical solar cells decreased (Grätzel, 2001).

The research in DSSCs started in the 1960s when Tributch and Gerisher reported an enhancement in the absorption range of wide band gap semiconductor. They observed increased absorption in visible region when the surface of wide bandgap semiconductor like TiO_2 was impregnated with dye molecules (Tributsch & Gerischer, 1969). They used flat electrodes which showed low adsorption of dye and hence low absorption yield. This problem was overcome in 1985 by using rough surfaced semiconductor electrodes which ensured increased adsorption and efficiency of the cells (Desilvestro et al., 1985). In 1991, Brian and Gratzel succeeded to develop DSSC using I^-/I_3^- electrolyte, a mesoporous electrode to increase further dye adsorption, yielding an efficiency of 7 %. DSSCs have reached photo conversion efficiencies for small laboratory cells up to 12 % and for solar modules they have reached to about 9 % (Zalas & Klein, 2012). Few of the main advantages of DSSCs include;

- optimized performance in real world conditions
- low embodied energy and technology
- low manufacturing cost
- variety of substrates
- environment friendly materials

- thin film technology saves resources
- aesthetics
- readily available raw material
- high temperature performance

1.4 Problem Statement

With regards to the DNA/RNA templated formation of conductive and smooth metal wires in sub-micron to nanoscale, a number of issues need to be solved. An improvement in the morphology of the fabricated metal wires and the height of the wires is paramount. The previous studies (explained in detail in Sections 2.1 and 2.2) show irregular, beads on string morphology of the fabricated wires. This nature of wires may cause a decrease in their conductivity and grain boundary electron scattering effect may increase causing high resistance. Therefore, producing smooth and continuous metal wires is an ongoing challenge. Another very important issue that needs to be addressed and has not been resolved before is the easy removal of DNA/RNA scaffold after the formation of the metal structures. After formation of the desired structures, the template scaffold is left on the substrates as residue. Owing to non-ohmic behavior of nucleic acids, the presence of any amount of scaffold residue left on the substrate is detrimental for the conductivity of the wires. Moreover, there is a dire need of economical and controllable writing method to arrange the metal wires onto substrates.

1.5 Aims and Objectives

The general objective of this work is to fabricate the DNA/RNA templated gold/silver (Au/Ag) wires and study their application as modified CEs in DSSCs to enhance the overall performance of the cell. This work has the following specific research objectives;

- optimization and synthesis of Ag/Au wires by DNA/RNA templating method on Si and ITO substrates,
- morphological, structural, electro-catalytic characterization of the fabricated Ag/Au wires,
- study of the potential applications of fabricated Ag/Au wires on substrates as modified CEs in DSSCs and
- fabrication of compatible photoanodes using various deposition techniques, and their performance analysis with the modified CEs.

1.6 Thesis Outline

This thesis is divided into six chapters.

Chapter 1: Introduction. This chapter describes the scope of sub-micron to nanoscale metal wires and the drive to study their application in DSSCs. Scope and objectives of this study has been significantly described.

Chapter 2: Literature Review. This chapter comprises of a detailed study of background of DNA/RNA templated metal wires, the basic structure of these nucleic acids their role in metal wire templating and the previously used techniques of DNA templated metal wire fabrication. The role of CE and photoanode in working of DSSCs and their importance was also discussed. Moreover, the methods to develop semiconductor photoanodes, e.g. AACVD and EPD, have also been briefly discussed. An insight into commonly used characterization techniques and their working principles was also presented.

Chapter 3: Experimental methods. The materials used and the methods adopted in this research were extensively explained in this chapter

Chapter 4: Fabrication of DNA/RNA templated metal wires for CEs. This chapter focuses on the analysis of the results related to the DNA/RNA-metal templating. There are two main highlights of this chapter; the discussion on the structural, morphological and elemental analysis of the fabricated metal wires based on various precursors and process routes and the discussion on the electro-chemical properties of the fabricated wires on various substrates for their application as modified CEs in DSSCs.

Chapter 5: Development of photoanode. Discussion on development of compatible photoanodes along with analysis of their performance with modified CEs have been presented in this chapter.

Chapter 6: Conclusions and future works. A summary of the research findings was presented in this chapter.

CHAPTER 2: LITERATURE REVIEW

2.1 Structure and Properties of DNA and RNA

In order to understand the DNA and RNA templating and scaffolding abilities and their importance, it is essential to have basic knowledge of their structure and properties. The basics of the structure and properties of the nucleic acids have been discussed in this section.

2.1.1 Structure of DNA and RNA

DNA and RNA are essential biological molecules (nucleic acids) which are parts of all living organism and viruses (Sinden, 2012). DNA carries the genetic information while, RNA plays various biological roles like expression of gene, coding-decoding etc. (Watson, 2008). In order to understand DNA/RNA templating and metal-DNA/RNA binding, it is essential to understand their basic structure of the two.

The structure of DNA was first studied by Watson and Crick based on Rosalind Franklin's X-ray diffraction (XRD) results (Watson & Crick, 1993). DNA, as shown in Figure 2.1(a), has a double helix structure formed by the coiling of two biopolymer strands known as polynucleotides (Winnacker, 1978). These strands are composed of nucleotides and each nucleotide is composed of a deoxyribose sugar, a phosphate group and one of the four nitrogen based nucleobases namely Adenine (A), Guanine (G), Cytosine (C) and Thymine (T) as shown in Figure 2.1(b, c) (Varghese et al., 2009). All genes possess almost same 3-D form but differ in number and order of their nucleotide building blocks (Brinton, 1965). The chains of nucleotides are formed by the covalent linkage between deoxyribose sugar of one nucleotide and the phosphate of the next. These chains result in formation of alternating sugar-phosphate backbone of DNA. The nitrogenous bases of two different polynucleotide strands bind together with hydrogen

bonds following the base pairing mechanism (C with G and A with T) and hence the double stranded DNA is formed (Varghese et al., 2009). DNA strands has lengths ranging between nanometers to millimeters, diameter is 2 nm and each base pair has a spacing of 3.5 Å between them.

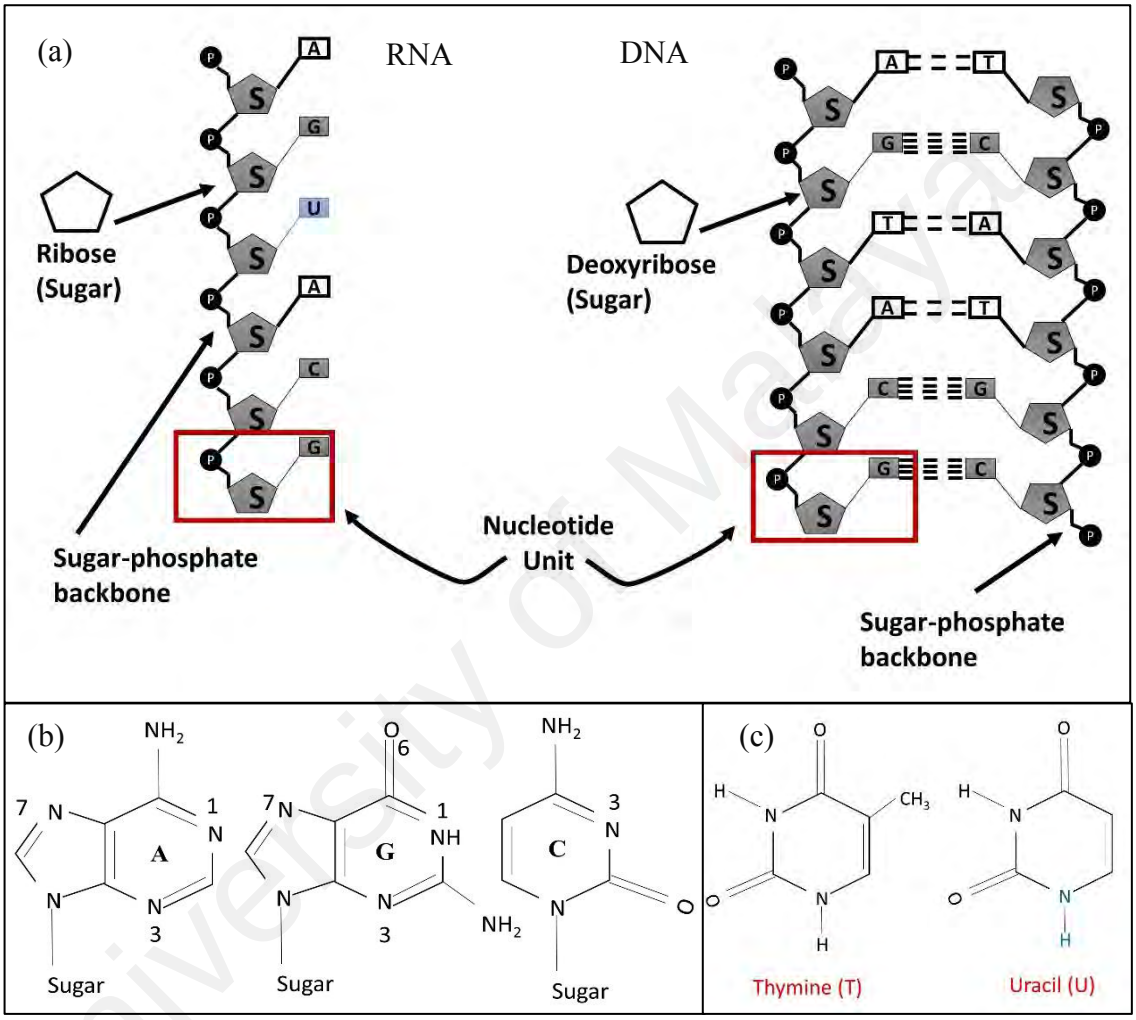

Figure 2.1: Images showing (a) structures of RNA and DNA, (b) nucleotides common in both nucleic acids (c) structures of T in DNA and U in RNA.

RNA also consists of a chain of nucleotides, but differs from DNA in three aspects; the backbone sugar of RNA is ribose instead of deoxyribose in DNA, RNA lacks the nucleobase T and contains Uracil (U) instead. RNA possess a single strand folded to itself i.e. a single polynucleotide chain (Haurwitz et al., 2010; Langridge & Gomatos, 1963). The ribose sugar in RNA has an extra OH group (Watson, 2008). The lengths of the

strands of DNA and RNA are based on the number of base pair and can easily be controlled.

2.1.2 Nucleic Acid-Metal Binding

Interaction of nucleobases, DNA/RNA backbone and the metal nanoparticles (NPs) is an important topic owing to the wide scientific and technological applications. In our study, DNA and RNA are used as scaffold material owing to their natural self-assembly properties and ability to bind metal NPs in order to form metal sub-micron to nanoscale structures. Both these abilities help us to form self-assembled metal wires.

2.1.2.1 DNA-Metal Binding

Studies have shown that DNA molecules allow binding of metal NPs at various sites on its structure. Metal-DNA binding can occur in the following sites; phosphate (DNA backbone)-metal linkage, nucleobases-metal linkage and the combination of phosphate-metal linkage and nucleobase-metal linkage. Backbone of DNA is partially charged negative due to negatively charged phosphate group (Dugui et al., 1993; Scharf & Müller, 2013). Each phosphodiester entity carries one negative charge making DNA polyanionic in nature. Phosphate-metal linkage is based on electrostatic, non-covalent interaction between phosphate groups in the backbone of DNA and the metal NPs. The binding results in the charge compensation and neutralization of the complex (Duguid et al., 1993). Phosphate-metal linkage usually develops between alkali, transition and alkaline earth metals and DNA. For example, Magnesium (Mg) has low affinity for bases and tends to bind to the backbone of DNA (Eichhorn & Shin, 1968; Eisinger et al., 1962). The nucleobases (A, T, G and C) in DNA possess electron donor sites through Nitrogen (N) atoms rings where metal NPs can form coordinate bonds. The most prominent sites for metal binding are G N7 and A N7 such as, the G N7 linkage of Chromium (Cr) (Arakawa et al., 2000). DNA nucleobases can also bind metal NPs through hydrogen bonding

similar to the H-bonding between bases and phosphates. The third form of combination linkage is rare. Such a linkage in which both backbone and nucleobases were involved has been observed for (Palladium) Pd-DNA binding (Al-Hinai et al., 2013).

2.1.2.2 RNA-Metal Binding

The binding of RNA to metal NPs is similar owing to the structural similarity between DNA and RNA. The energetic binding of the isomers follows simple electrostatic rules. At pH 7, the phosphodiester backbone of RNA carries abundant negative charge (Sigel, 2005; Šponer et al., 2005). There are several negative sites in RNA molecule making it polyanionic in nature. The most important metal binding sites in RNA molecules are: purine N7, Uracil O4, Phosphoryl oxygens and G N7. Nevertheless, nucleobases themselves are excellent N and O donor ligands, forming well-defined binding sites primarily for divalent cations (Donghi & Sigel, 2012). Metal NPs can counterbalance the negative charge of the phosphate backbone by diffusely binding to RNA (Freisinger & Sigel, 2007). Theoretically, this diffused metal binding can be explained using non-linear Poisson Boltzmann equation and Hill-type binding formalisms. The non-linear Poisson-Boltzmann equation describes the distribution of charge over dielectric properties of molecule and arbitrary molecular surface on the structure of molecule and the surrounding solvent. Highly negative electrostatic potential regions correlate well with the metal binding sites (Hud, 2009). Therefore, RNA contains an anionic phosphodiester group providing multiple sites for metal NPs to get attached using the principles of electrostatic condensation and charge neutralization.

2.1.3 Self-Assembly of DNA and RNA

Self-assembly of molecules is popularly employed for assembly of well-defined construction of submicron to nano-size structures (Hamley, 2003). Self-assembly is defined as a process in which atoms and molecules act as building blocks to assemble,

arrange and grown into ordered aggregates in a controlled manner. The use of DNA as a building block has been extensively explored (Lin et al., 2006; Nie et al., 2010; Poizot et al., 2000). Figure 2.2(a) shows the synergistic self-assembly of DNA and RNA where the DNA strands guide the RNA strands to self-assemble forming hybrid DNA-RNA branches (Ko et al., 2010). Figure 2.2(b) shows the cleavable RNA strands self-assembled to form RNA sponge (Lee et al., 2012).

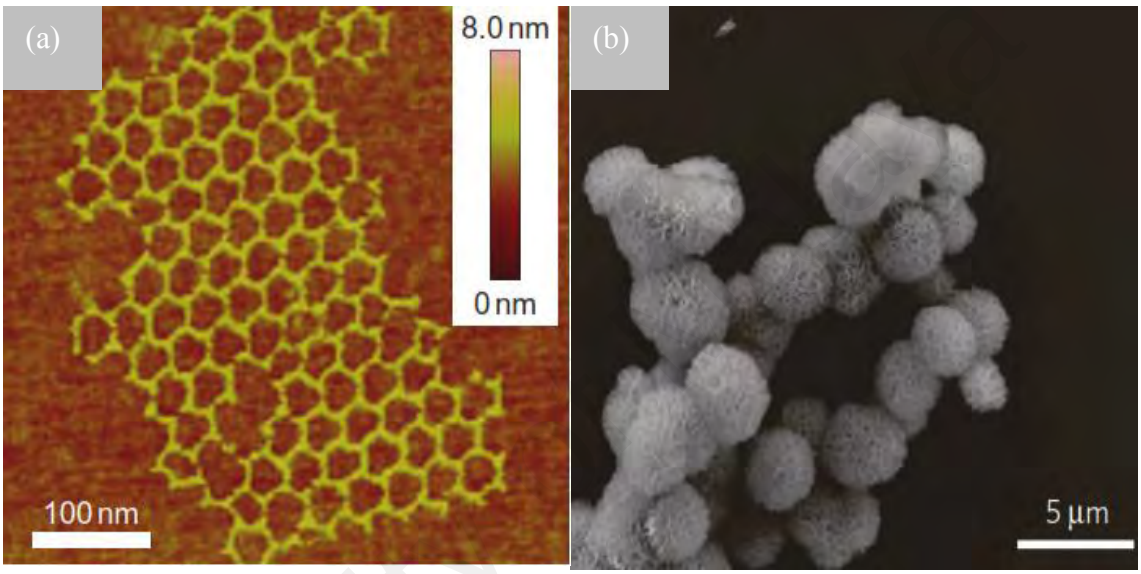

Figure 2.2: (a) AFM image showing synergistic self-assembly of DNA and RNA into DNA-RNA hybrid branches and (b) SEM image of self-assembled RNA sponge (Ko et al., 2010; Lee et al., 2012).

DNA and RNA self-assembly rely upon the self-recognition and base-paired helices. Multiple DNA double helix and RNA single helix strands have the tendency to combine precisely to build programmable sub-assemblies using complementary Watson-Crick base pairing. The arrangement leads to the formation of large number and variety of hierarchical structures and recurrent tertiary architectures of folded RNA/DNA transcripts (Andersen et al., 2009; Becerril et al., 2006; Chworos et al., 2004; Dibrov et al., 2011; Grabow et al., 2011).

A major challenge in this field is how to exploit self-assembly of DNA and RNA to form desired length and shape materials enabling complex structures to be formed entirely by self-assembly. Usually, assembly of nanoscale materials is driven by a thermodynamic force for the compensation of entropy decrease due to formation of ordered systems. Henceforth, submicron to nano-structured material formation requires high control of growth conditions and high precision in assembly of the building blocks. We have employed above mentioned properties of the nucleic acids to assemble DNA-metal and RNA-metal complexes to fabricate connected metal wire structures of desired length. DNA/RNA Templating and Scaffolding. Nucleic acid- metal wire templating is generally a three-step process. The first step is the binding of metal to DNA by incubating DNA with metal NPs called the doping of DNA with metal. The second step is the reduction of the metal on the surface of the template. The final step is the nucleation and growth of metal particles and assembly into metal wires.

2.1.4 Solution and Surface-based Approaches

In solution-based approach, DNA is incubated with metal salts or metal NPs in aqueous solution (Al-Hinai et al., 2013). The films are usually formed on the substrates using drop casting method or spin coating. A major challenge in using this approach is the alignment of wires and templates on the substrates.

Surface-based approach is similar to solution based approach but differ in the method of doping of DNA with metal. In this method, DNA is immobilised on a solid surface before incubating it with metal. DNA template is first formed on the substrate to construct the wire of desired length, and then the doping, nucleation and growth occurs. The alignment of DNA on the surface can also be achieved by molecular combing or electrophoretic stretching (Bensimon et al., 1995; Schurr & Smith, 1990). This method is highly desirable for precise positioning of metal wires for electronic circuits.

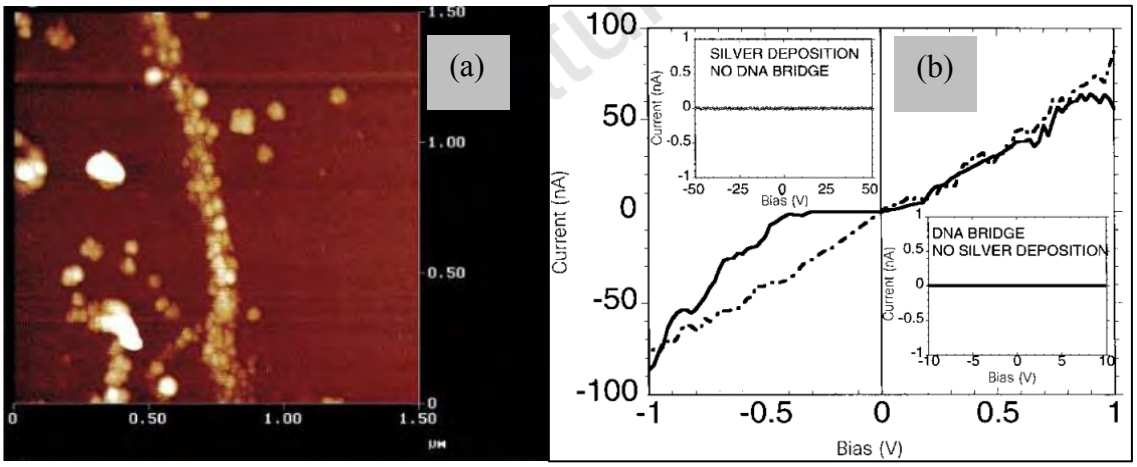

Figure 2.3: *(*a) AFM image of earliest fabricated Ag wires using DNA templating method and (b) the IV profile of the conductive DNA templated Ag wires (Braun et al., 1998).

This research is based on solution-based process. Moreover, the use of coffee-ring effect and scribing method (explained later) allows the fabrication of metal wires of desired length and eliminates the process of DNA immobilisation (attaching DNA to substrates). The importance of DNA as a building block for templating and fabricating various metal structures was realized with the work reported by Braun in 1998 where DNA was used as a template to fabricate conductive silver (Ag) wire (~100 nm diameter) between 2 gold electrodes, 12-16 μm apart as shown in Figure 2.3 (Braun et al., 1998). The λ-DNA was immobilised between two pre-deposited Au electrodes and then treated with silver nitrate ($AgNO_3$) and reduced using hydroquinone solution. Since then, many metals like Ag Pd, Cu etc. have been bound to arrays of DNA or on single DNA molecules to assemble the metals into submicron-structures and nano-structures for their potential applications in nanoelectronics, gas sensing etc. (Al-Hinai et al., 2013; Kudo & Fujihira, 2006; Monson & Woolley, 2003; Park et al., 2006). In 2001, DNA templated conductive Pd nanowires (50 nm diameter) were fabricated by depositing Pd thin film onto single DNA molecules using surface based approach (Richter et al., 2001).

The fabricated Pd nanowires showed ohmic behaviour at room temperature. With the use of molecular combing for stretching of DNA into desired patterns, fabrication of 1-D parallel and 2-D crossed chain Pd arrays were reported (Deng & Mao, 2003). In the subsequent years, Ag nanowires (Al-Said et al., 2009), AuNPs (Sohn et al., 2011), magnetite nanowires (Mohamed et al., 2012), Pd nanowires (Pate et al., 2014), Ag nanoclusters (Léon et al., 2016) and branched Au nanostructures (Song et al., 2016) etc. were successfully fabricated employing surface and solution-based approaches. The morphology of these DNA templated nanowires, NPs and nanoclusters are shown in Figure 2.4.

In the work carried-out by Al-Said (Al-Said et al., 2009) DNA/polymer Ag nanowires were fabricated by aligning DNA using molecular combing to obtain conductive and smooth nanowires (~20 nm thick) (Figure 2.4(a)). To prepare AuNPs using DNA templating in work presented by Sohn et al. (2011), DNA was reacted with chloroauric acid ($HAuCl_4$) to form DNA-Au complex and then reduced (Sohn et al., 2011**)**. The size of AuNPs thus formed were 10 nm with aggregation into formation of clusters of 50 nm (Figure 2.4(b)). The magnetite nanowires (height ~30 nm, Figure 2.4(c)) were synthesized using solution based approach in which an incubated solution of DNA and Fe_2O_4 solution was deposited on substrate using spin coating (Mohamed et al., 2012). Pd nanowires (Figure 2.4(d)) were also fabricated using solution based approach by the electrodeless reduction of Pd (II) on DNA (Al-Hinai et al., 2013**)**. The incubated solution was then drop casted on a substrate and the droplet was dried to obtain nanowires of lengths 5-45 nm at the edge of the dried mass.

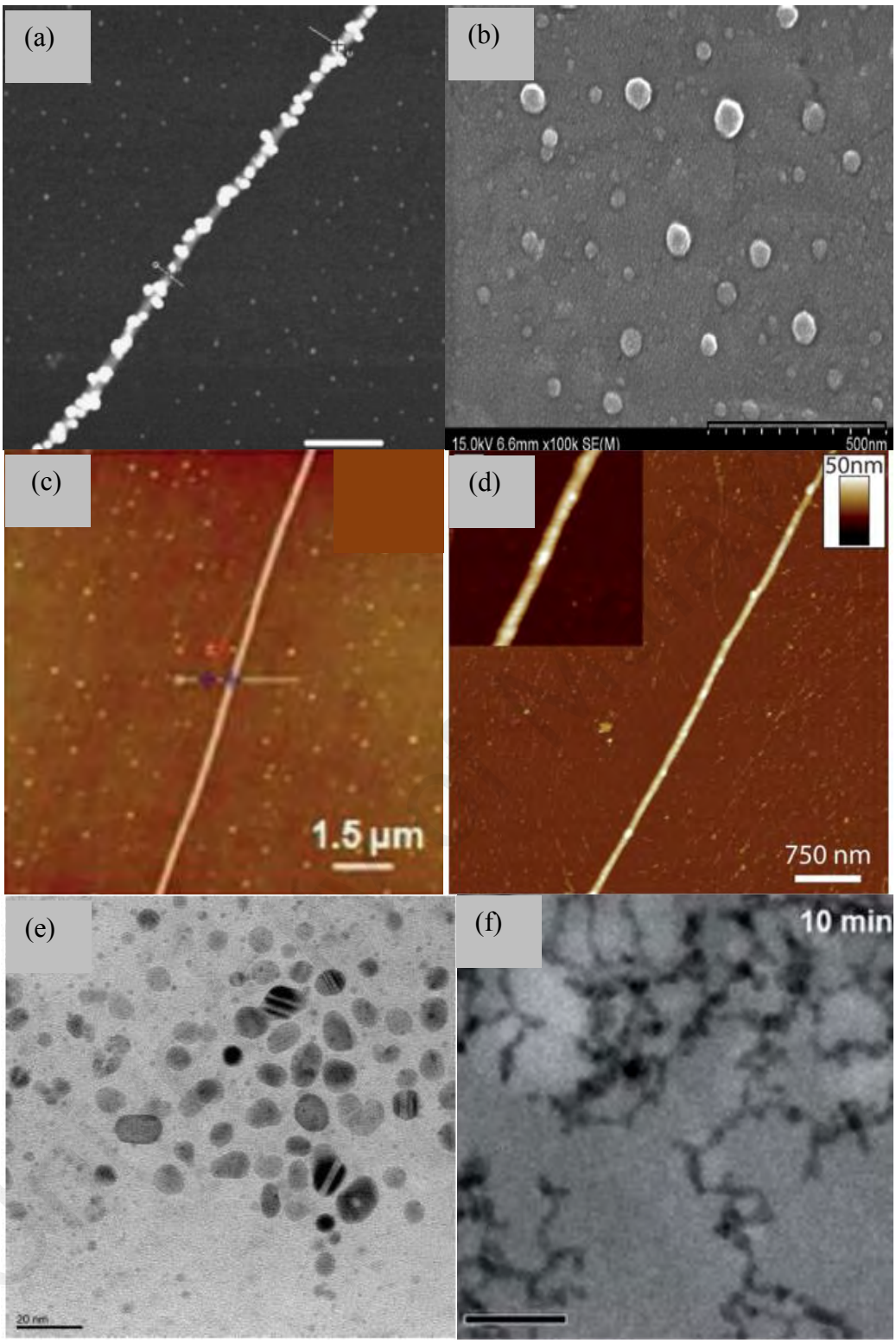

Figure 2.4: (a) AFM image of DNA/polymer templated Ag nanowires, (b) SEM micrograph of DNA templated AuNPs, (c) AFM image of DNA templated magnetite nanowires, (d) AFM image of DNA templated Pd nanowires, (e) TEM image of DNA temlpated Ag nanoclusters and (f) DNA templated branched Au nanostructures (Al-Hinai et al., 2013; Al-Said et al., 2009; Léon et al., 2016; Mohamed et al., 2012; Sohn et al., 2011; Song et al., 2016).

In the work conducted by Léon et al. (2016), Ag nanoclusters were formed by using artificially produced nucleobases to alter the binding sites of the Ag metal cation as shown in Figure 2.4(e)**.** Similarly, in order to fabricate branched Au nanostructures (Song et al., 2016), the branched DNA was first synthesized by annealing 3-4 partially complementary oligonucleotides. Branched DNA was metallized with Au and surface based approach was employed (Figure 2.4(f)). It should be noted that in these studies, the shape and size of DNA templated metal structures highly depend on the method or approach employed.

Recently, capillary force induced fabrication of DNA templated silver wires (average heights 200-400 nm), as shown in Figure 2.5, were reported in which AgNPs were incubated with DNA and solution based approach was used to fabricate the Ag wires (Periasamy et al., 2015; Vengadesh et al., 2015). Capillary force was employed to arrange or stretch the metal wires along a desired length. This method combined the advantages of both, surface and solution-based approaches. For fabrication of solution based-drop casted Pd nanowires (Al-Hinai et al., 2013), the nanowire density was seen along the edge of the dried mass. This was due to the movement of DNA-metal complex towards the edges of the drying film due to differential evaporation rates along the bulk and the edge of the film.

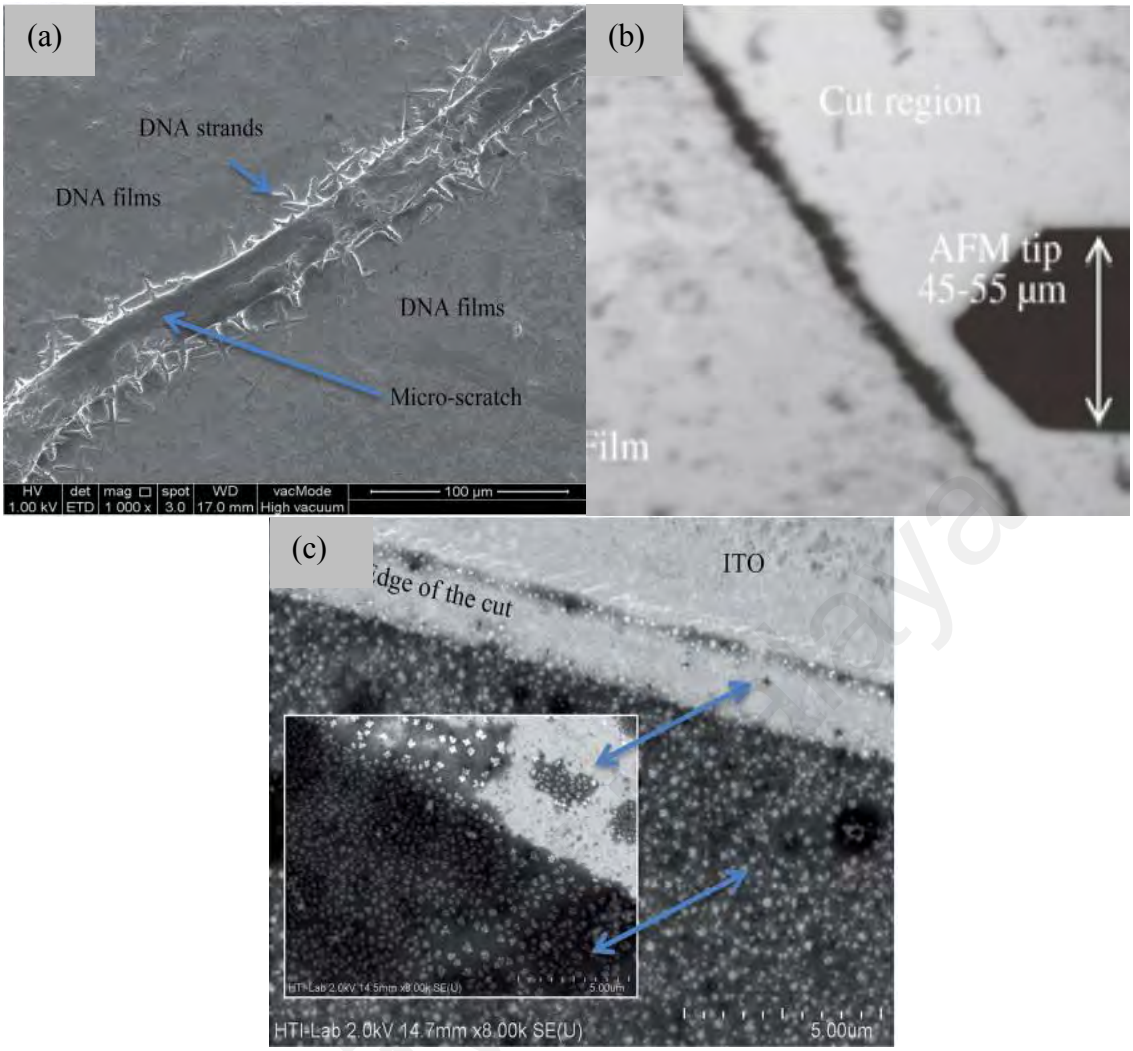

Figure 2.5: (a) FESEM image showing strands of DNA along the scribe and (b, c) AFM image showing deposition of DNA templated Ag wires along the edges of the scribe (Periasamy et al., 2015; Vengadesh et al., 2015).

In the current work to be outlined in this thesis, we introduced a scribe in the middle of a drop casted DNA-metal film to allow the deposition of metal wires along the edges of the cut. The structural resemblance of DNA and RNA allows both the biological molecules to act as a template in fabricating various material structures. However, very few studies have been conducted for use of RNA as a template. RNA has been reported to be used as a template in synthesis of Pd NPs on gold surfaces (Liu et al., 2006) and fabrication of RNA templated CdS nanocrystals (Ma et al., 2006). To the best of our knowledge, none of the studies have been reported for RNA templated metal wire fabrication.

2.2 Metal Wires as Modified CEs in DSSCs

In this section, the working principles of the DSSCs along with their components have been discussed. The role of CE and its influence on performance of DSSCs have also been discussed.

2.2.1 Working Principles of DSSCs

The current generation mechanism of DSSCs is similar to the phenomenon of photosynthesis in plants. Plants convert sunlight into energy using chlorophyll, a green pigment in cells, as light absorbers (sensitizers). In DSSCs function of chlorophyll is performed by an organic dye sensitizer. The water in plants is replaced by electrolyte in DSSCs and function of oxidized di-hydro nicotinamide adenine di nucleotide phosphate (NADPH) is substituted by wide band gap semiconductor (Lagref et al., 2008; Smestad, 1998). In both, photosynthesis and current generation by DSSCs, charge separation occurs by kinetic competition. Whereas, in p-n junction solar cells, charge separation takes place by formation of electric field in the junction (Späth et al., 2003). Photon to energy conversion in DSSCs takes place according to the following steps (Hara & Arakawa 2005; Tennakone et al., 1998; Weerasinghe et al., 2013; William., 2011);

Step 1: Excitation of Dye; Absorption of photons excites the dye molecules from HOMO (highest occupied molecular orbital) to LUMO (lowest unoccupied molecular orbital) states. The excited dye state has a lifetime of nanosecond range.

Step 2: Electron injection into semiconductor; Excited dye molecule injects the electron into CB of the semiconductor and gets oxidized. This occurs in femtosecond timescale range. To ensure efficient electron injection, energy level of semiconductor conduction band must be about 0.2–0.3 V lower than that of dye. The back reaction of

electron from CB to oxidized dye molecule is much slower and lies in microsecond to millisecond range. This difference causes efficient charge separation in the cell.

Step 3: Electricity generation; In the third step, electron diffuses through the photoanode, reaches transparent conducting oxide (TCO) substrate and travels through the outer circuit to generate electric power (flow of electrons). TiO_2 based nano-porous photoanode layer contains anatase TiO_2 NPs. Presence of oxygen vacancies in TiO_2 lattice make it slightly n doped. The plane (101) is thermodynamically stable and is predominant in TiO_2 anatase NPs. One photoanode contains around 10^{16} particles and have 1000 times larger projected area. The electron transport within TiO_2 layer occurs through diffusion since the NPs are very small to form an electric field. The electron transfer can be explained by trapping/de-trapping model. Electron waits in the trap state for time (t) before hopping to next trap site. The trap state waiting time depends on the depth of the trap state. Fick's law of diffusion defines the electron transport according to the following equation;

$$\frac{\delta n}{\delta t \delta A} = -D \frac{\delta c}{\delta x} \tag{2.1}$$

where t is the waiting time, n is the number of electrons, A is the surface area, c is the electron concentration and D is the effective diffusion constant.

Effective diffusion constant depends on the position of quasi Fermi level. Since the transport of electrons takes place by diffusion, diffusion length of electrons must be greater or at least equal to the thickness of photoanode. After the flow of electron through outer circuit, it is collected at the CE.

Step 4: Dye regeneration and electron recapture; Electron after reaching the CE, is transferred to the electrolyte which consists of a redox couple. This electron regenerates the oxidized dye molecule in nanosecond timescale range. A loss of about 600 mV occurs

which is the main reason that limits the open circuit voltage (V_{oc}) of the cell. The loss occurs due to mismatch of energy between redox couple and the dye.

The complete steps of photon to current generation mechanism in DSSCs are shown in Figure 2.6 and represented by the following equations where *D* is dye molecule, D^* excited dye molecule, D^+ oxidized dye molecule and e^- represents electron

$$D + Photon \rightarrow D^*_{LUMO} \text{ (Excitation of dye)} \quad (2.2)$$

$$D^*_{LUMO} + TiO_2 \rightarrow e^-_{CB\ of\ TiO_2} + D^+ \text{ (Injection of } e^-\text{)} \quad (2.3)$$

$$e^-_{CB\ of\ TiO_2} + CE \rightarrow TiO_2 + e^-_{CE} + electricity \text{ (Electricity generation)} \quad (2.4)$$

$$D^+ + \frac{3}{2}I^- \rightarrow D + \frac{1}{2}I_3^- \text{ (Dye regeneration)} \quad (2.5)$$

$$I_3^- + e^-_{CE} \rightarrow CE \text{ (Electron recapture)} \quad (2.6)$$

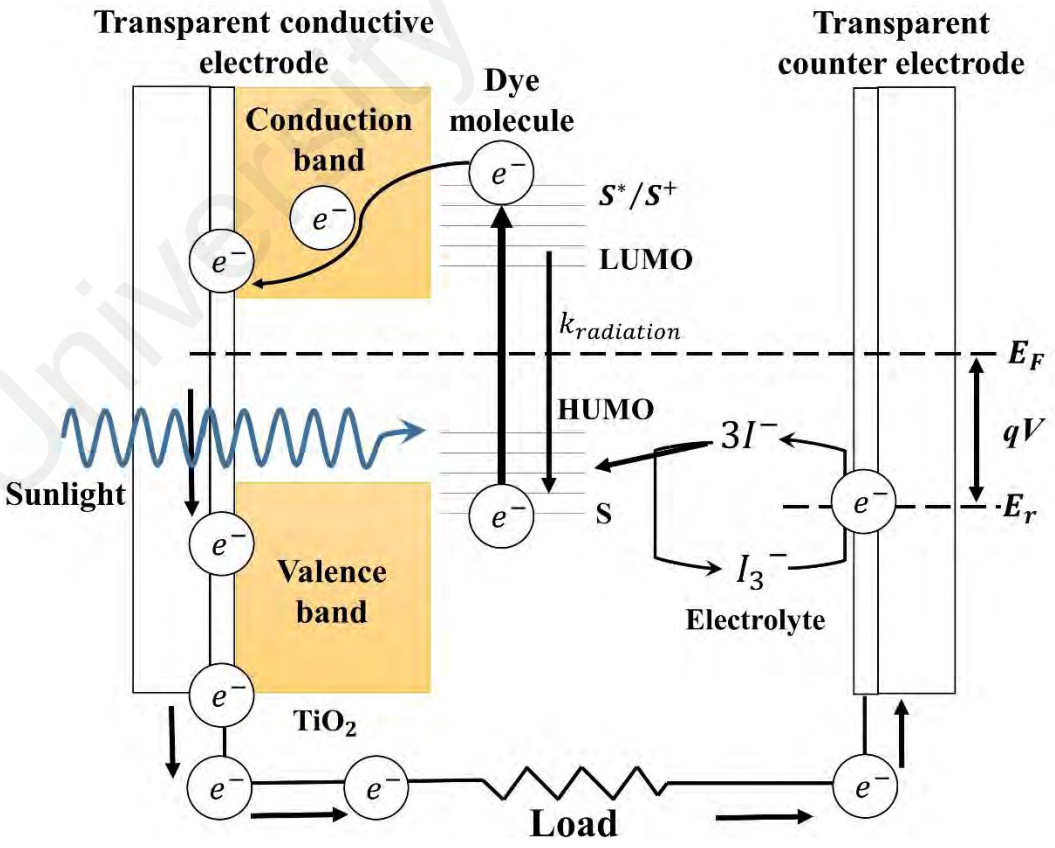

Figure 2.6: Components and working of a DSSCs.

2.2.2 Charge Transfer Kinetics in DSSCs

2.2.2.1 Electron Injection Process

The rate constant for the injection of electron from sensitizer to semiconductor CB is given by the following expression of Fermi's golden rule;

$$c = \frac{4\pi^2}{h} V^2 \rho(E) \tag{2.7}$$

where c is rate constant for electron injection, h is the Planck constant, V is electronic coupling of semiconductor and sensitizer and $\rho(E)$ is density of states of semiconductor CB.

Hence from this expression, the electron injection rate depends on the configuration of dye adsorbed on the wide band gap semiconductor and also on the difference between E_{LUMO} of dye and E_{CB} of semiconductor. The rate constant for electron injection depends on the material of wide gap semiconductor used and on the electronic coupling between dye and semiconductor. Electron is injected from π^* orbital of excited dye molecule to CB of semiconductor. In TiO_2 based DSSCs, valence band consists of occupied 2d orbital of oxygen and CB consists of unoccupied 3d orbital of titanium with large and continuous density of states. N719 dye adsorbs on TiO_2 surface with anchor group (carboxyl group).

2.2.2.2 Recombination and Dark Current

Charge recombination reactions occurring at the interface between semiconductor and dye molecule are very slow as compared to the electron injection. Low recombination leads to high cell performance due to efficient charge transfer. Charge recombination between N719 molecules and TiO_2 semiconductor occurs due to the transfer of electrons from TiO_2 to Ru (III) (back electrons) whereas transfer of electrons from bipyridyl ligands to TiO_2 CB is responsible for electron injection. The transfer from TiO_2 to Ru (III) is a

long-distance process and hence is slower as compared to ultrafast electron injection. This is the reason for least recombination possibility at the dye/semiconductor interface.

Recombination at the semiconductor/electrolyte interface causing dark current is a primary process in DSSCs (Van de Lagemaat et al., 2000). Dark current or reverse bias leakage current is a small electric current flowing through the cell even when the cell is not exposed to irradiation or photons. An increase in dark current decreases V_{oc} of the cell as concluded from general equation of solar cell shown below;

$$V_{oc} = \frac{k_B T}{q} ln\left[\frac{I_{inj}}{I_{dark}} + 1\right] \tag{2.8}$$

where I_{inj} is injection current, I_{dark} is dark current, T is absolute temperature of the cell, q is the magnitude of electron charge and k_B is Boltzmann constant.

This equation relates V_{oc} to dark current and injection current. The main reason for dark current in DSSCs is incomplete adsorption of dye on semiconductor surface. It occurs at points where the electrolyte is in direct contact with semiconductor. The following equation represents the dark current reaction in DSSCs;

$$I_3^- + 2e^-(semiconductor) \rightarrow 3I^- \tag{2.9}$$

2.2.2.3 Electron Transport

Electron transport in semiconductor films is an important process in solar cells (Enache-Pommer et al., 2009). Different mechanisms have been studied and suggested for the conduction of electrons in TiO_2 films like a trapping/de-trapping mechanism, diffusion mechanism and a mechanism that involves insulator metal transition (Cavallo et alo., 2017; Chen et al., 2013; Hsiao et al., 2010). In general, the electrons diffuse by hopping several times between semiconductor particles.

2.2.3 Importance of the CE

One of the most important components of a DSSC is a CE which performs two crucial functions in DSSCs; conduction of electrons from the external circuit and actuate the reduction of the redox couple. One of the two steps of electrochemical process at CE occurs at the electrode-electrolyte interface (redox reactions). Moreover, the mass and charge transfer also occur through the electrode. Reduction of dye ions forms I_3^- ions (tri iodide), which are supposed to be reduced to iodide ions (I^-) at CE. High electro-catalytic activity is a key feature of the CE. Pt-coated TCO substrate are widely employed as CEs in DSSCs (Tang et al., 2013). Recently, carbon nanotubes and graphene have been used as promising alternative materials for CE (Huang et al., 2012; Wang & Hu, 2012). However, the efficiency of these CEs is significantly less than the conventional Pt based CEs. Efficient reduction of I_3^- to I^- is crucial for the high performance of DSSCs. Therefore, a CE material must possess high catalytic activity, good conductivity and high stability (Tachan et al., 2011).

2.3 Characterization Techniques

Characterization techniques are external techniques used in material science to probe into the properties and internal structure of the materials under study. Characterization techniques can be employed for structural, morphological, compositional analysis. Few of the techniques are explained below;

2.3.1 Atomic Force Microscopy

Atomic force microscopy (AFM) is a technique to visualize and measure the surface morphology of a material with high level of accuracy and resolution. It demonstrates the resolution in fractions of a nanometer (Haugstad, 2012). An AFM physically feels the surface of the sample with the help of a sharp probe. By doing this, it builds up the map

of the height of the sample's surface. Surface scanning performed by AFM is done by a cantilever. The cantilever scans the surface of the sample by its probe. Normally, the probe is a sharp tip having a pyramidal shape of 3-6 μm height placed at the end of a cantilever (which can be considered as a spring). The amount of force between the probe and the sample is dependent upon the stiffness of the spring and the cantilever's deflection from the sample's surface (Butt et al., 2005). This force can be described by the Hooke's Law;

$$F = -K.x \tag{2.10}$$

where *F* is the force, *K* is a spring constant (stiffness) and *x* is cantilever deflection (Burnham et al., 2004).

If the spring constant of the cantilever is less than the surface, it results in bending of the cantilever and monitoring of the deflection. The probe of AFM physically feels the sample's surface and builds up the map of the surface's height. To acquire the image's resolution, AFM measures lateral and vertical deflections of the cantilever. When the las

er beam is reflected off the cantilever, it strikes the position-sensitive photo detector, which then indicates the angular deflections of the cantilever. There are three modes of operation of AFM; contact AFM, intermittent contact (tapping mode AFM) and non-contact AFM (Binnig et al., 1986). Contact mode AFM works by the principle of deflection. When the bending of the cantilever occurs due to lesser spring constant from the surface, it is recorded. The force between the sample's surface and the probe is kept constant by maintaining a constant cantilever deflection. The tapping mode or the intermittent mode is similar to the contact mode. However, in this mode the cantilever oscillates at its resonant frequency and the probe lightly taps on the sample's surface. In non-contact mode, the cantilever does not touch the sample's surface (Binnig et al., 1986).

Instead of touching, the cantilever oscillates above the adsorbed fluid layer on the surface during the scanning.

2.3.2 Cyclic Voltammetry

CV is an electrochemical technique which measures the current in an electrochemical cell (Mabbott, 1983). It is useful for obtaining information about complicated electrode reactions. The condition for the measurement of the current is that the voltage exceeds the one which is predicted by the Nernst equation. Nernst equation specifies the relationship between the concentration of two species (labeled O and R) and the potential of an electrode involved in the redox reaction at the electrode. This is expressed as the following equation;

$$E = E^0 - \left(\frac{RT}{nF}\right) \ln\left(\frac{C_o}{C_r}\right) \tag{2.11}$$

where E^0 is the redox potential, C_o is the concentration of the oxidized half of the couple and C_R is the concentration of the reduced half (Marken et al., 2010).

In a CV experiment, the working electrode potential is labeled on the x-axis (linearly) against time. When the set potential is reached in CV experiment, the working electrode potential is ramped in the opposite direction to return to the initial potential. These cycles can be repeated for as many times as required. The cyclic voltammogram trace is obtained when the current at the working electrode is plotted against the applied voltage (i.e. the working electrode's potential).

2.3.3 X-ray Photon Spectroscopy

X-ray Photon Spectroscopy (XPS) is also known as Electron Spectroscopy for Chemical Analysis (ESCA). It is the most widely employed technique for surface characterization because it can be used with an array of different materials (Hercules, 2004). It can also provide valuable quantitative information regarding the chemical state of the surface of the material under study. It reveals which elements are present at the surface.

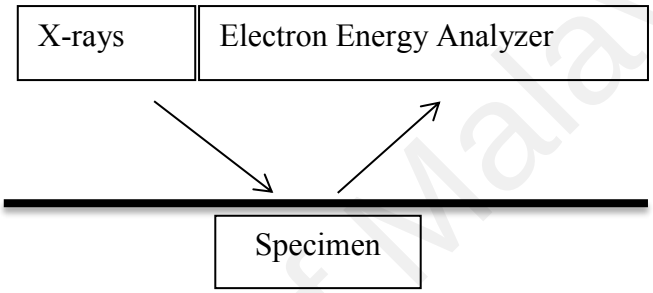

Figure 2.7: Schematic of basic principle of X-ray Photon spectroscopy.

XPS can analyze a sample to a depth of 2 to 5 nm. Initially, the sample is irradiated with X-rays of sufficient energy (Figure 2.7**)**. This irradiation excites the electrons in specific bound states. Typically, in XPS sufficient energy is input to break the photoelectron away from the nuclear attraction force of the element (Engelhard et al., 2017). When the X-rays are bombarded on the sample's surface, some of the photo-ejected electrons scatter in-elastically through the sample on their way to the surface. Once in the vacuum, these are collected by an electron analyzer which measures their kinetic energy. Each energy peak on the spectrum corresponds to a specific element. In addition to this, the intensity of the peak tells how much of an element is present in the material under study. Each peak corresponds to the number of atoms present in each element. XPS is used to analyze materials such as metal alloys, glass, semiconductors,

wood, catalysts, polymers, inorganic compounds, ceramics, bio-materials and many others.

2.3.4 Raman Spectroscopy

Light interacts differently with different materials (Khan et al., 2013). In some materials, light transmits through, while for some materials it reflects or scatters off. This interaction is dominated by the difference in materials and the color (wavelength) of light. Raman spectroscopy consists of one or more single colored light sources as could be achieved using lasers (Bumbrah & Sharma, 2016). The lenses are used to capture the scattered light and to focus the light onto the material sample. A prism is used to split the light into different colors and a light filter is employed to filter out only the Raman light and discard the other reflected and scattered light. Lastly, a very sensitive light detector detects the light and a computer is required to control the whole system and then display the spectrum. Raman spectroscopy is a technique that provides structural fingerprint of a material for the identification of its molecules and their chemical bonds (Mogilevsky et al., 2012). It provides information regarding the molecular vibrations which can be used for sample identification and quantification. It uses a monochromatic light (usually laser) that scatters the photons of a molecule. Majority of the photons scatter within elastic limits, which is of the same frequency as that of the excitation source. This is known as Rayleigh or elastic scattering. However, a small fraction (ca. 10^{-5}% of the incident light intensity) scatters differently. As a result, the impinged laser photons either gain or lose energies. This scattered light forms the Raman spectrum.

2.3.5 X-Ray Diffraction

X-ray diffraction (XRD) is an analytical technique for quantitative determination and identification of phases and orientations in crystalline compounds (Poralan Jr et al., 2015). XRD is a non-destructive and versatile technique that yields crystallographic information of the specimen. About 95 % of solid materials on earth are crystalline like metals, salts, semiconductors, minerals etc (Stanjek & Häusler, 2004). This technique is useful in determining structural properties like grain size, lattice parameters, epitaxy, thermal expansion, type and lengths of chemical bonds in a specimen, etc. When crystalline materials are irradiated by X-rays, they interact with atoms of the material and refract X-rays of characteristic energy as shown in Figure 2.8(a). An individual pattern is generated by each material. In a mixture of materials, each substance gives its own pattern independently. XRD works on the principal of constructive interference of refracted X-rays.

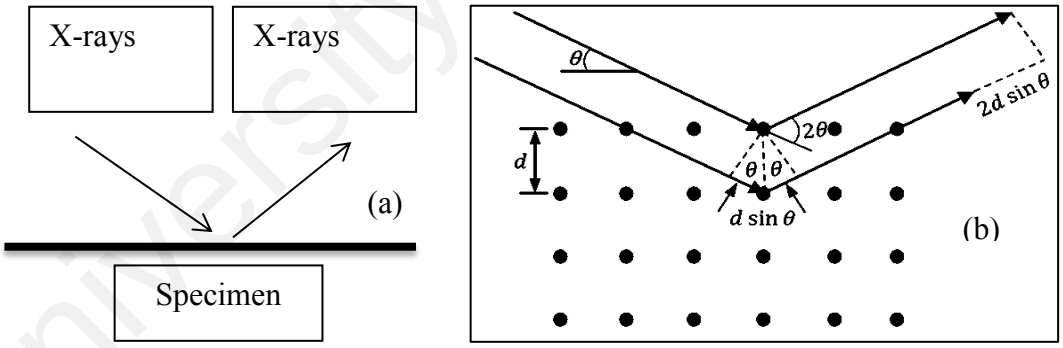

Figure 2.8: (a) Probe beam and measuring particle in XRD and (b) X-ray interaction with atoms according to Bragg's law.

When X-rays interact with matter, 3 phenomena may occur; ionization, fluorescence or diffraction. In XRD, when X-rays hit atoms, the electrons in atom start vibrating with frequency equal to the frequency of the striking X-rays. In most of the directions, destructive interference will occur i.e. both rays will be out of phase and no resultant X-rays will leave the solid sample. In a few directions, constructive interference will occur

i.e. waves will be in phase and well-defined X-ray beams will diffract from the sample as could be determined by Bragg's law (Figure 2.8(b));

$$n\lambda = 2d\sin\theta \tag{2.12}$$

where θ is the angle between incident ray and scattering planes known as incident angle (incident angle is equal to scattering angle), d is the spacing between the planes, λ is wavelength of the X-rays and n is an integer value.

These diffracted X-rays can then be detected by a detector to create a diffractogram. A diffractogram is a graph which is plotted between 2θ on x-axis and intensity on y-axis. This diffractogram is compared with internationally recognized data base (using or without using software). This data base contains reference patterns of almost all crystalline compounds. The detector records intensities of the diffracted beams and angles forming a pattern which is the fingerprint of the material. Miller indices (*h, k, l)* values define the inter-planar spacing and orientation. Number and position of peaks (2θ values) enables determination of the lattice type, cell parameters and crystal class. Intensity of peaks gives information about position and types of atoms in the specimen (Sato et al., 2006).

2.3.6 Scanning Electron Microscopy

SEM is an imaging technique that uses electrons instead of light to study morphology, particle shape and defects of films and powders (Frank et al., 2012). The schematic diagram of a SEM is shown in Figure 2.9. SEM provides magnification up to 300,000X and has an effective probing depth of 10 nm to 1 μm. A focused electron beam interacts with the surface of the sample and secondary electrons and backscattered electrons (BS electrons) are knocked out of the sample creating an electric current which forms the image. Electrons, emitted from a heated filament, are accelerated towards the sample. A

high vacuum is required because gas molecules may cause interference with electron beam and with BS or secondary electrons (Smith & Oatley, 1955). The electrons interact with the atoms of the sample and may produce secondary electrons, characteristic X-rays and BS electrons as shown in Figure 2.10. First electromagnetic lens de-magnifies the primary beam that the second electromagnetic lens focuses. These signals are then detected by a detector. Most SEMs contain secondary electron detectors while only a few may have X-ray or other detectors as well. BS electrons are generated due to elastic scattering. The detector along with cathode ray tube generates the micrograph image (Joy, 2009).

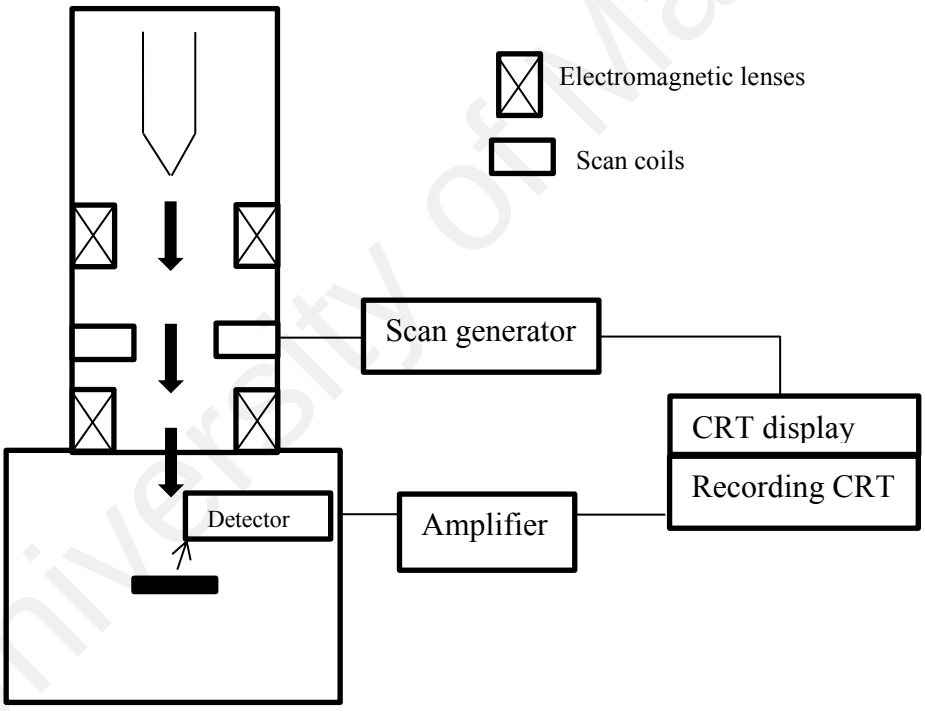

Figure 2.9: Schematic diagram of SEM.

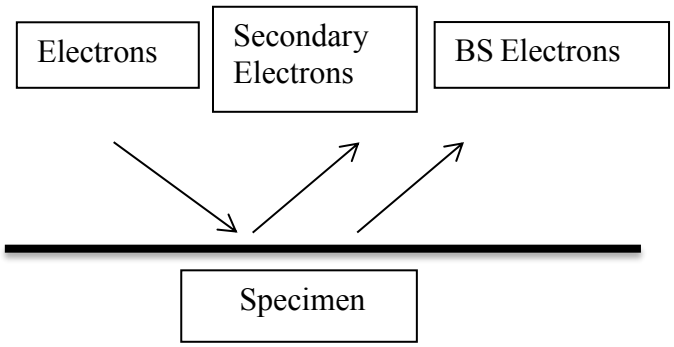

Figure 2.10: Probe beam and measuring particle in SEM.

2.3.7 Energy Dispersive Spectroscopy

Energy dispersive spectroscopy (EDS) is a compositional elemental analysis technique for chemical characterization of the specimen (Frankel & Aitken, 1970). The electrons have an effective probing depth of 1 μm (Rades et al., 2014). EDS is always used in conjunction with transmission electron microscope (TEM), electron probe micro-analyzer (EMPA) or SEM. When focused beam of high energy electrons is bombarded onto a solid sample, X-rays are emitted. The detector makes use of these X-rays to obtain localized chemical analysis (Figure 2.11).

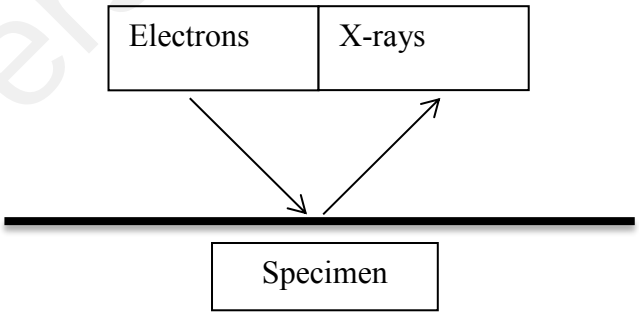

Figure 2.11: Probe beam and measuring particle in EDX.

When electrons strike the specimen, the electrons contained in specimen are excited creating vacant spaces in the atomic shells. Electrons in the higher shells fill these vacancies. The energy released in this process is in the form of X-rays. All elements emit X-rays with characteristic energy values. Each element in periodic table has its specific

energy value which makes elemental analysis through EDS possible. Kα X-rays are emitted when an electron from L shell fills the vacancy in K shell of the atom. Letters K, L and M represent the shell from where electrons are emitted and α, β and γ represent the shells where they are substituted. In principle, all elements in periodic table from beryllium to uranium (atomic number 4 to 92) can be detected by EDS.

2.3.8 Ultraviolet-visible Spectroscopy

Ultraviolet-visible (UV-vis) spectroscopy is an analysis technique which uses visible (400-700 nm) and ultraviolet (190-400 nm) regions of the electromagnetic spectrum to obtain information about organic molecules (Tissue, 2002). It is performed to determine impurities in a sample. Additional peaks other than the specimen substance's peak indicate the presence of impurities. It gives information about structural elucidation of the specimen. Combination and location of peaks helps us to analyze whether saturation, unsaturation and hetero atoms exist in the specimen or not. Quantitative analysis of compounds which absorb UV or visible radiation can be performed using Beer-lambert law (Mäntele & Deniz, 2017). Qualitative analysis can then be performed to determine the type of compounds present in the specimen. The spectrum obtained by UV-vis spectrophotometer is compared to spectra of known compounds. Qualitative analysis of functional groups can also be determined as presence of a band at certain wavelength determines the presence of a particular group. Schematic diagram of a UV-vis spectrophotometer has been shown in Figure 2.12. When the molecules that possess non-bonding or π electrons are irradiated to UV-vis light, the electrons get excited to higher anti-bonding orbitals. Lesser the energy gap between HOMO and LUMO of a material, easier is the excitation of electrons by longer wavelength radiations. When a molecule with energy gap between HOMO-LUMO equal to ΔE is exposed to radiation with wavelength corresponding to ΔE, electron jumps from HOMO to LUMO. This is referred

to as σ - σ* transition. Plot between wavelength on x-axis and absorbance on y-axis is obtained and analyzed (Lott, 1968).

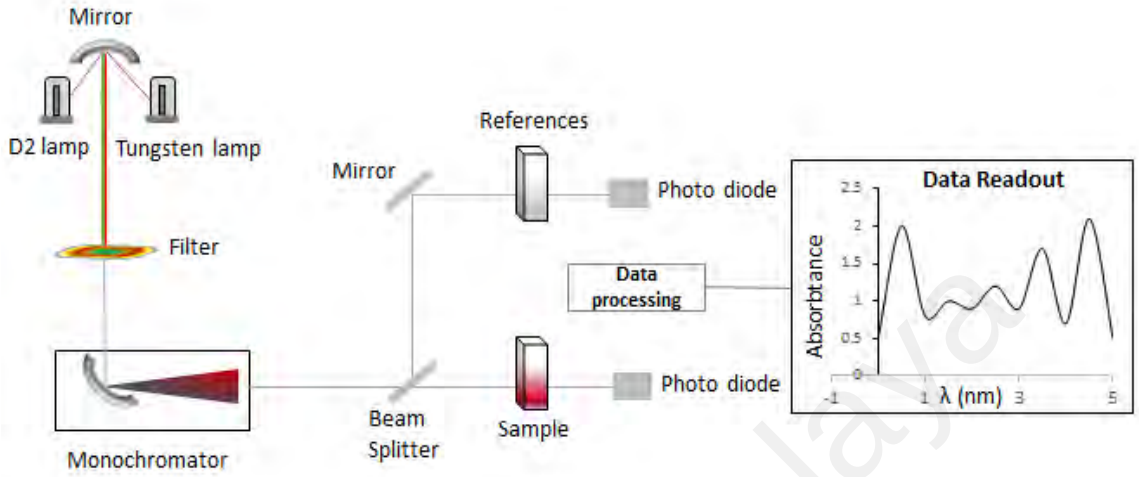

Figure 2.12: Schematic diagram of UV-vis spectrophotometer.

2.3.9 Fourier Transform Infrared Spectroscopy

Fourier transform infrared spectroscopy (FTIR) refers to the type of spectroscopy that works within the distinct region of electromagnetic spectrum known as infrared (IR) region. In this region of electromagnetic spectrum, the light has lower frequency and longer wavelength as compared to visible light. IR spectroscopy mostly includes the techniques based on absorption spectroscopy. This technique is widely used to study and identify chemicals. IR spectrometer is an instrument used in IR spectrometry to produce spectrum of a given liquid, solid, or gaseous sample. This technique is used to identify functional groups and structure elucidation of specimen, identification of substances, detection of impurities, quantitative analysis etc.

If a molecule confronts electromagnetic radiation whose frequency matches to the frequency of any of its vibrational modes, it will absorb energy from radiation and the transition of particle to higher vibrational energy state take place. ΔE (change in energy) between two vibrational states is equivalent to energy associated with absorbed

wavelength (Smith, 2011). Covalent bonds in a flexible, unlike rigid bonds, are flexible and always in a state of a vibration, which could be bending or stretching. The vibrational motion possessed by these molecules is the characteristics of their respective atoms. All organic compounds are capable of absorbing IR, which matches their vibration. The principle of IR spectrometer is similar to the UV-vis spectrometer that allows chemists to obtain absorption spectra that are distinctive reflections of their molecular structure. IR spectrum obtained is a graph between percentage transmittance and wavenumber representing the variation of percentage transmittance with the frequency of the infrared radiation.

CHAPTER 3: EXPERIMENTAL METHODS

Several experiments were performed to achieve the specific objectives mentioned in Chapter 1. Details of the following major experiments are given in this chapter;

- synthesis of AuNPs,
- extraction of DNA and RNA,
- fabrication of RNA templated Ag wires on Si substrate (AgW/Si) as a modified CE in DSSCs,
- fabrication of DNA templated Ag wires on the ITO substrate (AgW/ITO) as a modified CE in DSSCs,
- fabrication of DNA templated Au wires on Pt sputtered ITO substrate (AuW/Pt/ITO) as a modified CE in DSSCs,
- aerosol assisted Chemical Vapor Deposition (AACVD) of TiO_2 and Mg doped TiO_2 on ITO as a modified photoanode DSSCs and
- electrophoretic deposition of TiO_2 and its surface modification on ITO as a modified photoanode in DSSC.

3.1 General Considerations

All the experiments were carried out in a clean room or under an inert atmosphere of dry argon. Most of the chemicals used were purchased from Sigma Aldrich unless mentioned otherwise. ITO substrates (KINTEC, Hong Kong, dimensions 2.5 cm x 2.5 cm, 1.1 mm width, sheet resistance 378 Ω/sq.) were cleaned using acetone, 10% NaOH solution and rinsed in deionized water. All chemicals were used without any further purification. Double distilled water was used to make the solutions unless mentioned otherwise.

The morphology and elemental compositions were studied using FESEM (Quanta FEG 450) at 5 kV, hybrid with INCA Energy 200 (Oxford Inst.), as shown in Figure 3.1(a). SEM images were obtained using HITACHI Tabletop Microscope 3030. AFM images were obtained using Veeco Dimension 3100 (Department of Chemical Engineering and Biotechnology, University of Cambridge). Crystallinity and phase purity studies were conducted using XRD and spectra were recorded and analyzed using PAN analytical X'Pert High score diffractometer at 10 kV voltage, 40 mA current and Cu kα radiation (10-90° Bragg angles, step size, 0.026°).

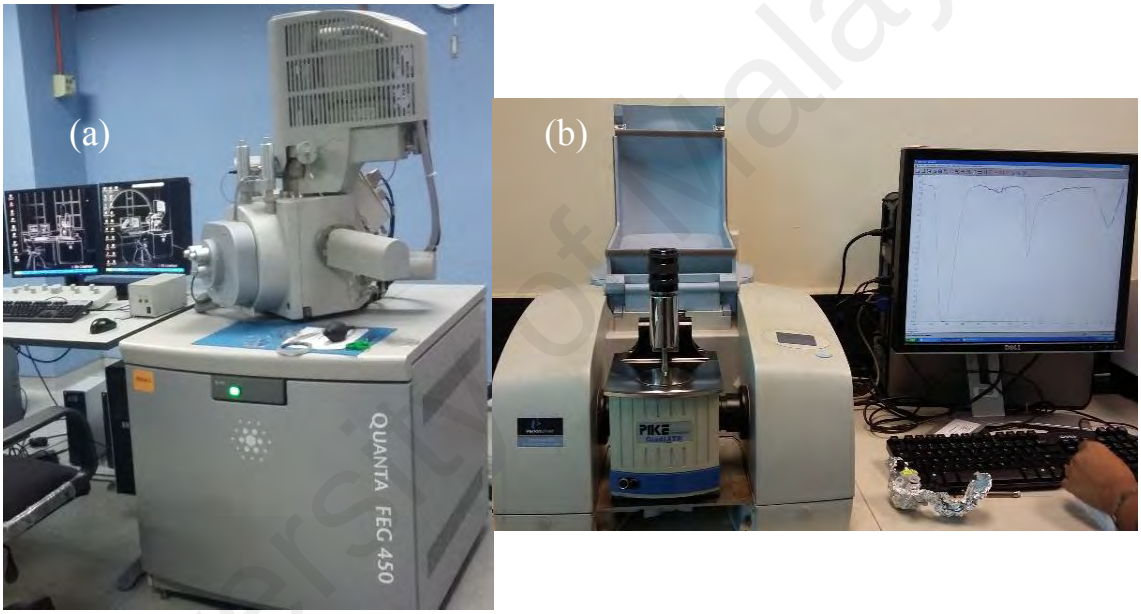

Figure 3.1: (a) Quanta FESEM for morphological studies and (b) Perkin Elmer FTIR equipment for structural characterization.

FTIR spectra were obtained using Perkin Elmer FTIR spectrum 400 **(**Figure 3.1(b**))**, at 4 cm^{-1} resolution. ULVAC-PHI Quantera II with a 32-channel Spherical Capacitor Energy Analyzer was used to carry out XPS measurements under vacuum of 10^{-6} Pa, natural energy width of 680 meV, and monochromatic Al kα radiation. Binding energies were calibrated using carbonaceous C1s line (284.6 eV).

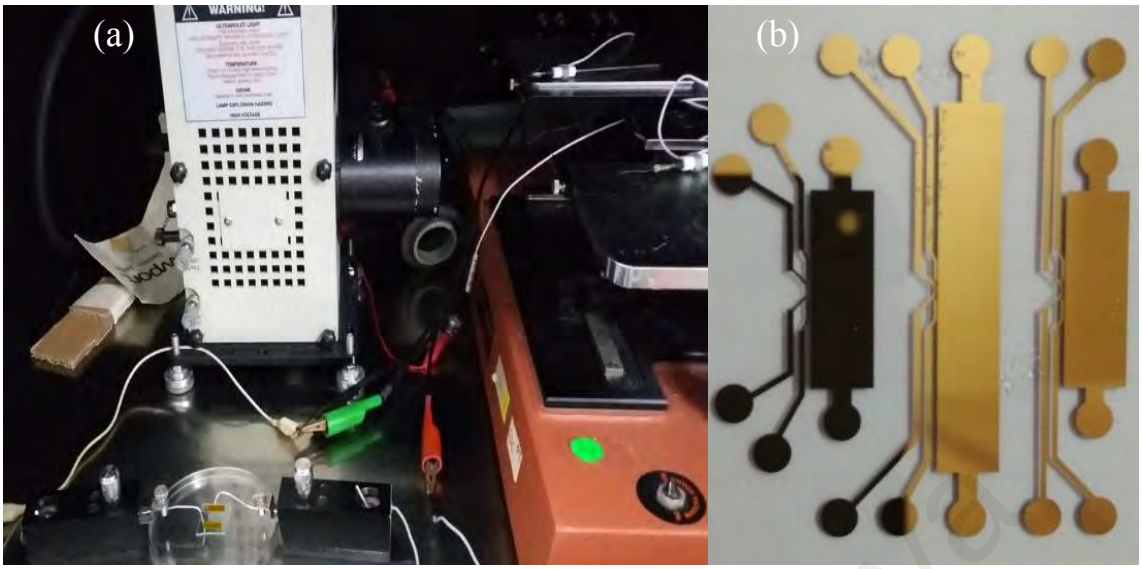

Figure 3.2: (a) Keithley electrometer and (b) a glass substrate with thermally evaporated Au electrodes to study the electrical conductivity of the templated wires.

The electrical properties of the fabricated metal wires along the edges of the scribe were measured using Keithley electrometer Figure 3.2(a) (Source Measurement Unit SMU 236). Samples for I-V characteristics were formed on a conventional glass substrate with two pre-deposited gold electrodes 5 mm apart as shown in Figure 3.2(b). Firstly, a mask was deposited on the surface of the glass substrate. The gold electrodes were then deposited using a thermal evaporator to make a metal contact with the DNA/RNA templated metal wires such that the length of the wires was connected to the gold electrodes. The thickness of the gold layer was ~40 nm.

A three-electrode electrochemical cell system (PAR-VersaSTAT electrochemical work station), as shown in Figure 3.3, was used for CV studies. The working electrode was the as prepared modified CEs, a Pt sheet was used as a CE and Ag/AgCl as a reference electrode. The supporting electrolyte consisted of 500 mM $LiClO_4$, 10 mM I_2 and 50 mM LiI in acetonitrile. Keithley 2400 SMU was used to measure J-V characteristics under 100 $mWcm^{-2}$ illumination using a solar light simulator (Newport 94043A) containing a simulated AM 1.5 filter. J-V test for each DSSC was repeated at least 4 times.

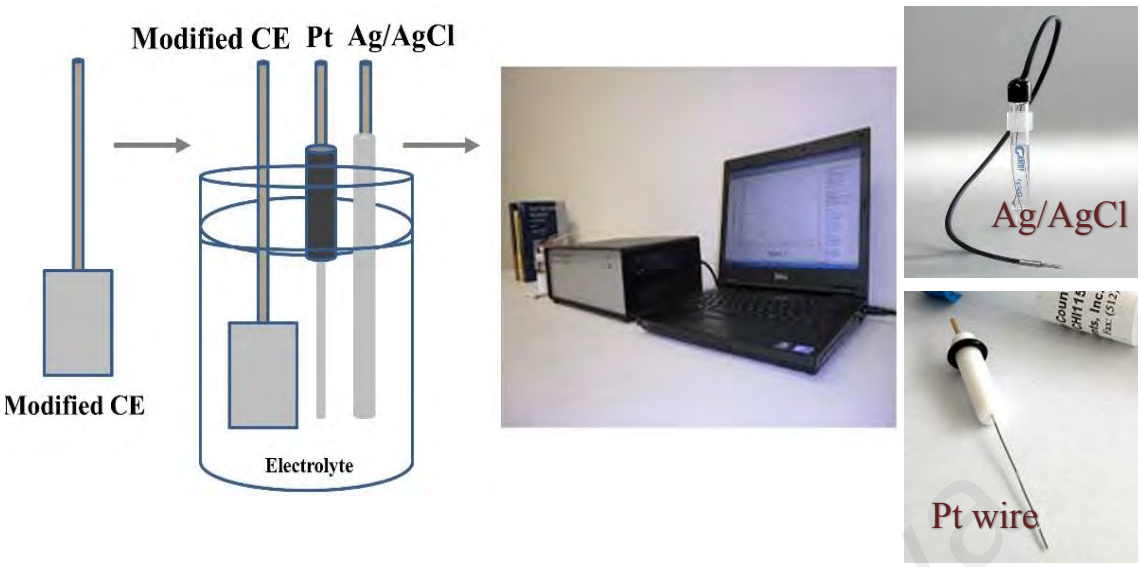

Figure 3.3: Three electrode cell system for study of catalytic properties of CEs.

N_2 adsorption-desorption, Raman and UV-vis spectroscopy were employed for photoanode studies. Phase compositions of the TiO_2 films were confirmed using Raman spectra obtained using RENISHAW Invia 2000 Raman Microscope with an excitation line of the argon laser emitting at 514 nm. Optical properties were studied by UV-vis spectrophotometer (Shimatzu) using $BaSO_4$ as a reference. The Brunauer-Emmett-Teller (BET) surface area of the films were measured using Quantachrome Instruments NOVA4000 and pore size was calculated using Barret-Joyner-Halenda (BJH) method using the desorption curve of nitrogen isotherm.

3.2 Synthesis and Characterization of AuNPs

AuNPs were synthesized in the laboratory via green synthesis and later used as an Au precursor in the fabrication of DNA templated AuW. For the synthesis of AuNPs, 5 ml of 1 mM aqueous solution of Tetrachloroauric (III) acid ($HAuCl_4 \cdot 3H_2O$) was reduced by incubating it with 2 ml of *C. Manga* (CM) extract (10 mg/ml, Yogyakarta, Indonesia) at room temperature for 1 hour. Change in color of the suspension from yellow to red-violet was observed upon the formation of AuNPs (Figure 3.4). Color transition was

apparent within 15 minutes of the reaction. The synthesized AuNPs were then purified by repeated centrifugation at 14,000 rpm for 30 minutes.

Figure 3.4: AuNPs synthesized using green synthesis method showing red-violet color of the synthesized AuNPs.

3.3 Extraction of RNA

Total RNA was extracted from human Wharton's Jelly Mesenchymal Stem Cells primary culture collected at passage 3. Total RNA extraction was carried out using a previously reported method (Kasim et al., 2015). The cell pellets were collected and total RNA was isolated using TRIZOL method (Invitrogen), according to the manufacturer's protocol. The RNA was then quantified using a spectrophotometer (Agilent, NanoDrop, Technologies Inc.) and the purity was assessed by the absorbance value at ratio of 260:280 nm (RNA concentration: 930ng/µl, Ratio of reading of OD260/OD280:2.8).

3.4 Extraction of DNA

Fresh fruiting body of edible mushroom King Oyster: *Pleurotus eryngii* (KLU-M 1380), was dried using a food dehydrator and a small piece of dried tissue was placed in a 2 ml micro centrifuge tube. Total genomic DNA was extracted using Forensic DNA Extraction Kit (Omega Bio-tek) according to the manufacturer's protocol explained elsewhere (Periasamy et al., 2016). DNA purity was assessed by the NanoDrop method using values from absorbance measured at 260 nm and 280 nm. Purified DNA used in

this work showed A260/A280 ratio of 1.98 and A260/A230 ratio of 2.24 with 54.8 ng/µl nucleic acid concentration.

3.5 Fabrication of RNA Templated Ag Wires on Si (AgW/Si) and DSSCs using AgW/Si as Modified CE

3.5.1 Fabrication of RNA Templated AgW/Si

The process of fabrication consists of four major steps; (1) incubation of AgNPs and RNA to form Ag-RNA complexes, (2) drop-casting complexes on the substrate, (3) writing the circuitry (scribing) to promote nucleation and growth of Ag wires, and (4) cleaning the substrates to remove the RNA residue after fabrication of the desired structures **(**Figure 3.5(a**)**).

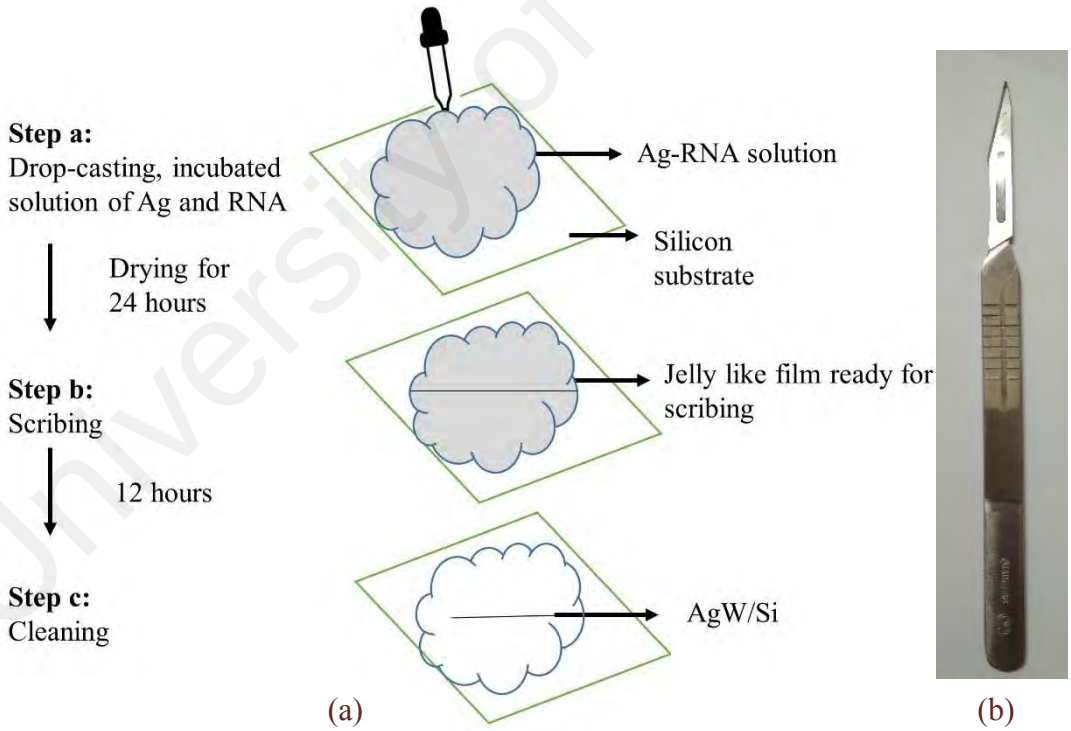

Figure 3.5: (a) Schematic diagram of fabrication of RNA templated AgW/Si and (b) surgical blade for scribing.

P-type silicon (Si) wafers with dimensions of 2.5 cm x 2.5 cm and orientation of (111) were used as the substrates. The Si wafers were washed, cleaned and dried using conventional cleaning procedure. To make Ag loaded RNA solution, 0.2 ml of RNA was mixed with 1 ml deionized water. 0.8 ml of this RNA solution was mixed with 0.8 ml of AgNPs (dispersed in aqueous buffer, 10 nm particle size). The Ag-RNA solution was incubated for 24 hours, allowing AgNPs to bind to the RNA forming Ag-RNA complexes. After which, the Ag-RNA solution was drop-casted onto the Si wafer using a micropipette. 20 minutes later, 0.01 ml of ethanol was applied onto the droplet and left to dry for 12 hours under normal atmospheric conditions. The film was then scribed through its center, using a surgical blade (scalpel handle No. 3, blade No. 11, diameter of blade 39 µm, Figure 3.5(b)) to allow capillary forced diffusion of Ag-RNA complexes towards the edges of the cut leading to the deposition of Ag wires. To ensure complete movement of Ag-RNA complexes from the bulk towards the edges of the scribe, the samples were left in the air for 12 hours. The RNA residue was then removed by washing the samples with bi-distilled water 3 times ensuring complete removal of residue. Autoclaved bi-distilled water was used to prepare the solutions and vessels, pipette, tubes etc. used were RNase free.

3.5.2 Material Characterization

In order to obtain XRD and FTIR signals, the samples were prepared with a thick coating of the films. The fabricated AgW/Si was subjected to XRD, FTIR, FESEM/EDX, and AFM, etc. for their analyses to study the morphology, structure and phase of the fabricated wires. Moreover, electrical and catalytic analyses were also performed to study their performance as a CE in DSSC.

3.5.3 Fabrication of Photoanode

For the comparison of the performance of DSSCs, TiO_2 based photoanodes were developed using the doctor blade coating method. The method employed is same as reported elsewhere (Shakir, Khan, Ali, Akbar, & Musthaq, 2015). A paste of TiO_2 was formed using 2 g TiO_2 powder (Degussa P25), 1 ml ethanol, 1 ml distilled water and a drop of nitric acid. The films were formed on cleaned ITO substrates using the doctor blade. The samples were then dried and annealed at 450 °C. These semiconductor electrodes were immersed into 0.5 mM N-719 (solaronix) dye solution for 24 hours at room temperature. The photoanodes thus formed were washed with water and ethanol.

3.5.4 Fabrication of DSSCs

TiO_2 photoanodes were sandwiched with modified CE (AgW/Si) and were clipped together using clipper pins. The space between the electrodes was filled with electrolyte solution, which was prepared by stirring 500 mM 4-tert-butylpyridine, 100 mM tetramethylammonium iodide, 100 mM tetrabutylammonium iodide, 100 mM LiI, 100 mM KI in 50 mL acetonitrile. Same electrolyte and dye solutions were used in all DSSC devices throughout the studies.

3.6 Fabrication of DNA Templated Ag Wires on ITO (AgW/ITO) and DSSCs using AgW/ITO as Modified CE

3.6.1 Fabrication of AgW/ITO

200 µl of DNA solution was mixed with 200 µl of AgNPs and incubated for 24 hours. Aqueous solution of sodium dodecyl sulfate (SDS) was made with various concentrations (0.2, 0.4 and 0.6 mM) to study the effect of addition of surfactant, and added to the incubated DNA-AgNPs solution. 50 µl of each 0.2 mM SDS Ag-DNA, 0.4 mM SDS Ag-DNA and 0.6 mM SDS Ag-DNA solutions were drop-casted on ITO substrates using a

micropipette and after 20 minutes, a drop of ethanol was added to each sample and left to dry in air (25 °C, clean room environment). After 12 hours, a scribe was made through the center of the films using surgical knife (Figure 3.5(b)). Ethanol dehydrates and concentrates DNA and aids in evaporation. Scribing allowed the movement of Ag-DNA complexes towards the cut. Samples were left for 12 hours to ensure maximum displacement. Enzymatic hydrolysis was then carried out in order to remove the DNA residue by immersing the sample in a solution of appropriate amounts of DNase I (source bovine pancreases), potassium phosphate buffer (pH 7.5) and magnesium chloride. The samples were then washed with water and dried in air. The schematic diagram of the fabrication method is shown in Figure 3.6.

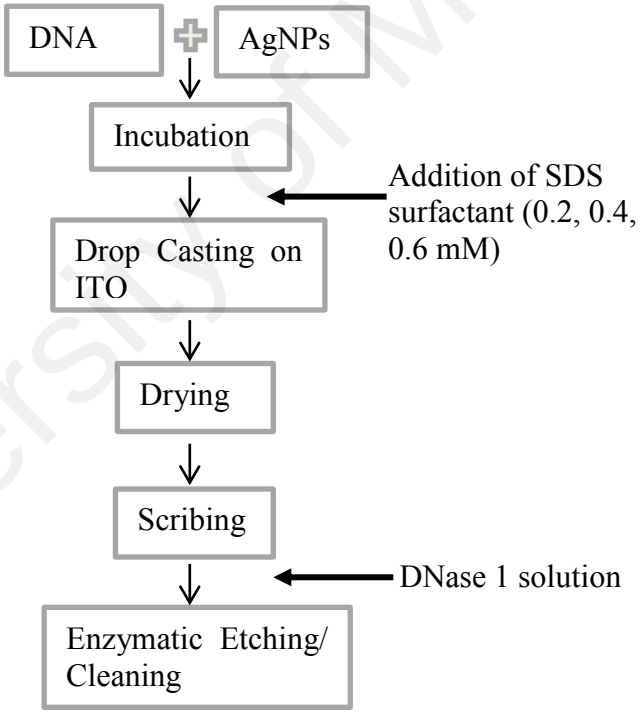

Figure 3.6: Schematic diagram for fabrication of AgW/ITO.

3.6.2 Fabrication of Photoanodes and DSSCs

Photoanodes and DSSCs were fabricated using same method and materials as described in Sections 3.5.2 and 3.5.3. However, AgW/ITO and AgNPs/ITO were used as CEs.

3.7 Fabrication of DNA Templated AuW on Pt sputtered ITO (Au/Pt/ITO)

3.7.1 Fabrication of Pt/ITO

A DC sputtering equipment was used to deposit thin Pt layer on ITO substrates at 35 mA sputtering current and 10^{-2} Torr pressure, forming Pt/ITO layer. Thickness of the Pt films was kept at 50 nm and controlled by carefully monitoring the deposition rate. All the samples were formed using the same deposition rate to standardize the thickness.

3.7.2 Fabrication of AuW/Pt/ITO

Modified CEs were prepared by decorating AuW on Pt/ITO substrates (AuW/Pt/ITO) using DNA templating method. 200 µl of DNA was mixed with 200 µl of AuNPs and incubated for 24 hours to allow binding of AuNPs to DNA. 50 µl of Au-DNA solution was drop-casted on a Pt/ITO substrate using a micropipette and after 20 minutes, a drop of ethanol was added to the droplet and left to dry in air (25 °C, clean room environment). After 12 hours, a scribe was carefully made through the center of the film using surgical knife (scalpel handle No. 3, blade No. 11, diameter 36 µm) without scratching the Pt film. Scribing allowed the movement of Au-DNA complexes towards the edges of the scribe due to the capillary force. The samples were then dried at room temperature for 3 hours, and annealed at 150, 200 and 250 °C in presence of N_2 to avoid any oxidation. DNA residue was then removed using DNase I solution followed by the cleaning of substrate using bi-distilled water and drying in air.

Remaining AuW on the Pt/ITO was then used as the modified CE for DSSCs. For comparison, Pt coated ITO (Pt/ITO) was also used as the standard. The as-prepared AuNPs were drop-casted on Pt/ITO substrate (AuNPs/Pt/ITO) without DNA templating, to study the influence of AuW compared to AuNPs on CE performance.

3.7.3 Fabrication of Photoanodes and DSSCs

Photoanodes and DSSCs were fabricated using the same method and materials as described in Sections 3.5.2 and 3.5.3. However, Pt/ITO AuW/Pt/ITO and AuNPs/Pt/ITO were used as CEs.

3.8 Fabrication of Modified Photoanodes

3.8.1 Deposition of TiO_2 and Mg Doped TiO_2 Films via AACVD

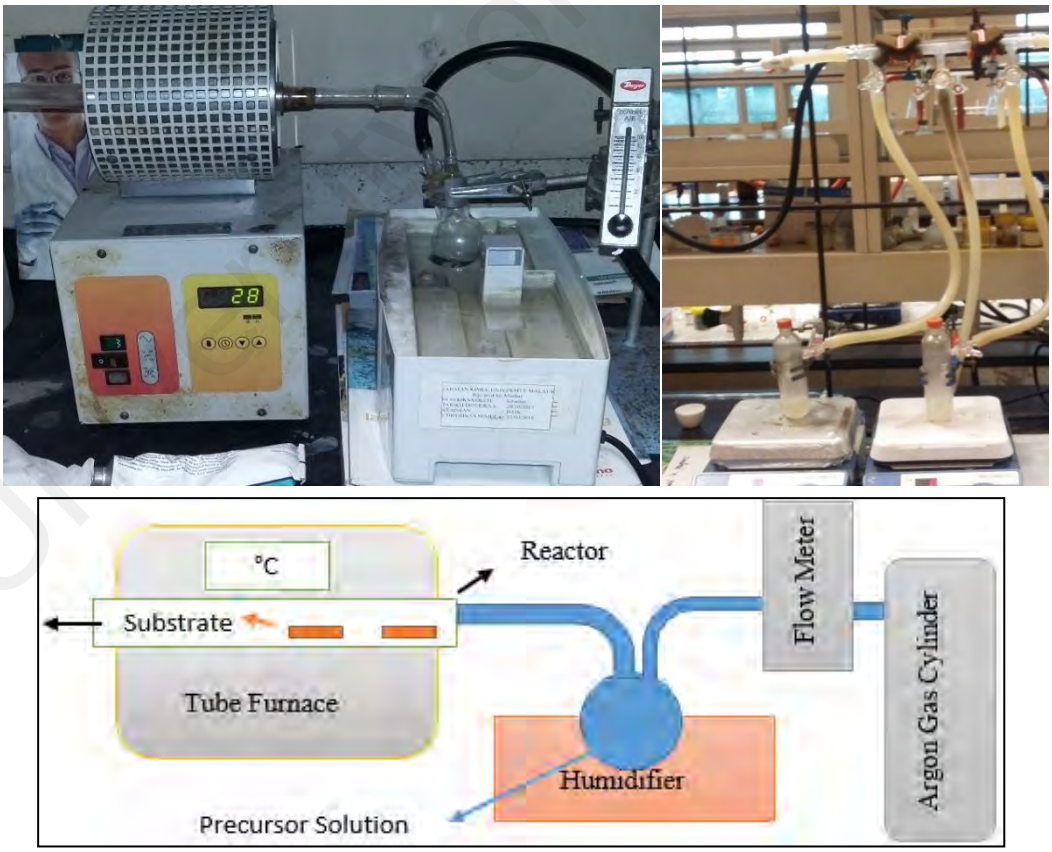

Figure 3.7: AACVD setup for deposition of undoped and doped TiO_2 thin films.

Table 3.1: AACVD conditions for the growth of TiO_2 and Mg doped TiO_2 films.

Annealing Temperature	450 °C
Carrier gas	Argon
Carrier gas flow rate	250 ml/min
Frequency of Humidifier	60 Hz
TiO_2 precursor	TTIP
Solvent	Methanol
Dopant salt	$Mg(NO_3)_2.6H_2O$
Doping Concentrations	0 mol%, 1 mol% and 2 mol%
Time for deposition	120 minutes
Thickness of films	700-800 nm
Substrate	2.5 x 2.5 cm ITO glass

Films were deposited using an in-house AACVD setup. The AACVD assembly is shown in Figure 3.7 and the deposition conditions are summarized in Table 3.1. ITO glass substrates were cleaned by immersing in dilute nitric acid, followed by washing with acetone and distilled water. The substrates were dried in the air and then placed inside the tube furnace chamber 15 minutes before the deposition and the chamber was heated up to the deposition temperature of 450 °C. Titanium (IV) isopropoxide (TTIP) was stirred with methanol to obtain 0.1M solution to prepare undoped films of TiO_2. In order to prepare 1 mol% and 2 mol% Mg doped TiO_2 films, appropriate amounts of $Mg(NO_3)_2.6H_2O$ was first dissolved in methanol (same amount of methanol as for undoped films was used) and then stirred in TTIP until a clear solution was obtained. Aerosols of respective solutions were generated using an ultrasonic air humidifier. The aerosol droplets were carried to the reactor chamber by passing argon gas at a flow rate of 250 ml/min through the aerosol mist. The films were deposited and the samples were annealed at 450 °C simultaneously. After 120 minutes, the humidifier and tube furnace were switched off and argon gas was passed over the substrates until cooled. The films thus obtained were 0 mol%, 1 mol% and 2 mol% Mg doped films.

3.8.1.1 Fabrication of DSSCs

The fabricated films were immersed in 0.5 mM solution of N719 (Solaronix) in ethanol for 24 hours for sensitization. The films were then washed with ethanol and dried at room temperature. These dye-adsorbed electrodes (photoanodes) were clamped with conventional CEs (platinum sputtered on ITO) to make sandwich type cells and the space between the photoanode and CE were filled with I^-/I_3^- redox electrolyte. The photoanode exhibiting the best J-V characteristics was then clamped with AuW/Pt/ITO CE and the performance of thus formed DSSC was analyzed.

3.8.2 Surface Modified TiO_2 Films Fabricated using EPD

3.8.2.1 Fabrication of Multistep EPD TiO_2 films

ITO glass with an active area of 0.4 cm^2 were used as substrates to fabricate TiO_2 photoanode films via EPD. The precursor solution for EPD was made by stirring together TiO_2 NPs (20 nm, P25, Degussa) with concentration of 5 g/l with isopropyl alcohol, acetone and DI water. To make the electrolyte for EPD process, 0.05 mM aqueous solution of magnesium nitrate hexahydrate was prepared. A standard spacing of 2.5 cm was used between the anode and ITO cathode. The EPD process was carried out at various electric fields (10, 15 and 20 V) to determine the optimum conditions. Multiple step EPD was performed at each electric field for 20 seconds using the method reported earlier (Hamadanian et al., 2012). Each EPD was carried out for 5 seconds, the photoanode was removed and the deposited layer was annealed at 150 °C for 10 minutes. Another layer was then deposited and the process was repeated 2 more times until 20 seconds deposition time was achieved for each film. The deposited layers were then soaked in a solution of 0.2 N H_2SO_4 in DI water in order to remove the Mg electrolyte. The films were rinsed using DI water and annealed at 450 °C for 1 hour. Experimental setup employed for EPD

method is shown is Figure. 3.8. To compare, films were also fabricated using single step EPD at 20 V while the rest of parameters were the same as for the multistep EPD process.

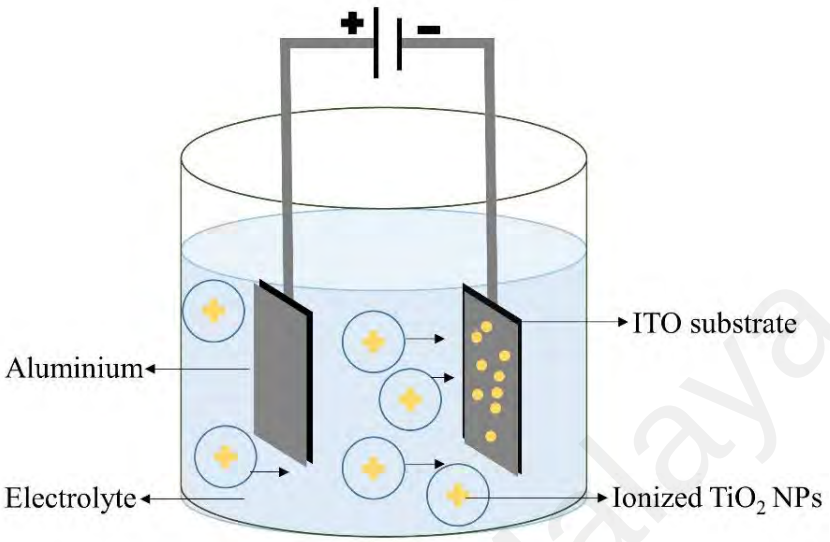

Figure 3.8: Schematic diagram of EPD assembly.

3.8.2.2 Surface Modification and Fabrication of Solar Cells

After optimizing the EPD deposition electric field, the best film was modified by loading it with Sn. The photoanode was immersed in 0.01 M aqueous solution of tin chloride and simulated using an ultrasonic generator at a frequency of 50 kHz for 30 minutes. The film was then washed with DI water, and dried at 100 °C in a vacuum oven. The solar cells were fabricated using EPD based photoanodes. The rest of the assembly of DSSC is same as described in Section 3.8.1.1.

CHAPTER 4: RESULTS AND DISCUSSION I: DNA/RNA TEMPLATED METAL WIRES

In this chapter, the characterization of DNA and RNA templated Ag and Au wires are discussed. The structural, morphological, electrical and catalytic properties of the fabricated metal wires are probed. Various process routes like the effect of addition of surfactant, effect of annealing temperature, etc. have been discussed along with the nucleation and growth mechanism. Moreover, the comparison of using RNA and DNA as scaffolding material has also been discussed in this chapter. The fabrication of metal wires onto different substrates like Si wafer, ITO and Pt sputtered ITO, and their application as a modified CE in DSSCs are studied in detail. The comparisons of CEs have also been elaborated based on their catalytic properties and the J-V characteristics of the DSSCs fabricated using different modified CEs and identical photoanodes (doctor blade coated TiO_2, N719 dye and I^-/I_3^- redox electrolyte).

4.1 Development of DNA/RNA Templated Metal Wires on Various Substrates as Modified CEs

4.1.1 Studies on AgNPs

In this section, studies have been conducted on the structure, crystal phase, morphology and elemental analysis of the AgNPs. It is important to know the morphology, phase and crystal structure characteristics of the AgNPs in order to understand their templating into conductive wires using RNA and DNA as a scaffold.

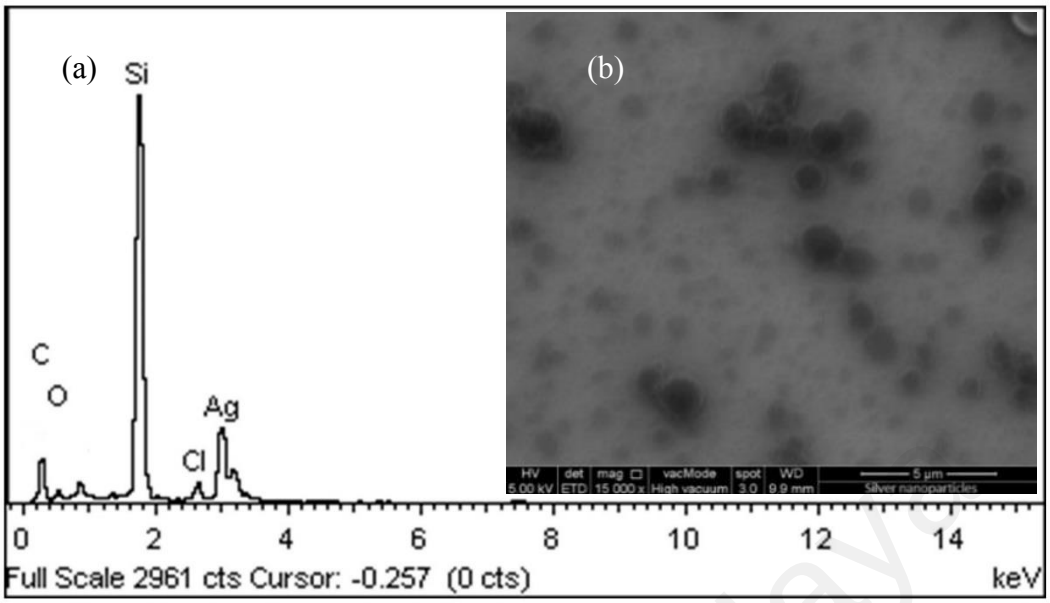

Figure 4.1: (a) EDX spectra and (b) FESEM images of AgNPs on Si substrate.

Figure 4.1(a) shows the EDX spectra of the AgNPs. EDX signals are recorded when the specimen under study emits X-rays when subjected to a focused electron beam. An inner shell of electrons may be excited by the electron beam, causing the ejection of the electron from the shell. This creates an electron deficiency of a hole which is filled by an electron from the outer shell. This causes an energy drop, which is compensated by the X-ray emission. Difference between the energies of the inner and outer shell determines the energy of the emitted X-ray. This difference in energy between the shells the is characteristic of one element, thereby, identifying the element as characteristic signals. The EDX spectra shows the presence of Ag along with trace amounts of C, O and Cl due to capping agents. The FESEM image of drop-casted AgNPs on Si substrate, as shown in Figure 4.1(b), depicted AgNPs of spherical shape with some agglomerations. The average particle size of the AgNPs is 10 nm.

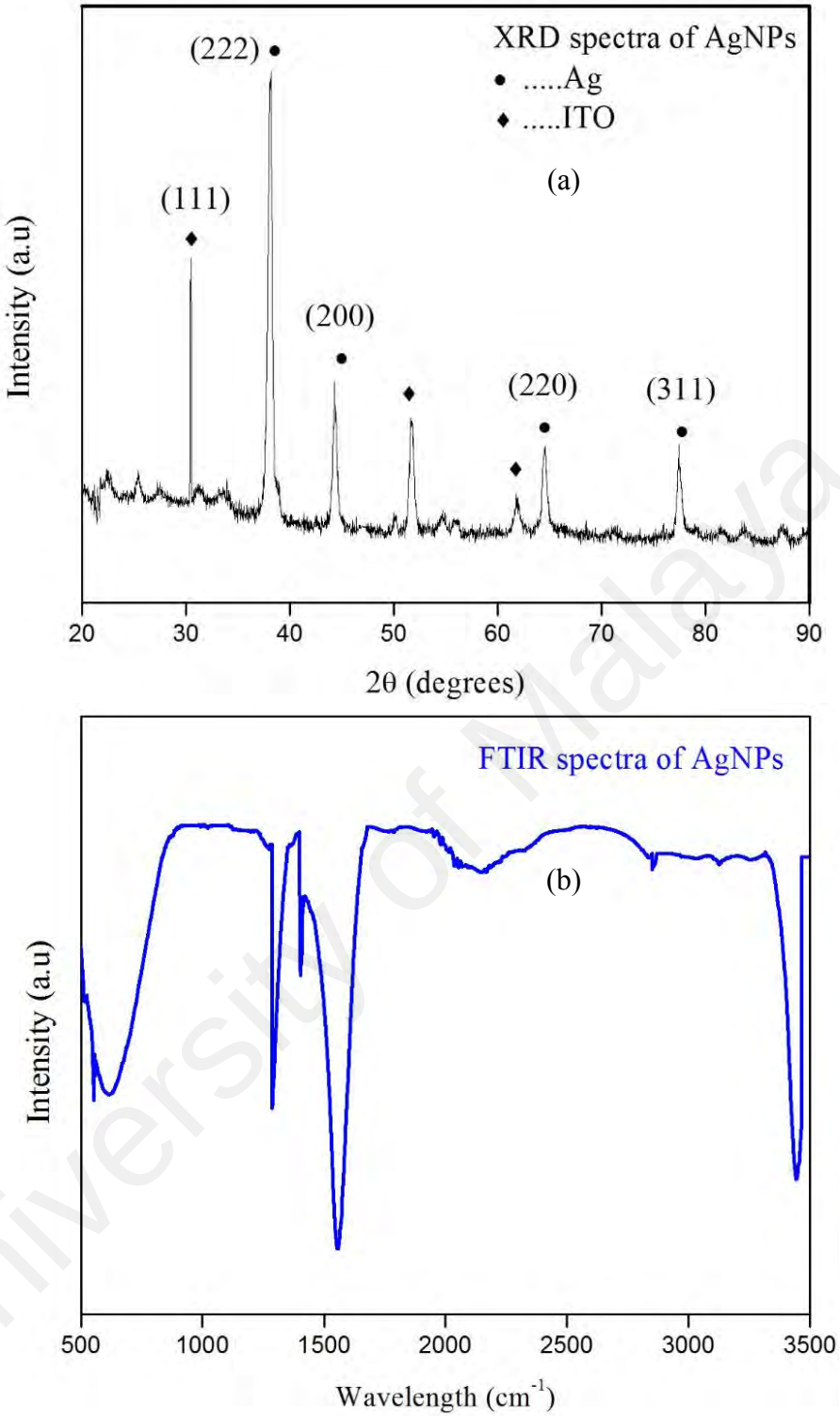

Figure 4.2: Images showing (a) XRD spectra and (b) FTIR spectra of AgNPs.

The crystalline phases and chemical identity of the AgNPs were determined using XRD and the spectrum is shown in Figure 4.2(a). Characteristic diffraction peaks can be observed at 38.2, 44.5, 64.5, 77.6 and 81.5° representing the (111), (200), (220), (311) and (222) reflection planes, respectively, of the face centered cubic (fcc) single crystalline

structure of Ag (JCPDS No. 4-0783) (Sathishkumar et al., 2009; Veith et al., 2011). The data from most intense diffraction peak at 38.2° was used to calculate the crystallite size of the NPs using Scherer equation;

$$\tau = \frac{K.\lambda}{\beta cos\theta} \tag{4.1}$$

where, τ is the crystallite size, K is a constant (shape factor), λ is the wavelength of the X-ray, β is line broadening at FWHM (full width half maximum) and θ is the Braggs angle. The crystallite size (mean diameter) of the Ag metal phase was calculated to be 40 nm.

FTIR spectra of AgNPs (Figure 4.2(b)), reveals significant peaks at 1051 cm^{-1} attributed to carbonyl group (–C=O), 1352 cm^{-1} for C-C stretching, 2954 cm^{-1} attributed to the C-H stretching vibrations (D. Kumar et al., 2015) and 3438 cm^{-1} is due to the presence of hydroxyl group O-H stretching vibration (Lin et al., 2010). These peaks are mainly due to bonds present in the capping agent and water molecules.

4.1.2 RNA Templated Ag Wires on Si Wafer

In the previous section, basic characteristics of AgNPs were studied as AgNPs solution is the metal precursor for DNA/RNA templated Ag wires. In the following section, fabrication of RNA templated Ag wires on Si wafer (AgW/Si) were discussed. The mechanism of fabrication of RNA templated Ag wires involves a three-step process; (1) the binding of AgNPs to RNA molecule due to electrostatic interactions forming Ag-RNA complexes, (2) the reduction of the AgNPs on the surface of RNA and (3) their rearrangement, nucleation and growth into well-connected-conductive AgW. A novel idea proposed in this study is the utilization of capillary force action to arrange the fabricated AgW along the edges of a scribe. The Ag-RNA film on the substrate was scribed using a surgical blade which, allows the evaporation of water from the edges of

the scribe. The diffusion of water molecules and Ag-RNA complexes towards the edges of the scribe occurs due to differential evaporation rates along the film leading to the effective deposition of AgW. Meanwhile, the reduction of AgNPs on RNA forms the seed for nucleation and growth. The fabricated AgW/Si was morphologically and structurally characterized for its potential application as a modified CE in DSSCs. Moreover, the binding of AgNPs with RNA was also studied using FTIR spectroscopy. The electro-catalytic activity and conductivity of the fabricated AgW on Si substrate were analyzed for the use of AgW/Si as a CE in DSSCs.

4.1.2.1 Morphological and Elemental Analysis of the Fabricated Wires

Figure 4.3(a) shows the negative control for RNA templated AgW, in which AgNPs solution was drop-casted and scribed on Si substrate without binding with scaffold i.e. in absence of RNA. Scattered networks of AgNPs can be observed and only a small amount of material density can be seen at the edges of the scribe due to capillary forced diffusion. This emphasizes on the importance of RNA scaffolding and its self-assembly in arranging the AgNPs as AgW. Figure 4.3(b) shows the structure of RNA drop-casted on Si wafer (without AgNPs). In our study, RNA is used as a scaffold owing to the self-assembly and ability to bind AgNPs. RNA also serves as a template for AgNPs to form nucleation sites for the growth of wires. Higher material density can be seen in Figure 4.3(c) along the edges of the cut. Removal of RNA scaffold leaves behind clean AgW/Si as can be seen in Figure 4.3(d). The backbone of RNA consists of phosphate molecules and ribose (sugar) in alternative manner. The ribose (sugar) consists of multiple hydroxyl groups that allow the formation of hydrogen bonds with water.

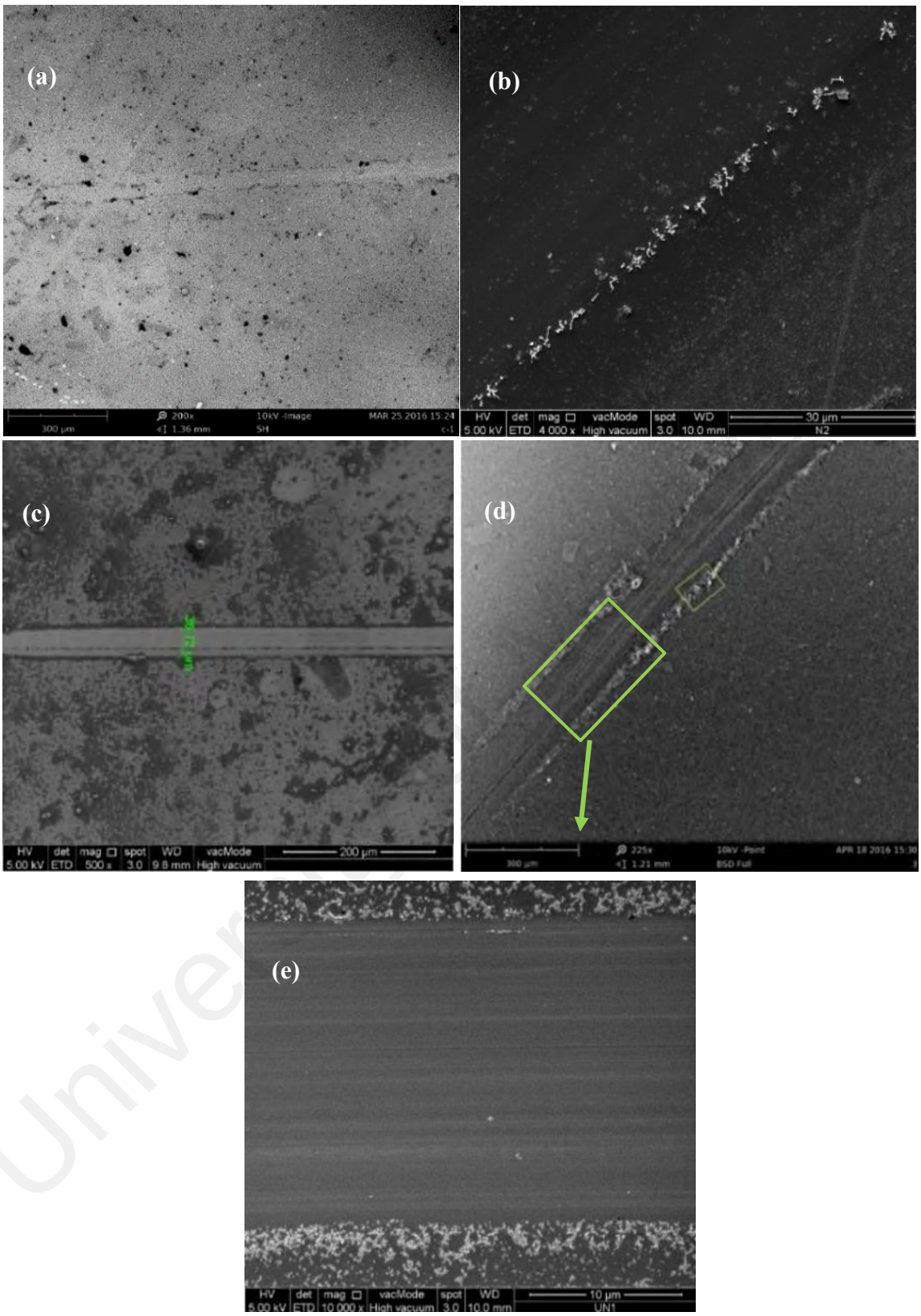

Figure 4.3: Images showing morphology of (a) AgNPs scribed without RNA, (b) RNA, (c) Ag-RNA scribed before cleaning, (d) AgW after cleaning and (e) magnified view of AgW.

Unlike DNA, the ribose sugar in RNA has an extra -OH group making it more soluble in water (Bolton & Kearns, 1978; Cate et al., 1996). Also, exposed bases are present in RNA that contain polar bonds. More the polar bonds, more is its solubility in water. Figure 4.3(e) shows the magnified image of the fabricated AgW/Si. Formation of Ag wires around the edges of the scribe can be explained by the capillary force action due to drying drops of solution or the coffee-ring effect (Deegan et al., 2000) as illustrated in Figure 4.4.

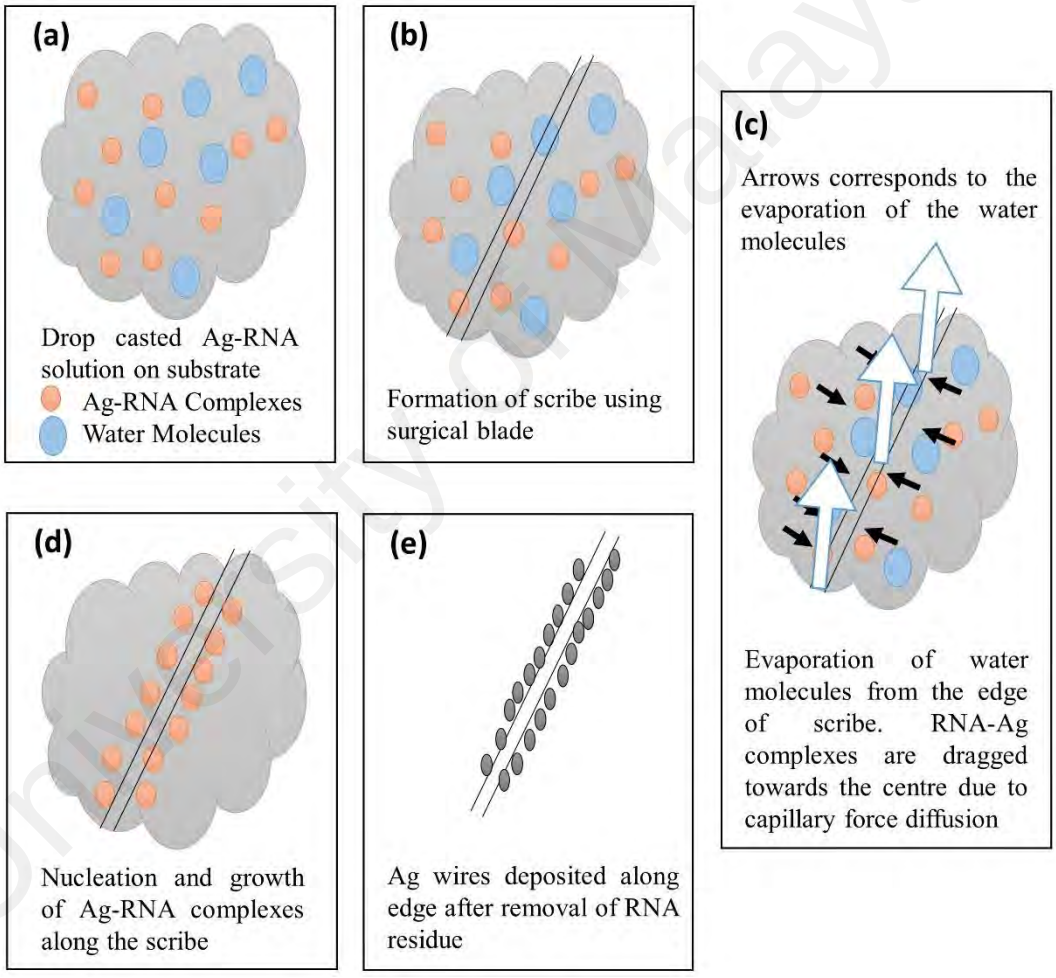

Figure 4.4: Schematic illustration of the aligning of RNA templated AgW along the edges of the scribe.

When AgNPs are incubated with RNA, they bind themselves to the RNA molecules. The energetic binding of the isomers follow simple electrostatic rules (Doria et al., 2012). At pH 7, the phosphodiester backbone of RNA carries an abundant negative charge. AgNPs can counterbalance the negative charge of the phosphate backbone by diffusely binding to RNA (Donghi & Sigel, 2012). Moreover, there are several negative sites in a RNA molecule making it polyanionic in nature (Freisinger & Sigel, 2007). The most well-defined metal binding sites in RNA molecules are purine N7, uracil O4, phosphoryl oxygens and guanosine (Donghi & Sigel, 2012). The nucleobases are excellent O and N donor ligands and forms good sites for metal NPs binding (Lipfert et al., 2014; Šponer et al., 2006). Therefore, AgNPs can bind to RNA either with the backbone of RNA or the binding sites with the nucleobases. This binding is termed as RNA doping and complexes thus formed are Ag-RNA complexes.

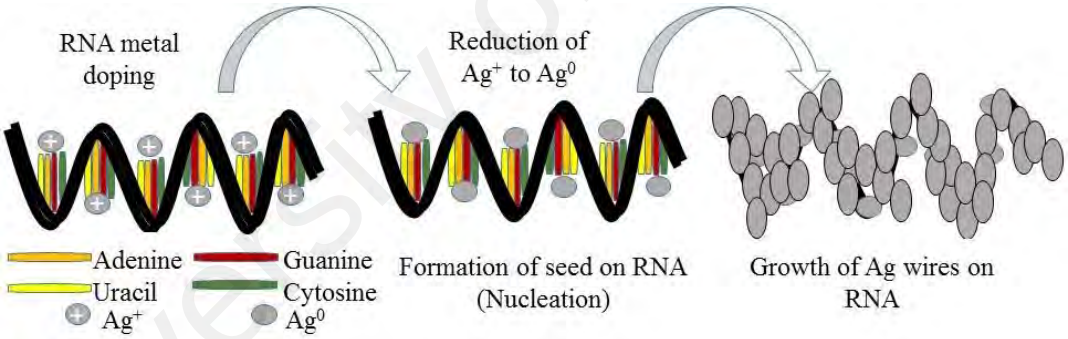

Figure 4.5: Proposed schematic of nucleation mechanism of RNA templated AgW.

After doping of the RNA molecules, a droplet was placed on the surface of substrate. The droplet was allowed to dry, which leaves behind a jelly-like film and the scribe or cut made through the center of the film. Differential evaporation rates across the droplet induces capillary force leading to the evaporation of water from the edges of the cut. Evaporation from the cut causes diffusion of water from bulk to the edge of the scribe. Henceforth, Ag-loaded RNA complexes are dragged towards the edge by water molecules following the coffee-ring effect (Chen et al., 2009; Vengadesh et al., 2015). Meanwhile,

the AgNPs are reduced at the backbone of RNA and form nucleation sites for clustering and growth of additional AgNPs to form AgW. The proposed growth mechanism is shown is Figure 4.5.

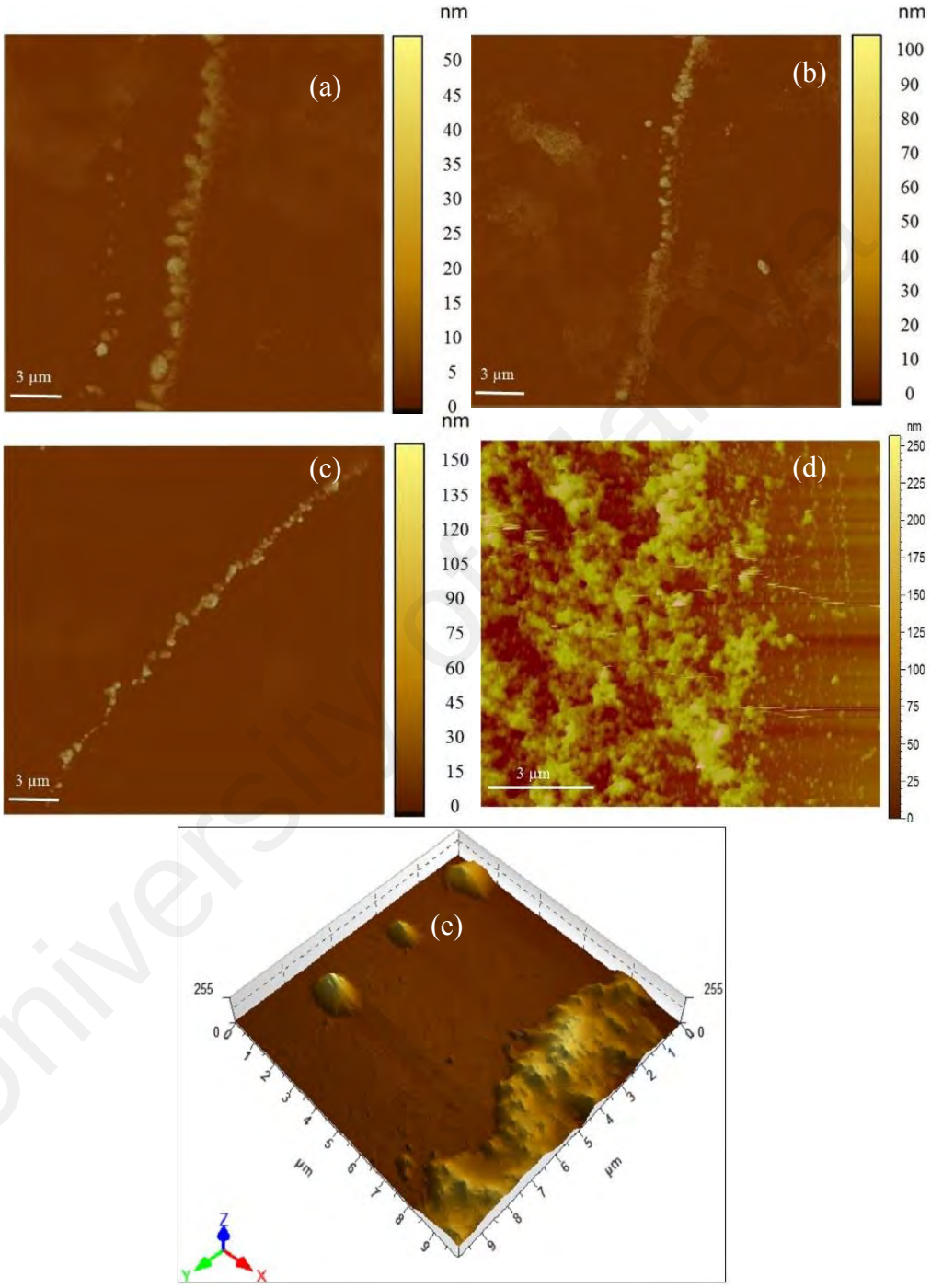

Figure 4.6: AFM images showing Ag-RNA wire fabrication process at different reaction times (a) 15 mins (height 50 nm) (b) 2 hours (height 100 nm) (c) 24 hours (height 250 nm), (d) well connected Ag wires after RNA removal (height 250 nm) and (e) 3-D structure of Ag wires.

The growth and morphology of RNA templated Ag wires were further studied using AFM. AFM images of the films were taken over a range of reaction times after scribe was made on to the semi-dry film. Figure 4.6(a) shows the Ag-RNA complexes that were formed during incubation, diffusing towards the scribe due to differential evaporation rates. The height of the complexes is 50 nm and it is observed to be increased with increase in reaction time up to 250 nm. Moreover, the diffusion towards the edge of the scribe and cluster formation can also be observed with increase in reaction time. The average particle size of AgNPs used in this study is 10 nm and at 15-minute reaction time, the height of the Ag-RNA complexes is 50 nm. This confirms the doping of RNA and formation of seed sites for the growth of the wire. Furthermore, most of the growth process takes place once the Ag-RNA complexes deposit around the edges of the scribe.

Morphological evolution stopped after 24 hours indicating achievement of maximum growth of the Ag wires (Figure 4.6(c)). These results were consistent with FESEM results. Connected Ag wires along the cut with granular morphology can be observed in Figure 4.6(d). Height measurements show heights ranging from 100 to 250 nm, width approximately 8 nm and the length depending on the length of the scribe. Figure 4.6(e) shows AFM image illustrating 3D structure and height profile of clean AgW. The images, in accordance with the FESEM images, show high material density along the edges of the cuts at both sides as a result of capillary force driven diffusion. However, the evaporation from different regions of film forms surface tension gradient causing Marangoni flow in the film, which resists the deposition and cause back-flow of Ag-RNA complexes (Yunker et al., 2011). Such a phenomenon can be observed in Figure 4.6(e) where few Ag-RNA complexes have deposited elsewhere. This phenomenon can be controlled by reducing surface tension using a suitable surfactant.

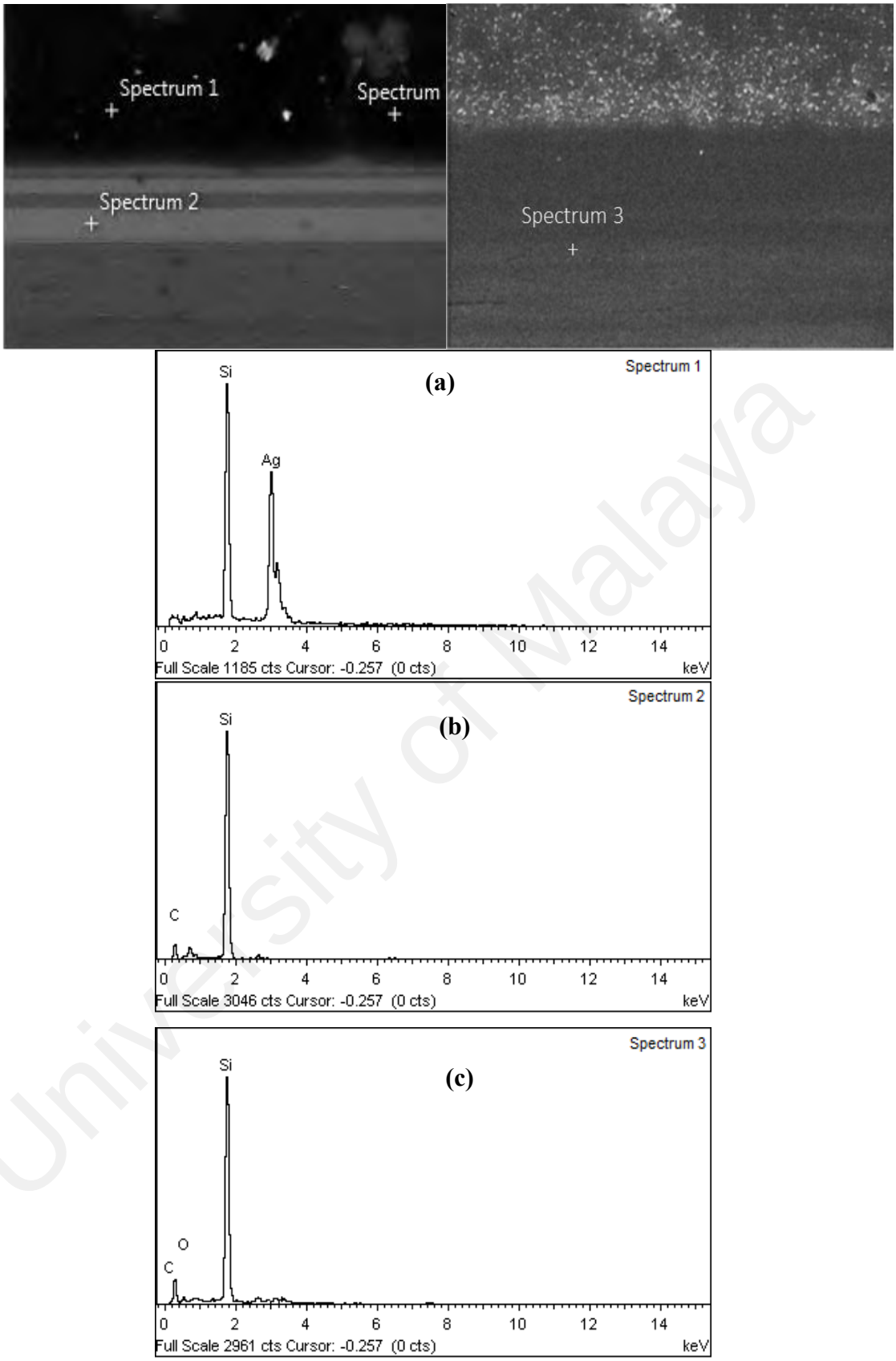

Figure 4.7: Elemental analysis using EDX showing distribution of elements. The graphs demonstrate the distribution of Ag at three different spots (a) along the wire, (b) along the cut and (c) away from the cut or interior of the scribed and cleaned film.

Elemental composition graphs are shown in Figure 4.7, demonstrating successful formation of clean Ag wire along the cut. It is shown that along the edges of the scribe, a significantly high percentage of Ag is present as compared to other regions. Elemental distribution of Ag is highlighted in the Figure 4.7(a) along the wire, (b) along the cut and (c) away from the cut. The Ag signals can only be observed along the edge of the scribe owing to the natural capillary force driven diffusion of silver cations along with the RNA molecules.

4.1.2.2 FTIR Studies on Binding of AgNPs to RNA

To study the binding of AgNPs to RNA molecules, FTIR spectroscopy was conducted. The FTIR spectra (Figure 4.8) for RNA film shows the several prominent characteristic vibrations for RNA at 1240 cm^{-1} assigned to PO_2 asymmetric stretching of RNA backbone, 1488 cm^{-1} assigned to base pair C, 1608 cm^{-1} assigned to base pair A, 1654 cm^{-1} assigned to base pairs U, G, A and C and 1698 cm^{-1} assigned to base pair G and U (Movasaghi et al., 2008; Neault & Riahi, 1997; Zucchiatti et al., 2016). The vibration at 1240 cm^{-1} corresponds to the A-form RNA which shows no significant shift in intensity on interaction with AgNPs, implying no conformal transition occurred for RNA. However, spectral changes can be observed for the band of base pairs U, G, A, C and base pair G and U. The band for U, G, A, C assigned at 1654 cm^{-1} shifted towards lower frequency at 1647 cm^{-1} with a change in intensity and the band for G and U (1698 cm^{-1}) shifted to higher frequency at 1700 cm^{-1} with a slight change in intensity.

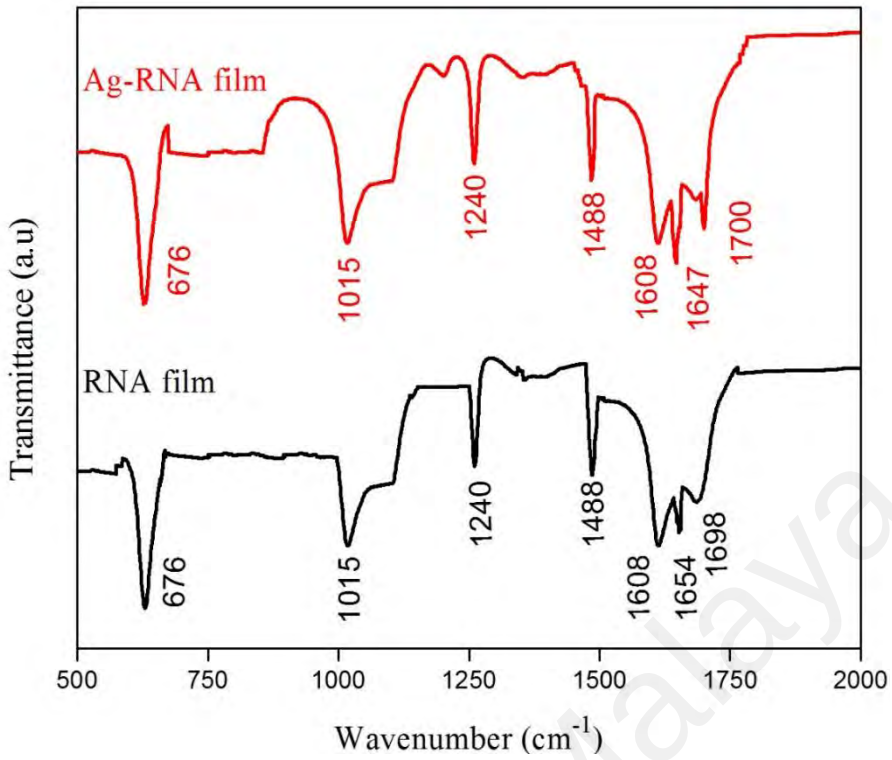

Figure 4.8: FTIR spectra of RNA and AgNPs-RNA film.

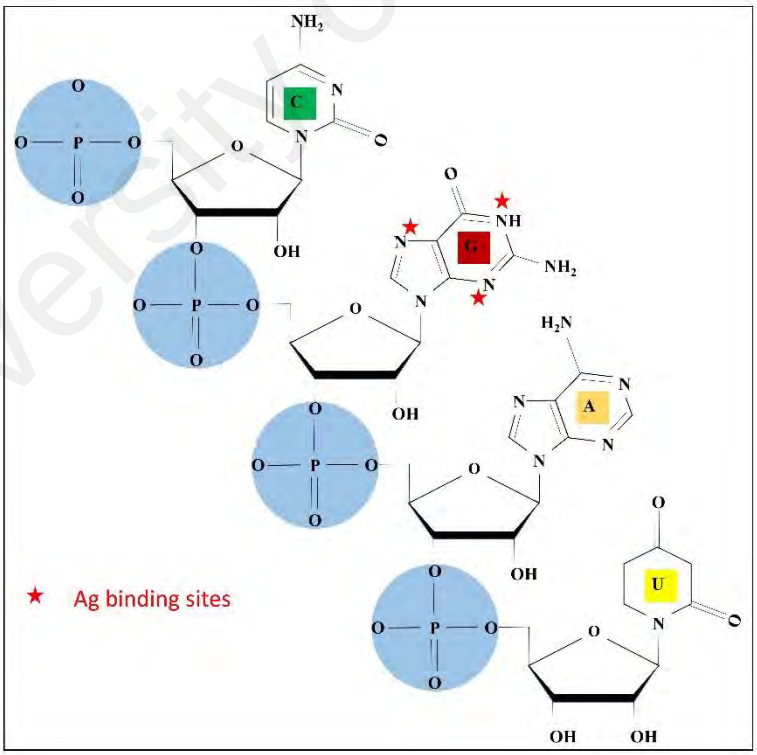

Figure 4.9: Binding sites for AgNPs on RNA determined using FTIR spectroscopy.

This could be attributed to the binding of AgNPs to G bases. Arakawa et al. (2001) observed similar binding of Ag^+ with RNA via G N_7 and O_6 atoms (Arakawa et al., 2001). Figure 4.9 shows the structure of RNA nucleobases and phosphate-sugar backbone of RNA. The red star on G N7 atoms represents the binding sites for AgNPs based on FTIR spectroscopy results.

4.1.2.3 Structural Analysis of Fabricated AgW based on XRD Results

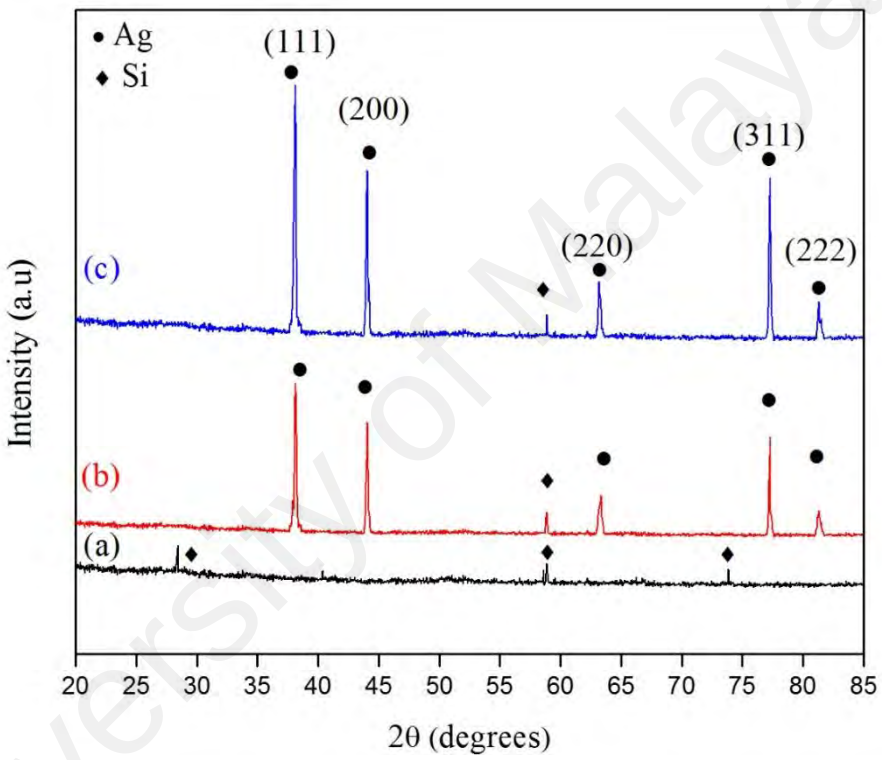

Figure 4.10: XRD graph of (a) RNA film, (b) AgNPs-RNA film and (c) cleaned AgW/Si.

XRD graph of AgW/Si shows characteristic peaks at 38.1, 44.09, 63.36, 77.29 and 81.31° corresponding to the (111), (200), (220), (311) and (222) reflection planes, respectively (Figure 4.10). All the peaks are indexed to facets of face centered cubic (fcc) crystalline structure of Ag (JCPDS No. 4-0783) (Khan et al., 2011). Some small peaks due to Si substrates can be noted in all films at 28.45 and 58.87° (Chong et al., 2013). The XRD peaks for AgW/Si and AgNPs-RNA/Si are identical, however, an increase in

intensity of the AgW/Si can be observed attributed to the removal of RNA scaffold. No oxide peaks were observed in XRD and FTIR spectra.

Scherer equation (4.1) was used to calculate the crystallite size of the fabricated AgW using data from the most intense deflection peak at 38.1°. The mean crystallite size of the RNA templated AgW was calculated to be 150 nm, which depicts that the material is in sub-micron range i.e. microcrystalline structure of AgW. The difference in the mean crystallite size of the AgNPs (40 nm, Section 4.1.1) and AgW (150 nm) supports the role of RNA in templating, nucleating and clustering the AgNPs to AgW. Reduction of AgNPs at RNA and use of wet solvent condition (presence of water) could lead to formation of oxides with silver on the surface of the film. However, no oxide peaks could be identified in XRD spectra, no oxide peaks were present in XRD spectra of AgNPs as well (Section 4.1.1).

4.1.2.4 Electro-catalytic Analysis of the RNA Templated AgW/Si

I-V measurements were carried out on glass substrate with pre-deposited gold electrodes. I-V results of scribed and cleaned AgW/glass substrate at room temperature (Figure 4.11) show ohmic behavior and good electric conductivity. The non-scribed Ag-RNA film on the glass substrate however, interestingly shows a semiconducting behavior suggesting the possibility that the presence of RNA might contribute to this novel discovery. RNA as a semiconducting material has recently been confirmed by series of experiments conducted in our laboratory and its application as an electronic diode has recently been patented (Periasamy., 2016).

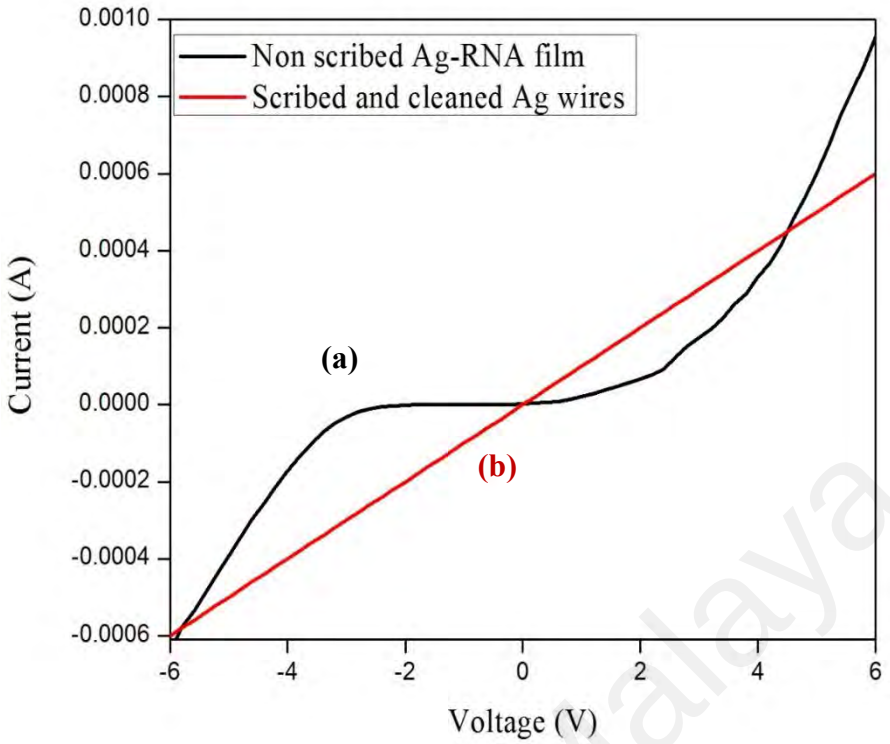

Figure 4.11: I-V characteristics of (a) Ag-RNA film before scribing and (b) after the formation of clean Ag wires.

To analyze the electrochemical behavior of the studied samples for their application as CEs in DSSCs, CV technique was employed at a scan rate of 100 mVs^{-1} (Figure 4.12). Two pairs of quasi reversible redox peaks can be observed for Si and AgW/Si CEs, in which AgW/Si CE exhibited maximum redox behavior attributed to large surface area of AgW/Si and high electrical conductivity achieved due to conductive AgW on Si substrate.

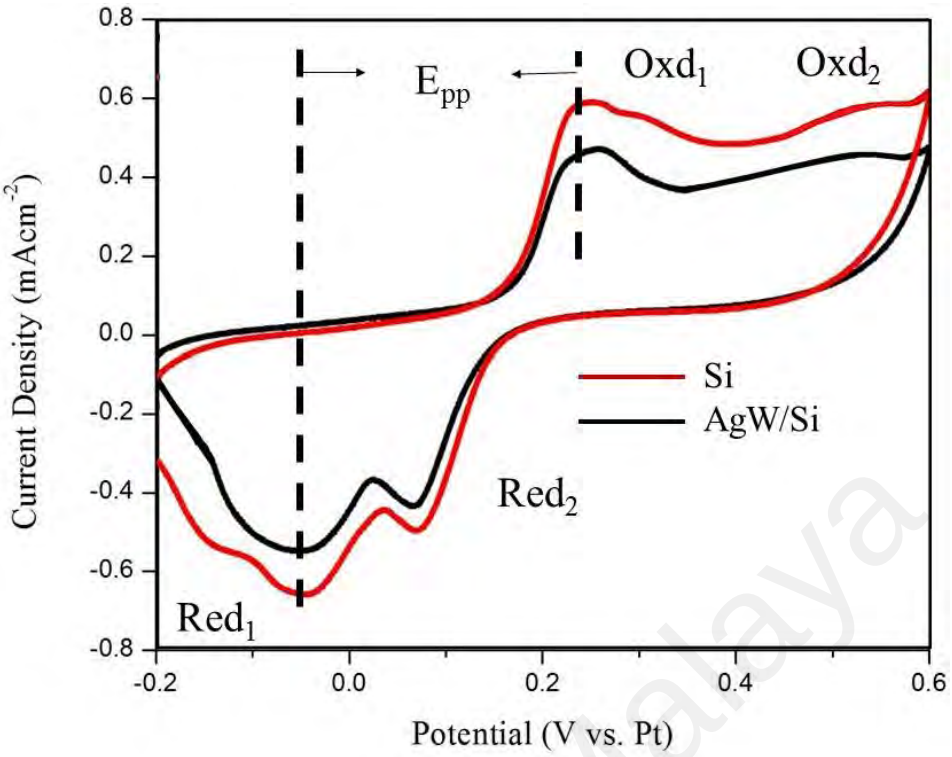

Figure 4.12: CV curves of Si and AuW/Si CEs at a scan rate of 100 mVs^{-1}.

Two sets of redox peaks can be observed in the curves; left redox peaks were due to reaction 1 (Reduction 1, Oxidation 1; Equation 4.2), while the redox peaks at the right were due to reaction 2 (Reduction 2, Oxidation 2; Equation 4.3).

$I_3 + 2e^- \leftrightarrows 3I^-$ ……. (Reaction 1) (4.2)

$3I_2 + 2e^- \leftrightarrows 2I_3^-$ …… (Reaction 2) (4.3)

One of the most important functions of CE is to catalyze the reduction of tri iodide ions to iodide ions and the left pair of peaks (Red_1) are critically important for performance of CEs (Dao et al., 2011).

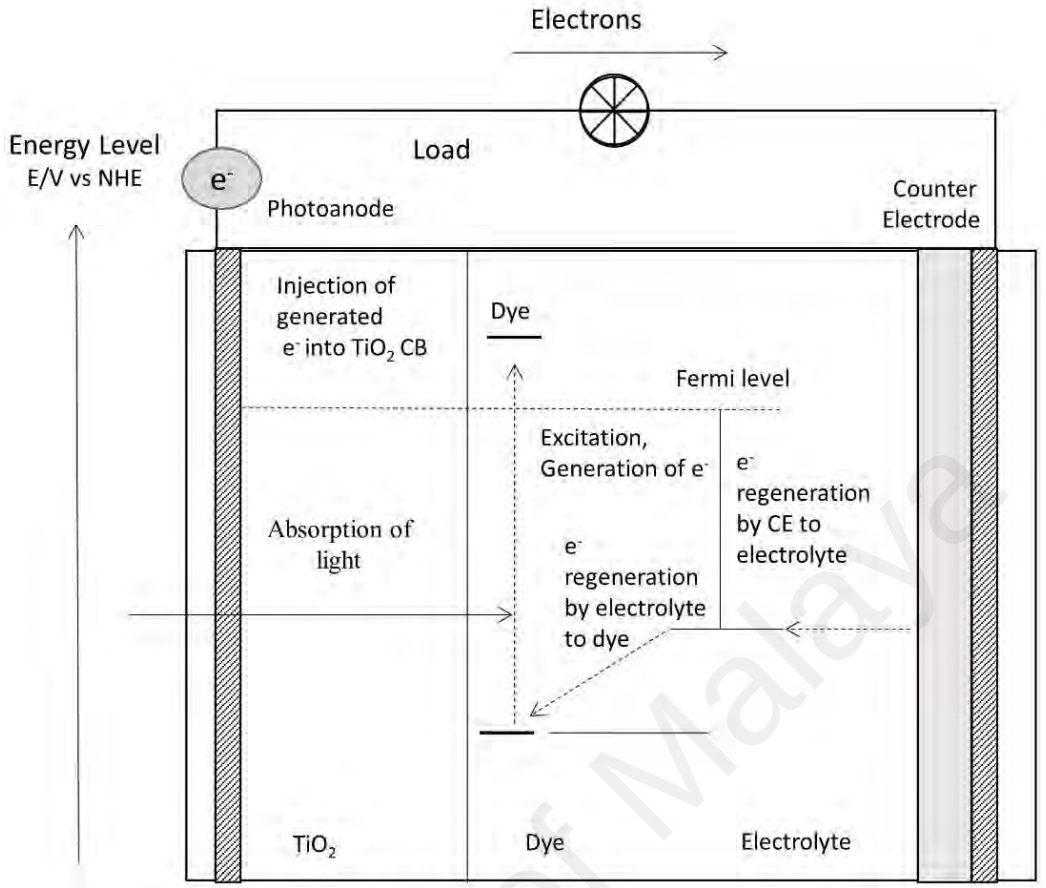

Figure 4.13: Schematic diagram illustrating the function of the CE.

The function of CE has been illustrated in Figure 4.13. In this regard, peak current density is an important parameter to analyze the catalytic activity of the CE. High current at fixed voltage is an indication of a stronger reaction (Ramasamy & Lee, 2010). Notably, AgW/Si CE possess maximum current density of 0.60 $mAcm^{-2}$ (Table 4.1). Another parameter to analyze the catalytic activity of the CEs is the peak to peak separation (E_{pp}). Electrochemical constant (k_s) and E_{pp} are inversely proportional to each other and therefore, smaller the E_{pp}, higher are the catalytic properties (Dao & Choi, 2015; He et al., 2014). J_{Red1} values (Table 4.1) show that the presence of AgW on Si CE has promotion effect on electro-catalytic activity of the CE. This could be attributed to the increase in the quantity of bonding sites which ensures rapid charge transfer, decrease in the I_3^- reduction over potential and enhancement in the reaction kinetics. However, the E_{pp} value is same for both CEs.

Table 4.1: Summary of photovoltaic and catalytic properties of DSSCs and CEs.

Sample	Solar cell characteristics				CE	
	V_{oc} (V)	J_{sc} (mA)	FF	η (%)	J_{Red1} ($mAcm^{-2}$)	E_{pp} (V)
Si	0.44	2.1	0.62	0.58±0.02	0.45	0.2
AgW/Si	0.49	3.5	0.68	0.96±0.03	0.60	0.2

4.1.2.5 J-V Characteristics of DSSCs based on AgW/Si CE

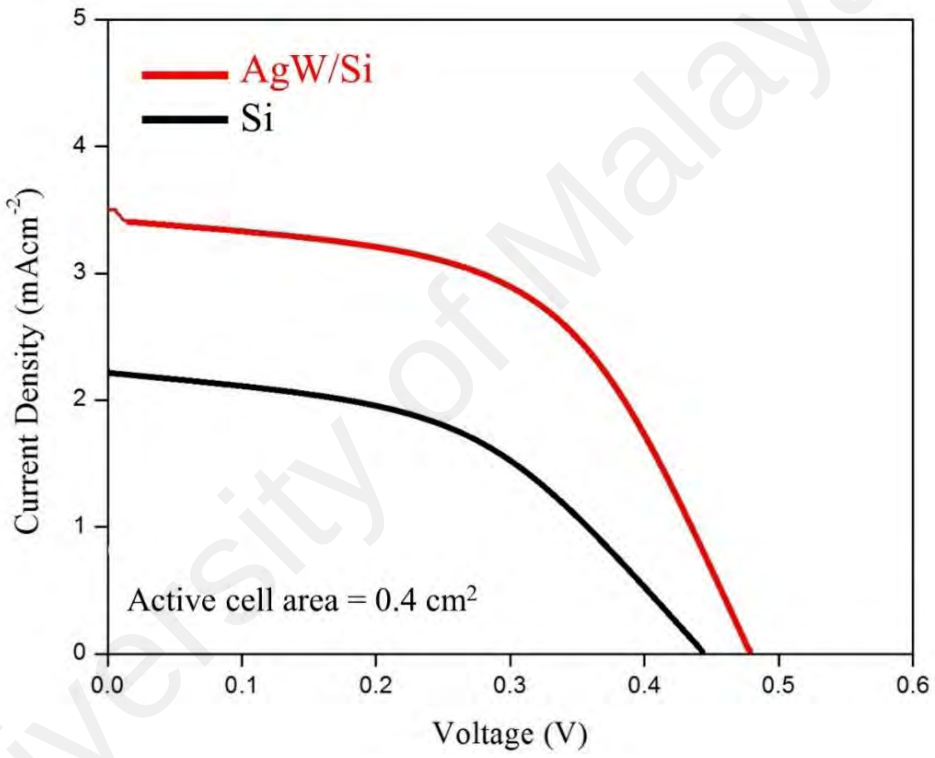

Figure 4.14: J-V curves of DSSCs based on Si and AgW/Si CEs.

J-V characteristics of the DSSCs fabricated using identical photoanodes and studied CEs are shown in Figure 4.14, and summarized in Table 4.1. It can be observed that using AgW/Si as a CE increased the V_{oc}, J_{sc} and overall efficiency of the DSSC. The presence of well-connected AgW on Si enhances the performance of the CE which led to higher catalytic reduction of the iodide ions in the electrolyte. Moreover, quick reduction of

iodide ions of redox electrolyte suppresses the recombination at the electrolyte/CE interface, thereby enhancing the performance of the DSSCs.

The novel technique used in this study demonstrates the promising prospects of an easy and highly controllable fabrication of conductive AgW on Si wafer. Results show the successful removal of the RNA residue using simple and cost-effective cleaning method to yield clean Ag wires with heights ranging from 100 to 250 nm. The doping of RNA with AgNPs led to reduction of Ag, which served as nucleation sites for the growth of the wires. AgNPs bind with G nucleobases of the RNA. The presence of AgW on Si enhanced the catalytic activity of the substrate and showed an increase in the overall performance of the solar cells when used as a CE in DSSCs.

Based upon all the results discussed above, two factors can be observed contributing to the limitation of the work; formation of the wires in sub-micron scale and the Marangoni effect hindering the complete deposition of the AgW on the edges of the scribe. Therefore, next study was conducted to control the Marangoni effect by addition of surfactant.

4.1.3 Studies on DNA Templated AgW/ITO and Effect of SDS Surfactant

DNA and RNA have significant resemblance in their structure, but the main difference lies in the structure of their strands. DNA has a double helix structure in contrast to RNA, which generally possess single helix structure (Section 2.1). In RNA templated Ag wires, we observed that RNA played a vital role in arrangement of the AgW on Si wafer. In this section, we have studied the role of DNA in metal templating on ITO substrate and probed its use as a CE in DSSCs. The fabricated DNA templated Ag wires were structurally, morphologically and electrically characterized. Moreover, their performance as CE was also analyzed using CV and J-V studies. Meanwhile, the effect of addition of SDS surfactant was also studied.

4.1.3.1 Morphological and Elemental Analysis

SDS surfactant was used in order to combat Marangoni effect and the effect of different concentration of SDS on morphology of the templated AgW was studied, as shown in Figure 4.15. SDS is an anionic surfactant with net negative charge. However, the quantity of SDS used was observed to be a key factor in affecting the templating process due to two reasons. Firstly, SDS is a detergent which can denature proteins (Weber & Osborn, 1969). High quantity of SDS present in Ag-DNA solution could lead to denaturing of DNA, which could hinder the scaffolding role of DNA. Secondly, SDS carry a negative charge, therefore large amounts of SDS in Ag-DNA solution could result in distorting the interaction of AgNPs and DNA and their binding. It can be clearly observed from Figure 4.15(a, b, c**)** that using low concentration of SDS had promotional effect of the fabrication of templated AgW and controlling the Marangoni effect. However, as the quantity of the SDS was increased in the Ag-DNA solution, the templating process was deteriorated (Figure 4.15(b and c)). For further studies and characterizations, samples fabricated with 0.2 mM concentration of SDS were used.

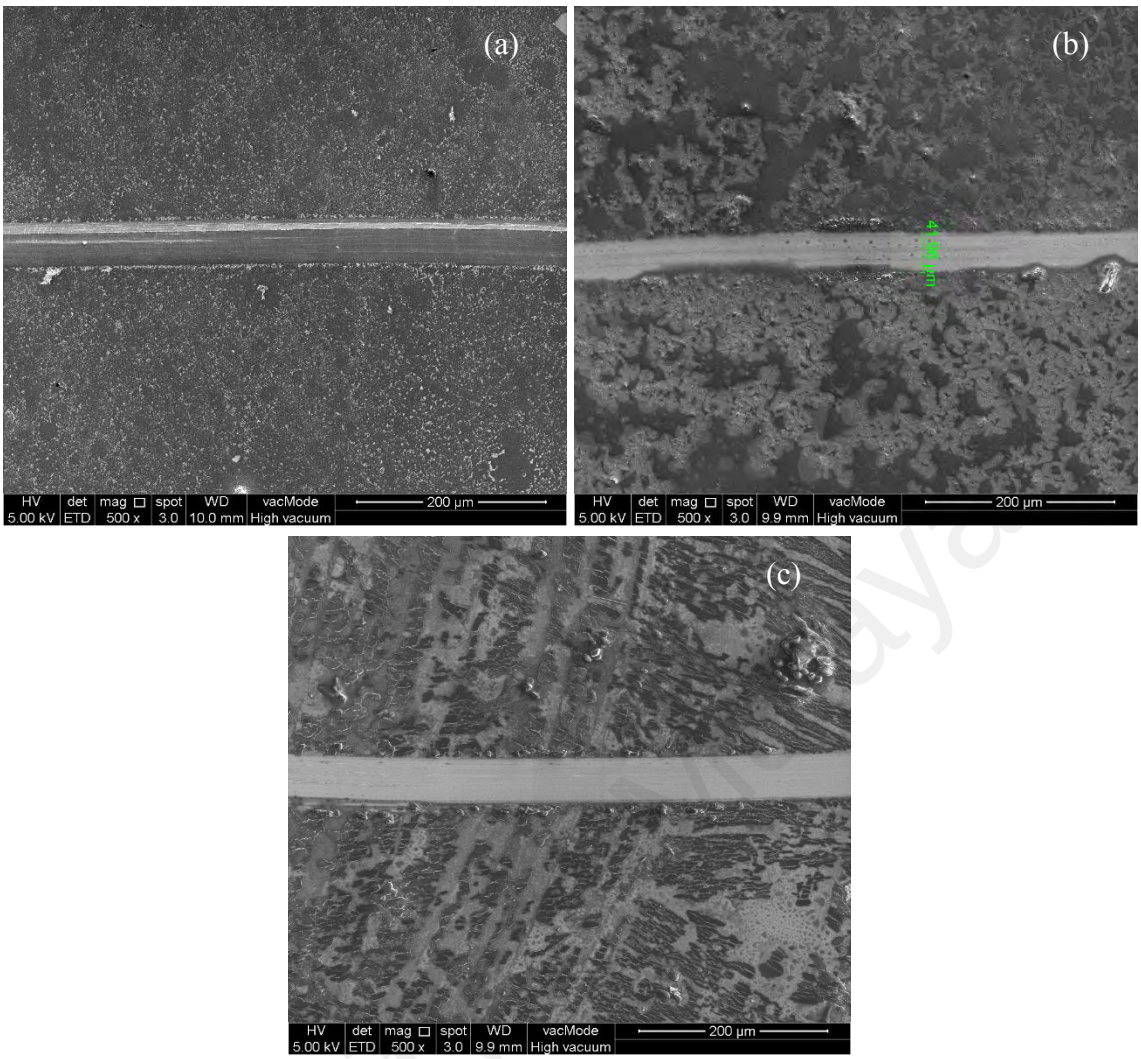

Figure 4.15: Non-cleaned and scribed Ag-DNA films with addition of SDS surfactant at concentrations (a) 0.2 mM, (b) 0.4 mM and (c) 0.6 mM.

The self-assembled morphology of DNA can be seen in FESEM image of DNA solution on ITO, (Figure 4.16(a)) and the well-separated AgNPs were observed throughout the ITO matrix as evident from the FESEM image of AgNPs/ITO (Figure 4.16(b)). Negative control is shown in Figure 4.16(c**)** in which the AgNPs film on ITO was scribed without binding it with DNA. A very insignificant amount of Ag deposition can be observed around the edges of the scribe. This emphasizes on the importance of DNA scaffold which aids in the formation of connected AgW on ITO. The hybrid formation of AgNPs with DNA leads to the formation of an arbitrary network along the rough surface as shown in Figure 4.16(d).

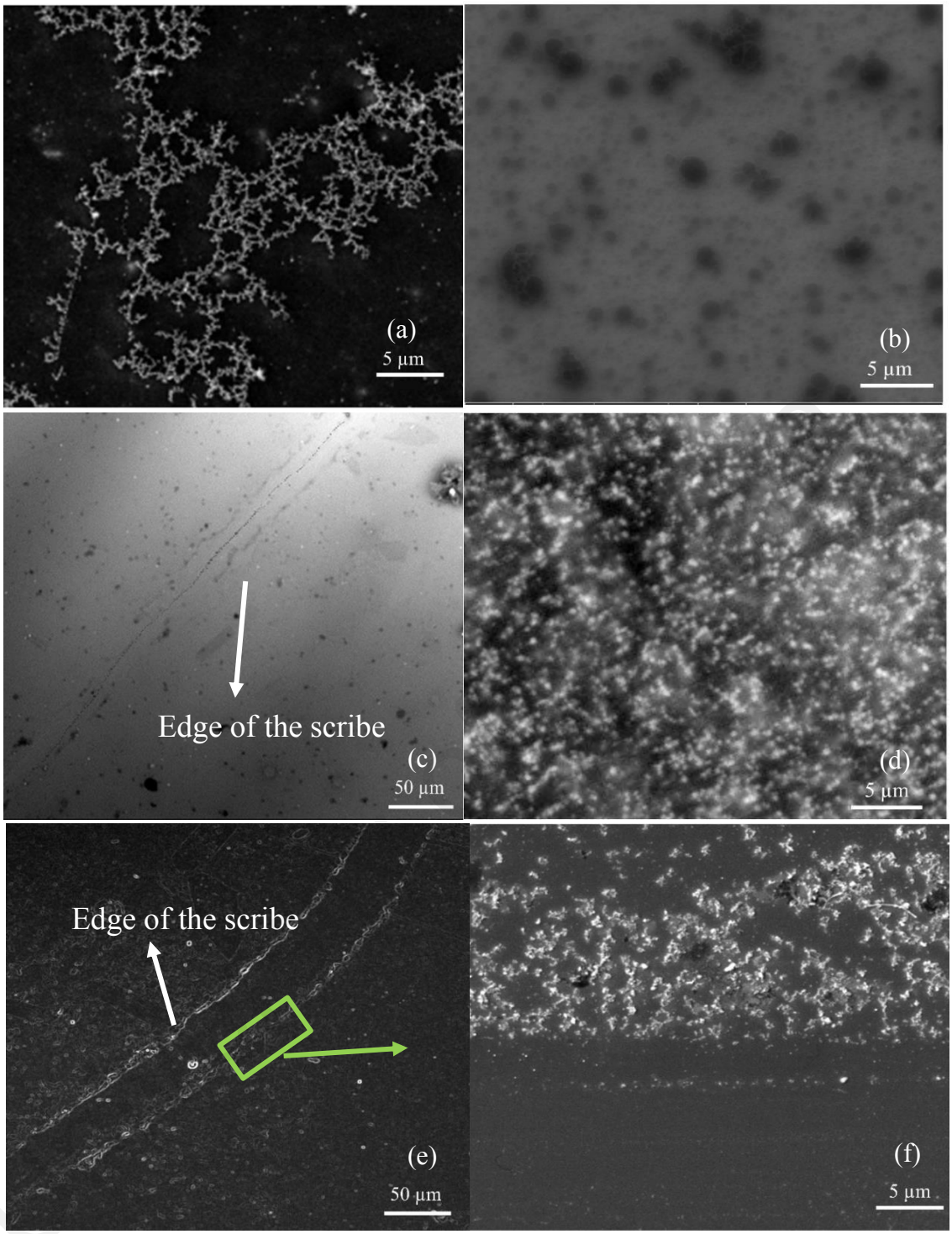

Figure 4.16: FESEM images showing (a) DNA solution drop-casted on ITO (b) drop-casted AgNPs, (c) scribed AgNPs drop-casted without DNA (d) formation of AgNPs-DNA complexes, (e) scribed and etched AgW around the scribe and (f) high magnification FESEM image of AgW on ITO.

Scribing and etching processes of DNA in Ag-DNA/ITO generated AgW with the high aspect ratio for AgW/ITO at the edges of both sides of scribe with a high material density**.** Figure 4.16(e) shows a lower magnification image depicting the deposition of AgW along the edges of the scribe. Figure 4.16(f) meanwhile shows high magnification image of the AgW formed after enzymatic etching and removal of the DNA scaffold. The observation is in good agreement with the "coffee-ring" effect and the natural capillary force allowed the diffusion of Ag-DNA towards the edge of the scribing region and conscripted its deposition along the scribed patterns (Deegan et al., 1997).

Fabrication of AgW on ITO involves four major steps; (1) the binding of AgNPs with DNA, (2) self-assembling of Ag-DNA complexes, (3) scribing the circuitry and (4) removal of DNA *via* enzymatic etching. The formation of wire structure on DNA follows same reduction, nucleation and growth route explained for fabrication of RNA templated Ag wires (Section 4.1.2). Marangoni flow observed in the previous studies was controlled using SDS surfactant. Addition of surfactant reduced the surface tension in the film thereby, ensuring the complete diffusion of the Ag-DNA complexes towards the edges of the scribe. Dai et al. (2005) studied the DNA patterns as templates with AgNPs to form uniform Ag nanopatterns and observed similar template directed nucleation and growth mechanism (Dai et al., 2005).

Ag-DNA/SDS film on ITO possessed gel-like nature, which allowed the mobility of Ag-DNA complexes towards the scribe due to the capillary flow from the edges of scribe. The enzymatic etching and washing samples with DI water yielded clean AgW on ITO. Self-assembly, nucleation and growth of AgNPs along the scribe due to DNA scaffold enabled the formation of conducting wires in sub-micron to nanoscale range (height 60-100 nm) as evident from AFM image (Figure 4.17). Meanwhile, the proposed nucleation and growth mechanism has been illustrated in Figure 4.18.

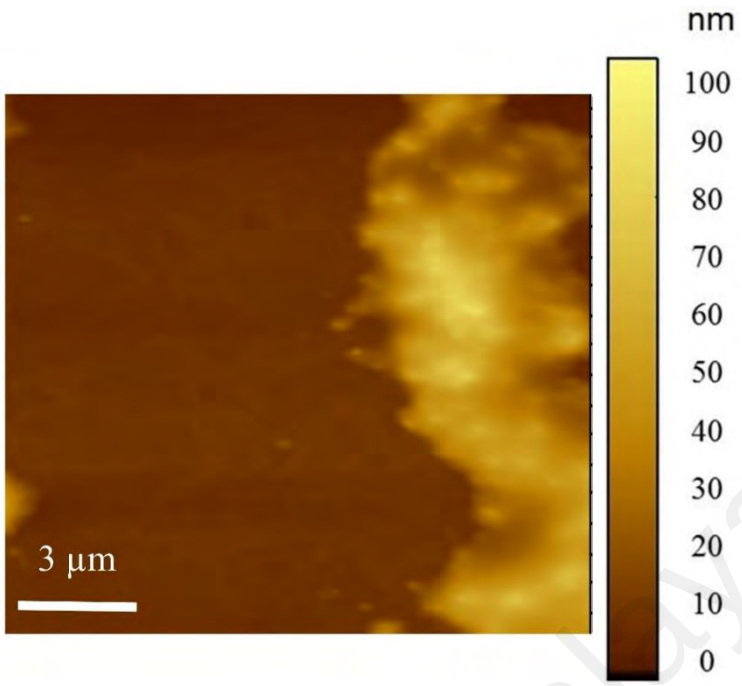

Figure 4.17: AFM image showing diameter of the fabricated wire (60-100 nm).

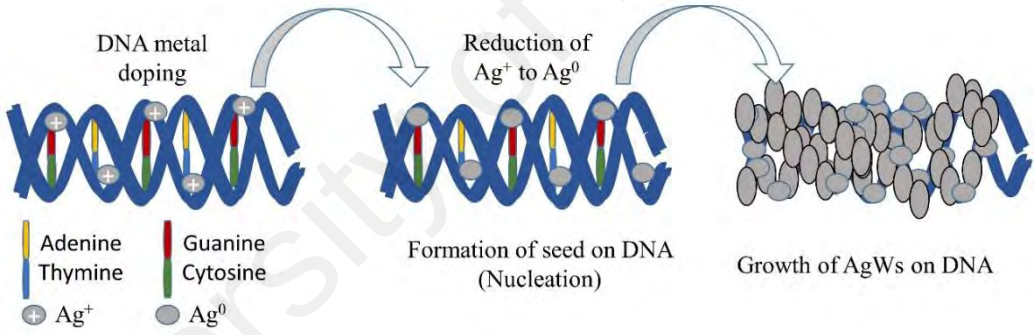

Figure 4.18: Proposed growth mechanism of DNA templated AgW.

Figure 4.19 shows the elemental composition of the films and their corresponding spectra. It is evident that DNA acts as a scaffold in arranging and assembling the wires along the scribe prior to removal or etching to obtain clean AgW on the substrate. EDX pattern of AgNPs-DNA/ITO displayed carbon (C) (25 at.%), oxygen (O) (35 at.%) and Ag (40 at.%) elements as shown in Figure 4.19(a), in which C and O are the constituents of DNA. AgNPs/ITO showed only the presence of Ag (100 at.%) (Figure 4.19(b)). Removal of DNA template from Ag-DNA/ITO was confirmed from the EDX pattern of AgW/ITO, which exhibited the existence of Ag (98 at.%) and C (2 at%) (Figure 4.19(c))

and the negligible presence of C is attributed to the existence of trace level of DNA in AgW/ITO.

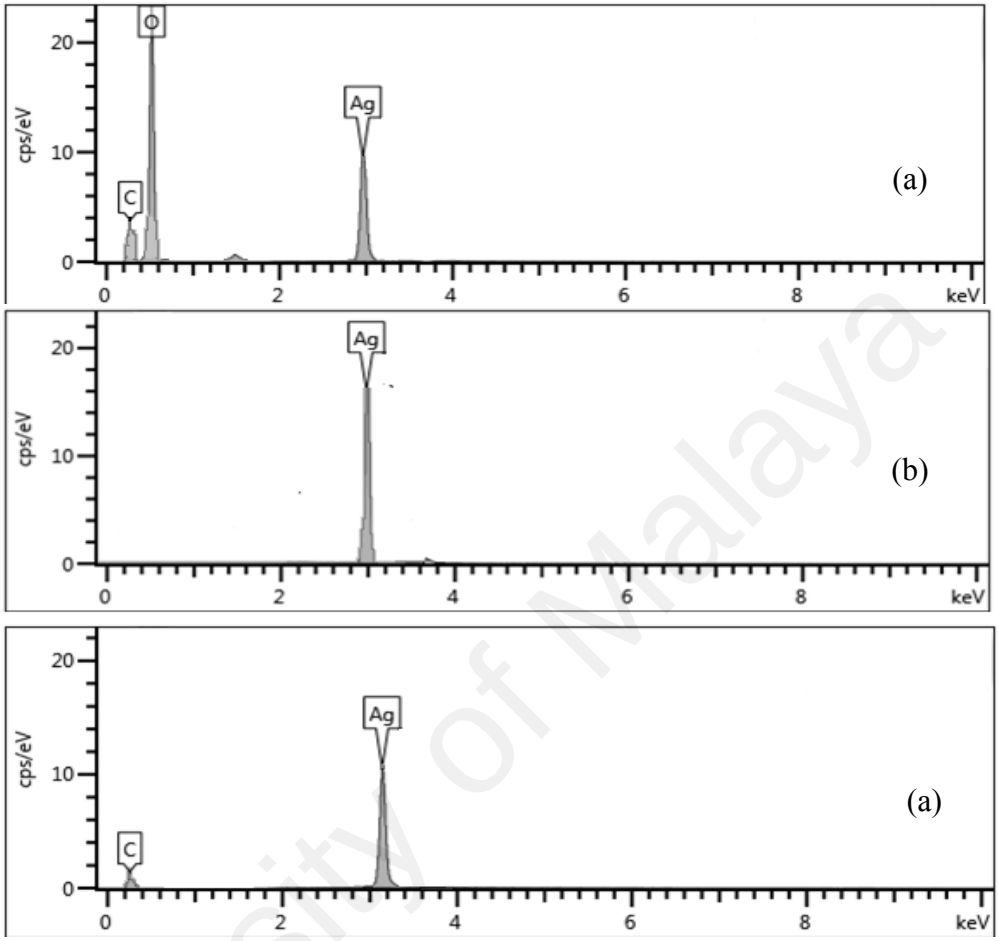

Figure 4.19: EDX spectra of (a) AgNPs-DNA solution film showing presence of DNA along with Ag, (b) scribed AgNPs film and (c) scribed-etched AgW film showing removal of DNA scaffold with etching.

4.1.3.2 Studies on Interaction and Binding of Ag-DNA using FTIR Spectroscopy

The interaction and binding of Ag with DNA was studied using FTIR spectroscopy and is shown in Figure 4.20. Like RNA, DNA also has a tendency of binding metal NPs to different binding locations (Bates et al., 2006; Heddle, 2013). Several spectral changes in terms of intensities and shifting were observed in DNA on binding with Ag. In DNA film, several plane vibrations related to DNA were observed.

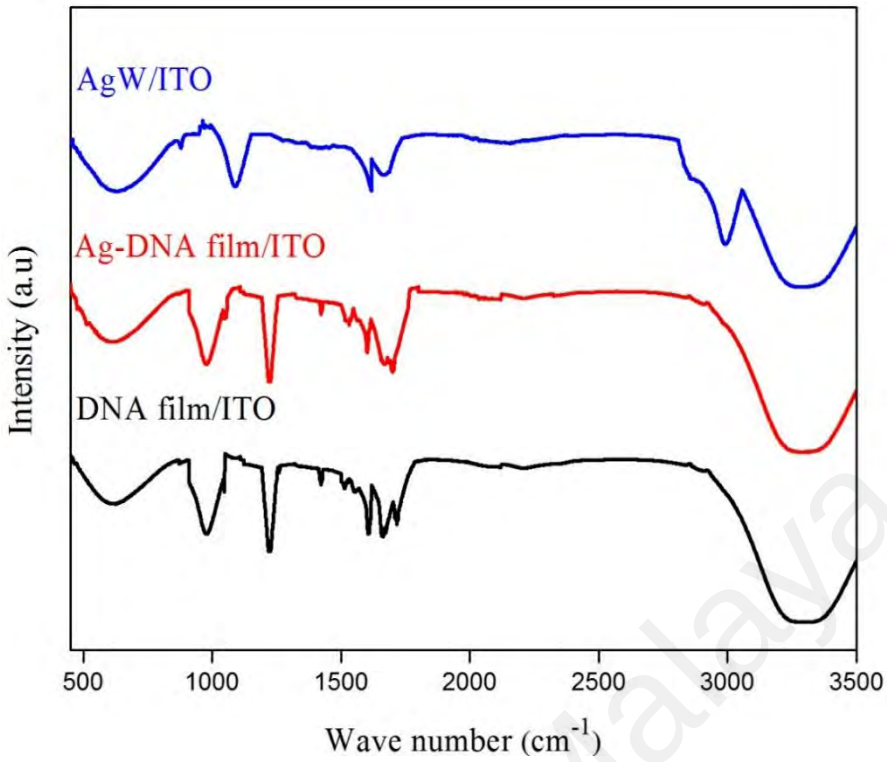

Figure 4.20: FTIR spectra of DNA film, Ag-DNA film and AgW on ITO.

Main bands associated with DNA can be observed; asymetric-stretch of phosphate band at 1222 cm^{-1} which is characteristic for B-form DNA, (A-C) at 1609 cm^{-1}, (G-T) at 1717 cm^{-1}, (T, G, A, C) at 1663 cm^{-1}, back bone (C-C) at 970 cm^{-1} and backbone (C-O) at 1051 cm^{-1} (Hackl et al., 2005; Whelan et al., 2011). The data is summarized in Table 4.2. On interaction of DNA with Ag, main changes can be observed at 1422 cm^{-1}, 1529 cm^{-1}, 1609 cm^{-1}, 1663 cm^{-1} and 1717 cm^{-1}. Bands at 1422 cm^{-1}, 1609 cm^{-1},1663 cm^{-1} and 1717 cm^{-1} were observed to have shifted to lower frequencies at 1400 cm^{-1}, 1600 cm^{-1}, 1656 cm^{-1} and 1700 cm^{-1} respectively. However, the band at 1529 cm^{-1} was shifted to higher frequency at 1531 cm^{-1}. 1422 cm^{-1} appears as a weak absorption at 1400 cm^{-1}. It can be deduced from these results that spectral changes have accured due to the formation of Ag-DNA complexes on binding of Ag to A-T and G-C base pairs of the DNA. Due to the alteration in frequencies of A, T, G and C, it is suggested that on adding Ag to DNA, Ag interchelated between A N1 and T N3 as well as G N1 and C N3 atoms. Moreover, no change in intensities of assymetic and symetric stretching of phosphate groups and

backbone of DNA at 970 cm^{-1}, 1051 cm^{-1}, 1087 cm^{-1} and 1222 cm^{-1} suggests no participation of C-C and C-O as well as phosphate groups of DNA in Ag-DNA binding.

Table 4.2: DNA conformal band assignments and shifts in frequencies on interaction with Ag.

Assignment	DNA film (cm^{-1})	Ag-DNA film (cm^{-1})
Backbone (VC-C)	970	970
Backbone (VC-O)	1051	1051
Symmetric phosphate	1087	1087
Anti-symmetric phosphate	1222	1222
C2'/C3'-endo deoxyribose	1422	1400
Base pair (C)	1529	1531
Base pair(A)	1608	1600
Base pair (T)	1663	1656
Base pair (G)	1717	1700

FTIR graph (Figure 4.20) of AgW shows absorption peaks at 1051 cm^{-1} attributed to carbonyl group (–C=O), 1652 cm^{-1} for C-C streching and 2954 cm^{-1} attributed to the C-H stretching vibrations (Kumar et al., 2015). Absence of peaks due to DNA supports the removal of DNA scaffold on etching. The broad peak in all samples observed at 3438 cm^{-1} is due to the presence of hydroxyl group O-H stretching vibration (Lin et al., 2010). Figure 4.21 shows the structure of DNA nucleobases. The red star on N atoms of G, A, T and C represents the binding sites for AgNPs based on FTIR spectroscopy results.

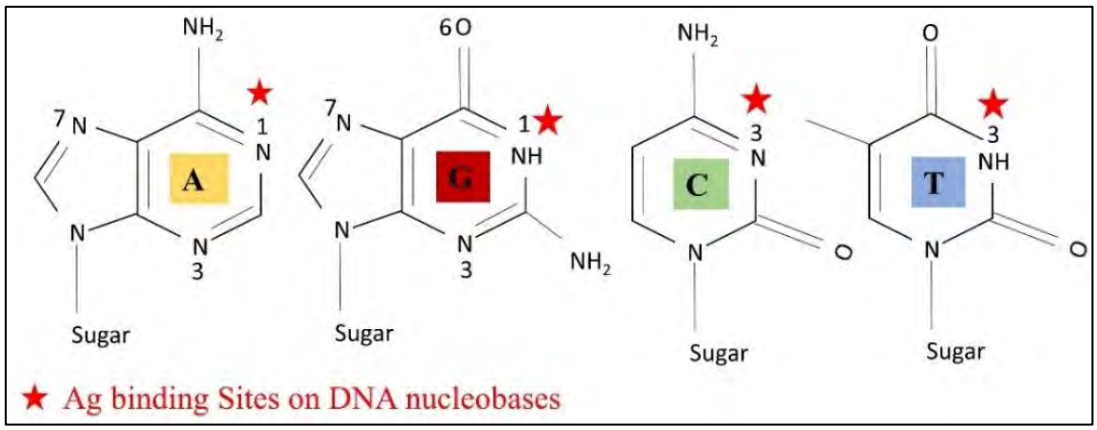

Figure 4.21: Depiction of Ag binding sites to the nucleobases in DNA based on FTIR results.

4.1.3.3 XRD and XPS Analysis of the Fabricated AgW/ITO

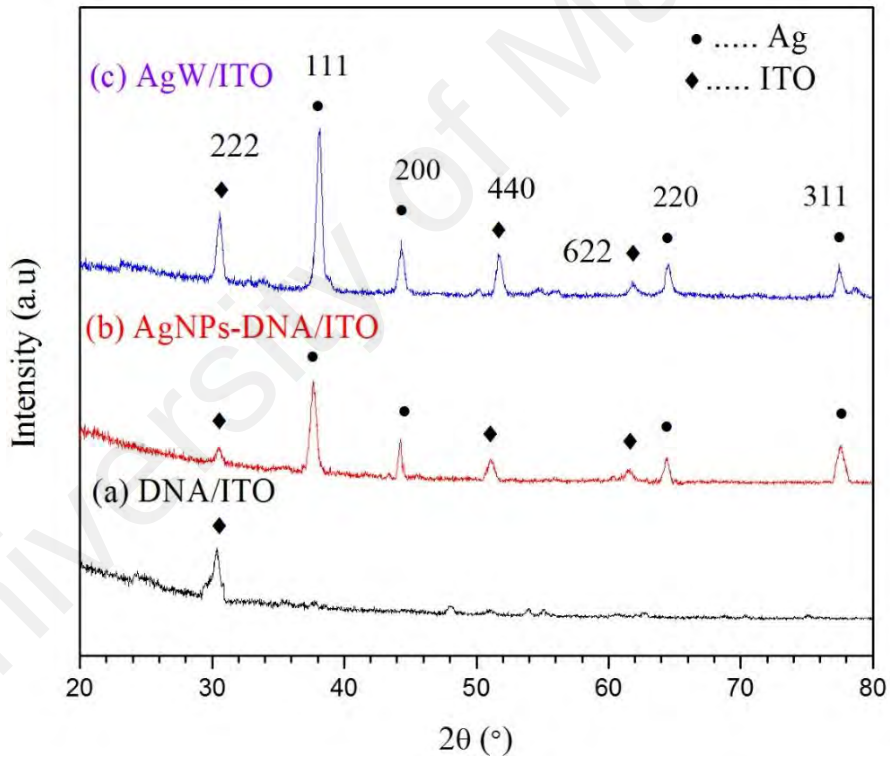

Figure 4.22: XRD spectra of (a) DNA film on ITO, (b) AgNPs-DNA film on ITO and (c) AgW on ITO.

AgW/ITO exhibited the characteristic diffraction peaks at 38.2, 44.5, 64.5, 77.6 and 81.5°, (Figure 4.22), representing the (111), (200), (220), (311) and (222) reflection planes, respectively, of the fcc single crystalline structure of Ag (JCPDS No. 4-0783) (Sathishkumar et al., 2009; Veith et al., 2011). Although the diffraction peaks obtained for AgNPs-DNA/ITO were identical with AgW/ITO, the characteristic intensities of AgNPs were quenched for AgW/ITO, (Figure 4.22(b and c)), owing to the hybrid formation of AgNPs with DNA. The quenched intensities of characteristic diffraction peaks of Ag were released for AgW/ITO, specifying the removal of a DNA template. In addition to Ag peaks, ITO peaks from substrate can be observed at 222, 440 and 622 planes (Veith et al., 2011). The mean crystallite diameter calculated using Scherer equation (Equation 4.1) of the fabricated AgW on ITO was estimated to be 90 nm. This implies that the material formed can be assumed to be in nanoscale. However, that it is a mean diameter, there might be presence of microcrystalline material as well.

The oxidation state and electronic structure of AgW was determined using XPS. Wide scan of clean DNA-templated AgW shown in Figure 4.23(a), reveals the presence of Ag along with trace level peaks of C 1S and O 1S ensuring the complete removal of DNA scaffold. Strong intensities of Ag3d peaks can be observed. The Ag 3d narrow scan spectrum clearly depicts the existence of two distinctive peaks at 368.43 and 374.43 eV, corresponding to Ag $3d_{5/2}$ and Ag $3d_{3/2}$, respectively. The splitting of 3d doublet was found to be 6 eV, specifying the existence of Ag^0 state (Lin & Wang, 2005; Mao et al., 2012).

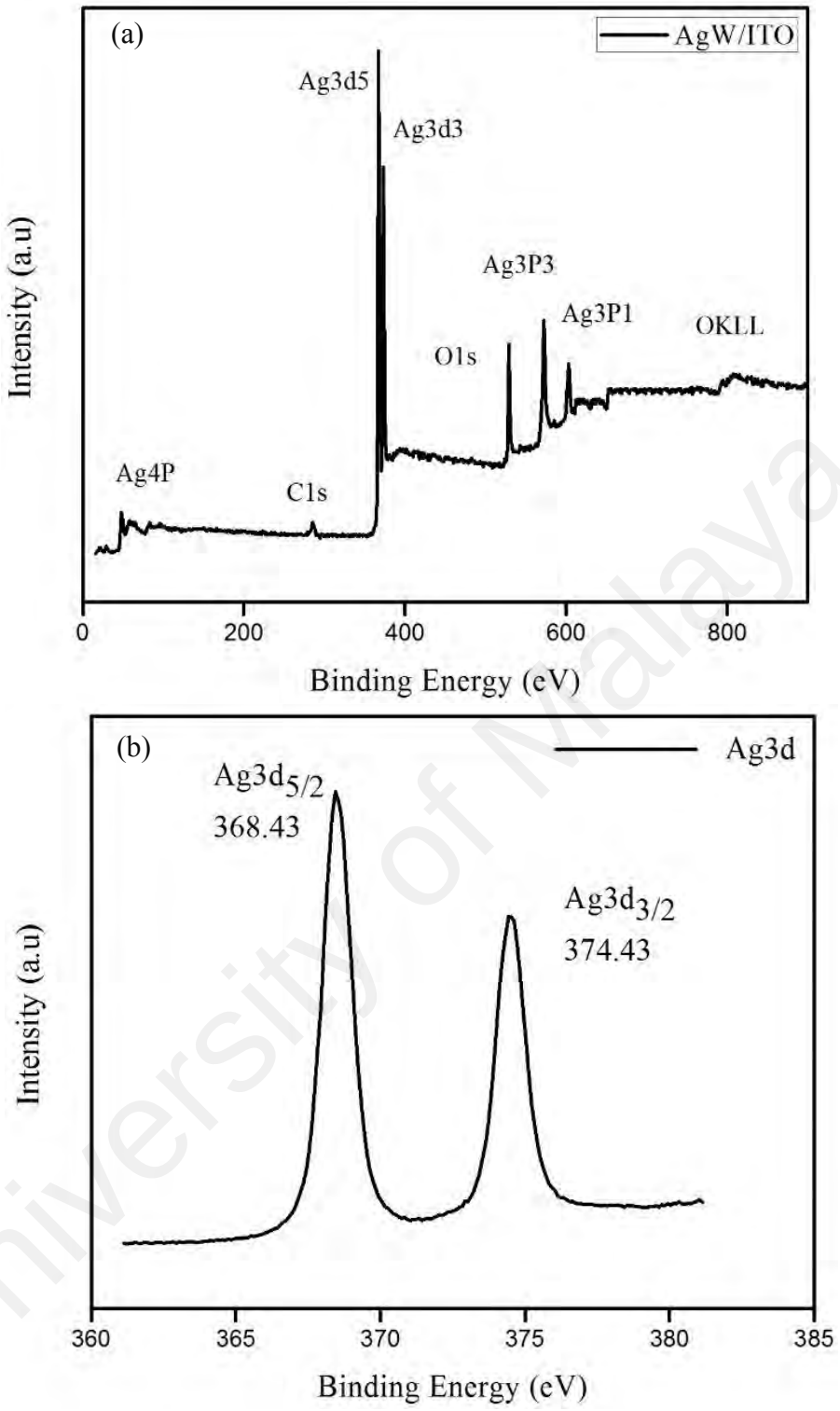

Figure 4.23: (a) XPS wide scan for fabricated AgW and (b) narrow scan for Ag3d.

4.1.3.4 Electro-catalytic Properties of the DNA Templated AgW/ITO

The electrochemical behavior of studied samples was investigated using CV technique at a scan rate of 100 mVs^{-1} and the curves are shown in Figure 4.24. DNA film on ITO and the AgNPs-DNA film on ITO does not exhibit any redox peaks owing to the passive behavior of DNA on ITO. This implies that any amount of DNA left on the substrates was detrimental for their performance as a CE. In contrast, the well-defined two pairs of quasi-reversible redox peaks were observed for AgNPs/ITO and AgW/ITO. Upon the formation of conductive AgW on ITO and successful removal of DNA, AgW/ITO showed maximum redox behavior and J_{Red1} value of 0.39 $mAcm^{-2}$. The E_{pp} value (Table 4.3) of AgW/ITO was slightly less than that of AgNPs/ITO. This indicates the importance of DNA templating in altering the morphology of AgNPs into self-assembled-well-connected AgW, which enhances the catalytic properties of the CEs.

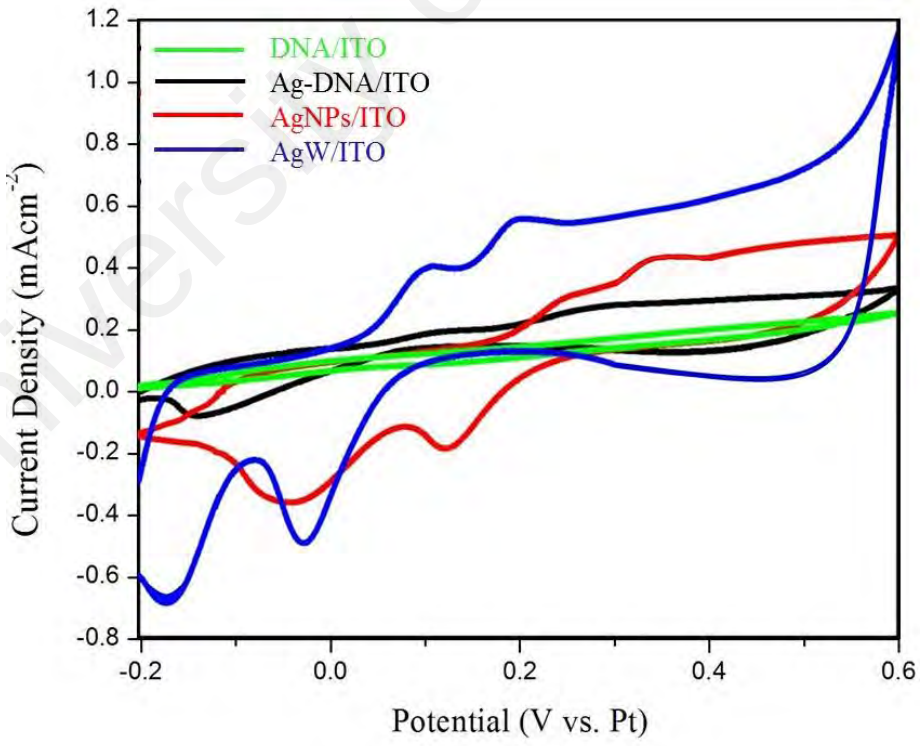

Figure 4.24: CV curves of DNA/ITO, AgNPs-DNA/ITO, AgNPs/ITO and AgW/ITO at a scan rate of 100 mVs^{-1}.

4.1.3.5 J-V Characteristics of DSSCs based on Modified CEs

J-V characteristics of the DSSCs based on fabricated CEs are shown in Figure 4.25, and the results are summarized in Table 4.3. The DSSCs based on AgNPs/ITO and AgW/ITO exhibited efficiency of 0.99 and 1.29 %, respectively. An increase in solar cell characteristics can be observed due to enhanced catalytic performance of AgW modified CE.

Table 4.3: Summary of photovoltaic and catalytic parameters of DSSCs and CEs.

Sample	Solar cell Characteristic				CE	
	V_{oc} (V)	J_{sc} (mA)	FF	η (%)	J_{Red1} ($mAcm^{-2}$)	E_{pp} (V)
AgNPs/ITO	0.50	3.50	0.62	0.99±0.02	0.25	0.20
AgW/ITO	0.52	4.10	0.68	1.29±0.02	0.39	0.19

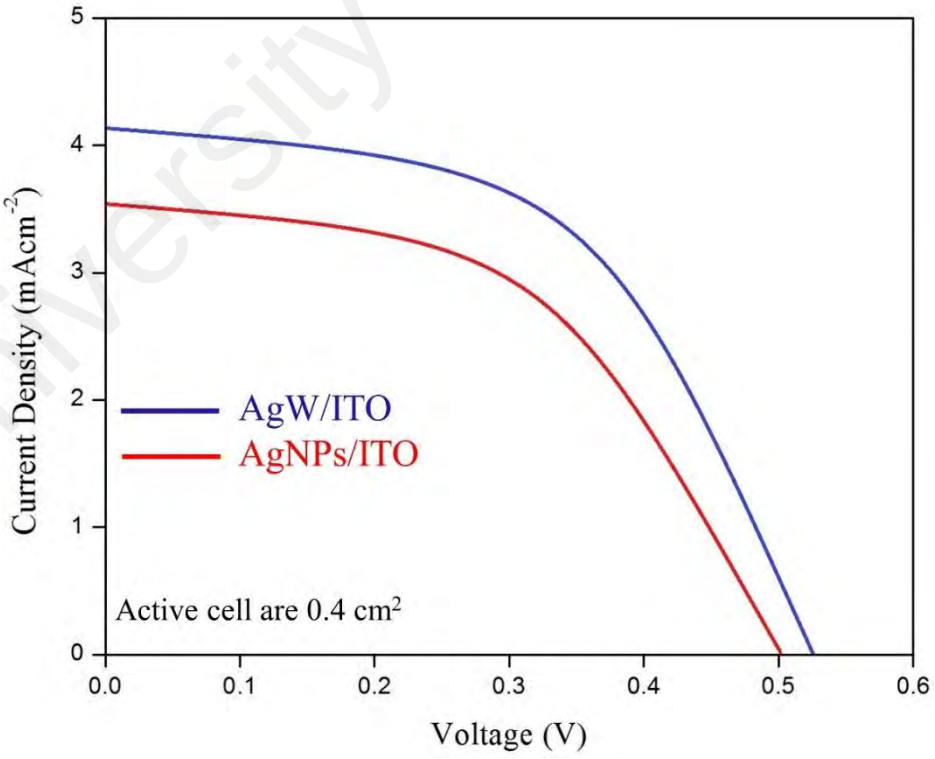

Figure 4.25: J-V characteristics of DSSCs based on AgW/ITO and AgNPs/ITO CEs.

So far, we have discussed the properties of DNA and RNA templated Ag wires on ITO and Si substrates, respectively. We have established the importance of DNA/RNA scaffolding in templating AgNPs into AgW. The significance of cleaning and removing the residual scaffold after the complete fabrication of AgW has also been elaborated. Although DNA and RNA templating methods are based on template-directed nucleation and growth mechanism, we observed that both the nucleic acids formed AgW of different heights. Moreover, the use of surfactant considerably reduced the Marangoni effect. The reduced Marangoni effect helped the complete diffusion of Ag-DNA complexes towards the scribe. An interesting observation made using the studies discussed above, is the dependence of the catalytic properties of a substrate on the morphology and dimensions of the templated AgW on it.

4.1.4 DNA Templated Au Wires

Although an enhancement in the characteristics of solar cells can be observed with the use of modified CEs based on Si wafer and ITO, however the low efficiency of the cells indicates unsuitability of the CEs. Moreover, the templated AgW formed existed in sub-micron dimensions. In the following study, DNA templated Au wires (AuWs) were fabricated on Pt sputtered ITO (Pt/ITO) substrates using 'scribing' or 'writing' method to be used as modified CE in DSSCs. Pt sputtered ITO is a conventionally used CE for DSSCs. The catalytic and conductive properties of CEs are highly dependent on size and shape of metal nanostructures on the substrate (Zeng et al. 2009). It has been established from studies mentioned above that the RNA/DNA templated fabrication of metal wires on conventionally used CE could enhance the catalytic properties of the CEs, thereby, improving the performance of the DSSCs. In this respect, the results were compared with conventionally used CE. DSSC fabricated using TiO_2 photoanode, N719 dye, I_3^-/I^- electrolyte and AuWs/Pt/ITO CE showed 36 % increase in efficiency as compared to the cells made under same parametrs but using conventional (Pt/ITO) CE. Moreover, in this

study, the effect of annealing on the size and morphology of the templated AgWs was also studied. The wires obtained after annealing of scribed Au-DNA film were formed in nanoscale dimension.

4.1.4.1 Morphological and Elecmental Analysis of the Fabricated AuWs

FESEM images of the studied samples are shown in Figure 4.26. Monodispersed and spherical AuNPs with an average size of 15.6 nm on Pt/ITO substrate can be seen in Figure 4.26(a). Negative control is shown in Figure 4.26(b) and non-DNA conjugated AuNPs were observed to be scattered all over the Pt/ITO substrate. Moreover, no formation of wire structures could be observed. Figure 4.26(c, d, f) shows the scribed Ag-DNA films subjected to annealing at different temperatures. On increasing the annealing temperature, the gap between the edges of the scribe was increased. Moreover, an increase in annealing temperature also increases the material density around the edges of the scribe. The reason could be attributed to the forced evaporation of any moisture left within the Ag-DNA complexes before annealing. Figure 4.26(d) shows the magnified image of networked AuW (annealed at 200 °C) after the removal of the DNA scaffold. Granular morphology of the fabricated AuW can be observed. The mechanism of formation of AuW around the edges is same as described for Ag/DNA studies.

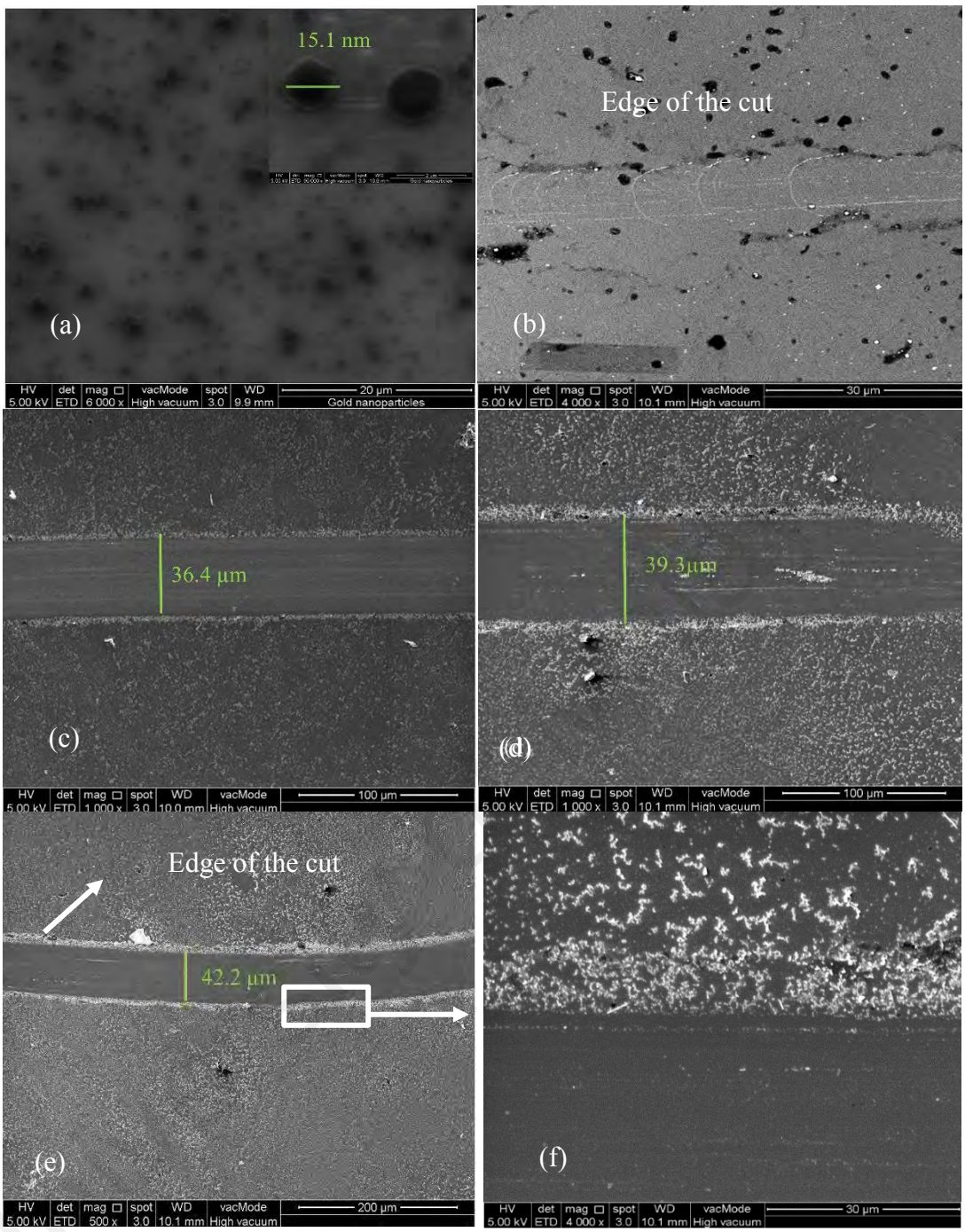

Figure 4.26: FESEM images of (a) AuNPs on Pt/ITO, (b) scribed AuNPs without binding with DNA, scribed Au-DNA films annealed at (c) 150 °C, (d) 200 °C, (e) 250 °C and (f) magnified image of AuW after cleaning.

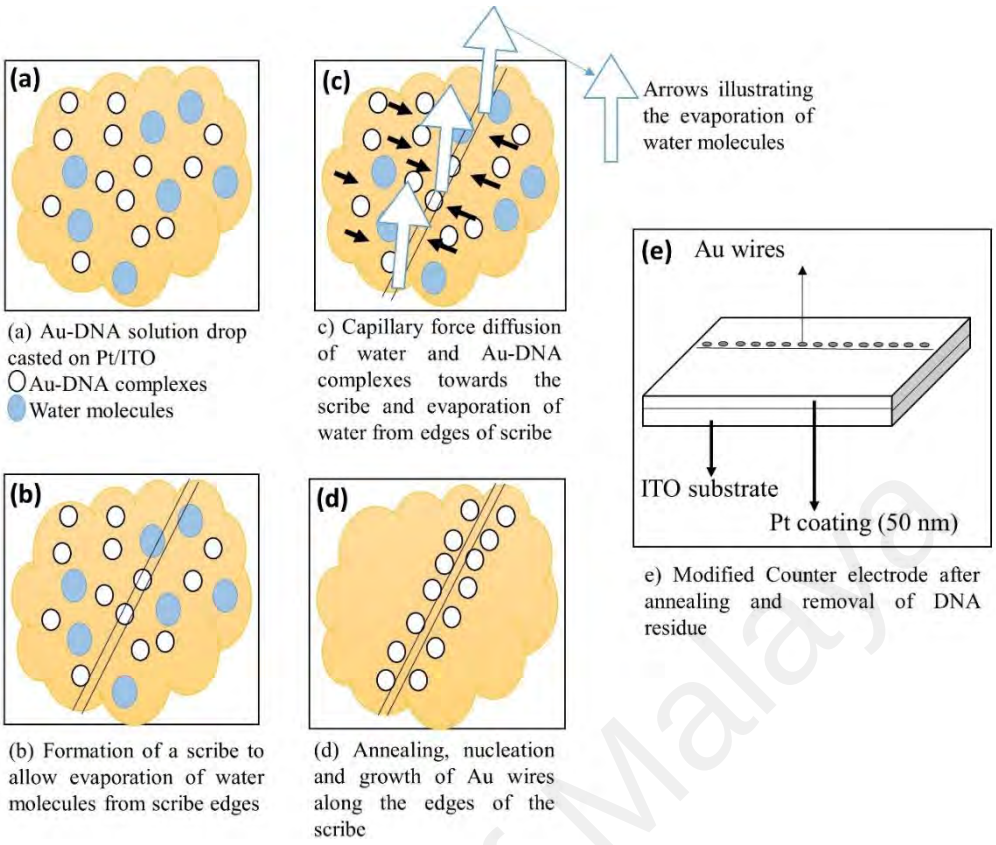

Figure 4.27: Images showing (a-d) the mechanism of aligning AuW on Pt/ITO using capillary force and (e) the structure of modified CE.

The mechanisms involved in the fabrication of AuW along the edges of the scribe and the structure of the modified CE used in this study are shown in Figure 4.27. Meanwhile, Figure 4.28 demonstrates the proposed growth mechanism of DNA templated AuW.

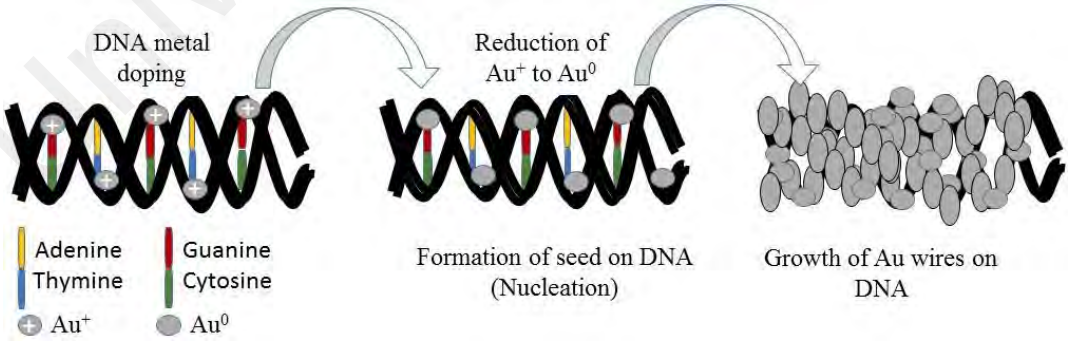

Figure 4.28: Proposed schematic illustration of growth of DNA templated AuW.

AFM image of the fabricated AuW (Figure 4.29), shows the granular morphology of the well-connected AuW with diameters ranging from 10 to 80 nm. The decrease in the height, as compared to previous studies reported in this chapter, was attributed to the positive aspects of annealing.

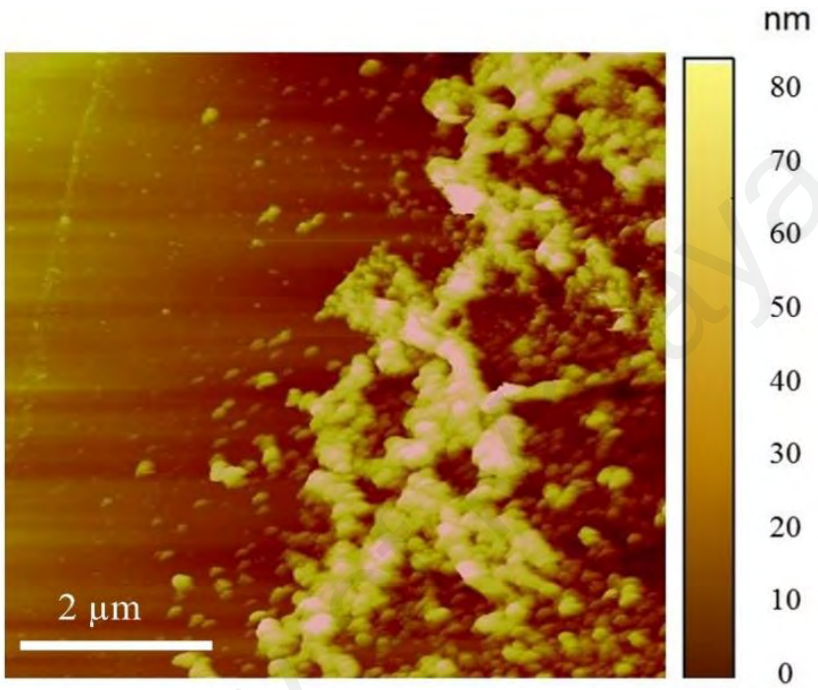

Figure 4.29: Contact mode AFM image of fabricated AuW showing diameter ranging from 40-80 nm.

EDX spectra of the AuNPs/Pt/ITO, as shown in Figure 4.30(a), exhibit strong signals characteristic to Au and Pt. The C and O present in AuNPs-DNA/Pt/ITO sample are the constituents of DNA, successfully removed after etching (Figure 4.30(c)). After the fabrication of AuW, removal of DNA scaffold is very important as DNA possess a semiconducting behavior (Periasamy et al., 2016). Moreover, it has been established from previous results that the presence of any amount of DNA left on the CE could be detrimental for its performance.

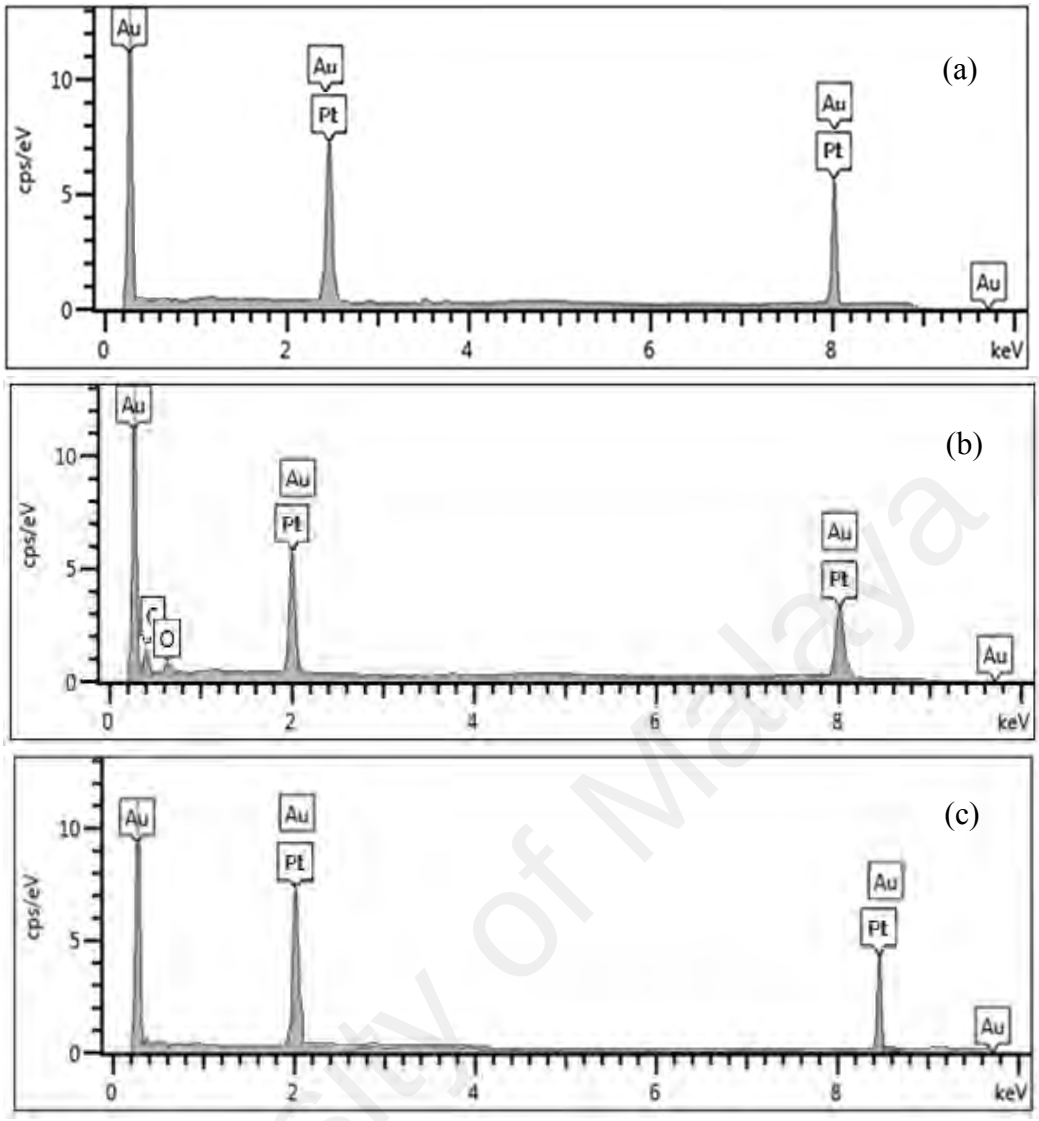

Figure 4.30: EDX graphs of (a) AuNPs/ITO, (b) Au-DNA/Pt/ITO and (c) AuNPs/Pt/ITO films showing successful removal of DNA scaffold after cleaning and formation of clean AuW on Pt/ITO substrates.

4.1.4.2 FTIR Studies on Binding of AuNPs to DNA

Interaction and binding of AuNPs with DNA was studied using FTIR spectroscopy, shown in Figure 4.31, and summarized in Table 4.4. Several spectral changes in terms of intensities and shifting was observed in DNA on binding with Au NPs. In DNA film, several plane vibrations related to DNA can be observed; asymetric-stretch of phosphate band at 1222 cm^{-1}, which is a characteristic band for B-form DNA, (A-C) at 1609 cm^{-1}, (G-T) at 1717 cm^{-1}, (T, G, A, C) at 1663 cm^{-1} and backbone (C-O) at 1051 cm^{-1} (Hackl

et al., 2005). On interaction of DNA with AuNPs, significant band changes to lower ferquency can be observed at 1609 cm^{-1}, 1663 cm^{-1} and 1717 cm^{-1}. These spectral changes are due to the formation of Au-DNA complexes.

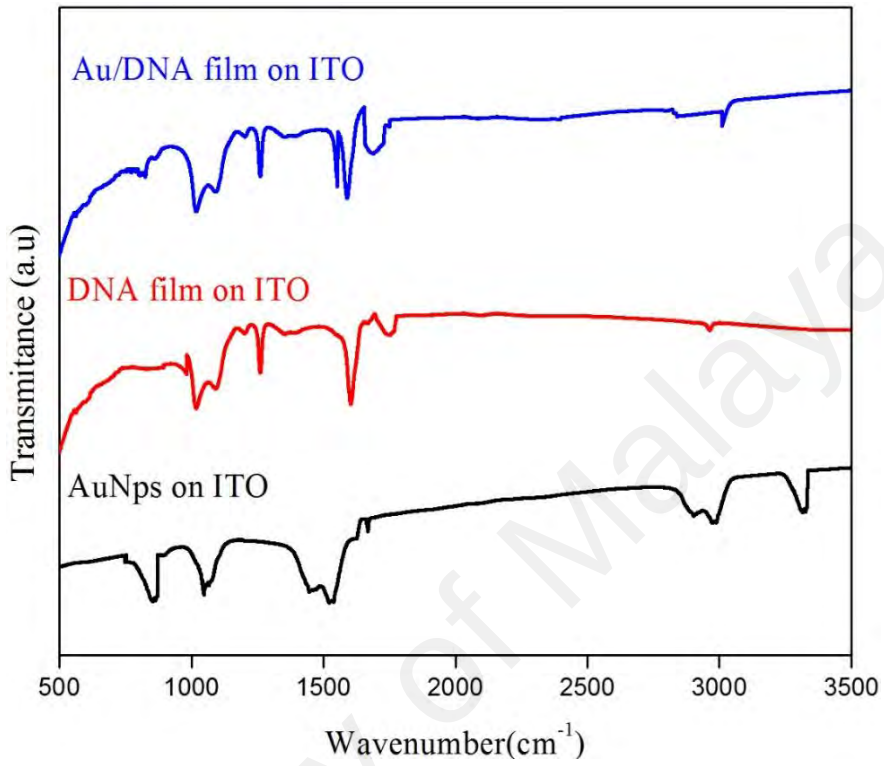

Figure 4.31: FTIR Spectra of AuNPs/ITO, DNA/ITO and Au/DNA/ITO films to study the interaction of Au with DNA and their binding.

These results suggest that DNA binds Au to its A-T and G-C base pairs. Due to the alteration in frequencies of A, T, G and C, it is suggested that on adding AuNPs to DNA, AuNPs interchelated between A and T as well as G and C nucleotides. Moreoever, no changes in intensities of assymetic and symetric stretching of phosphate groups and backbone of DNA at 1051 cm^{-1}, 1087 cm^{-1} and 1222 cm^{-1} suggests no participation of C-C and C-O as well as phosphate groups of DNA in Au-DNA binding. The backbone conformation of DNA was not changed during the binding. Bands present in AuNPs were due to C-O, N-O and O-H stretching arising mainly due to cappimg agents and water molecules.

Table 4.4: Conformal bands in DNA and shifts on interaction with Au ions to study the binding of Au with DNA.

Assignment	DNA film (cm^{-1})	Au-DNA film (cm^{-1})
Backbone (VC-O)	1051	1051
Symmetric phosphate	1087	1087
Anti-symmetric phosphate	1222	1222
Base pair(A-T)	1608	1569
Base pair (T,G,A,C)	1663	1656
Base pair (G-C)	1717	1700

4.1.4.3 Structural Studies of AuW/Pt/ITO based on XRD and XPS

In order to study the effect of annealing on AuW, DNA templated AuW was fabricated on ITO glass to ignore the peaks related to Pt in the film. The XRD spectra of AuNPs and AuW are shown in Figure 4.32.

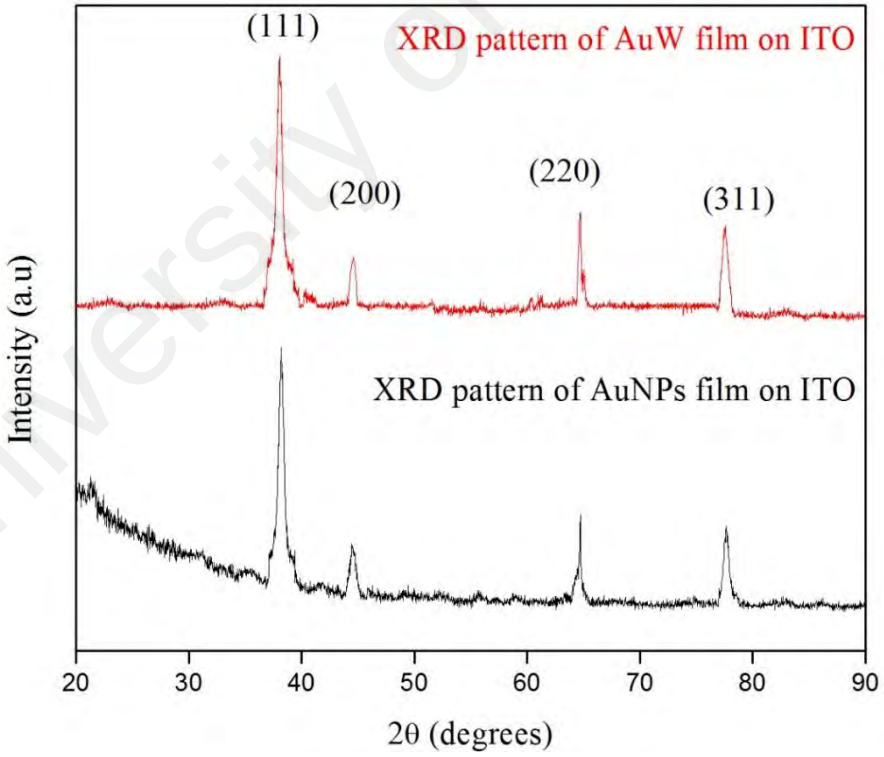

Figure 4.32: XRD patterns of AuNPs and AuW on ITO.

Characteristic diffraction peaks at 38.2, 44.5, 64.7 and 77.7° are indexed to (111), (200), (220) and (311) reflection planes, respectively, of the fcc structure of metallic Au (JCPDS No. 04-0784). The peak indexed at (111) plane, is more intense than the other peaks suggesting that the fabricated AuNPs and AuW were crystalline in nature (Suman et al., 2014). Mean crystallite sizes for AuNPs and AuW were calculated using Scherer equation (4.1) using the data from the most intense peak (111), and the crystallite sizes were estimated to be 43 and 45 nm, respectively. This indicates that the annealed-DNA templated AuW thus formed were nano-crystalline in nature. Watson et al. conducted XRD analysis on DNA templated Cu nanostructures and reported formation of microcrystalline material, in contrast to the material obtained here which is nanoscale (Watson et al., 2009).

AuW/Pt/ITO CE was subjected to XPS to analyze the valence state of AuW after their growth on the DNA template. Figure 4.33(a, b, c) shows AuW/Pt/ITO XPS wide spectrum, Pt4f narrow spectrum and Au4f narrow spectrum, respectively. The XPS wide spectrum exhibited Au4d, Au4f and Pt4f peaks along with trace levels of O1s and C1s depicting complete removal of the DNA residue. No impurity peaks were observed and the results were consistent with EDX analysis. Two sets of peaks in Pt4f and Au4f narrow scan in Figure 4.33(b, c) can be observed at (71.6, 74.9 eV) and (83.7, 87.4 eV), which are assigned to ($Pt_{7/2}$, $Pt4f_{5/2}$), and ($Au4f_{7/2}$, $Au4f_{5/2}$) of metallic Pt and Au, respectively (Dablemont et al., 2008; Kim et al., 2013; Li et al., 2015). These results indicated that no Au oxide or any other ionic form of Au was present on the CE after nucleation and removal of DNA.

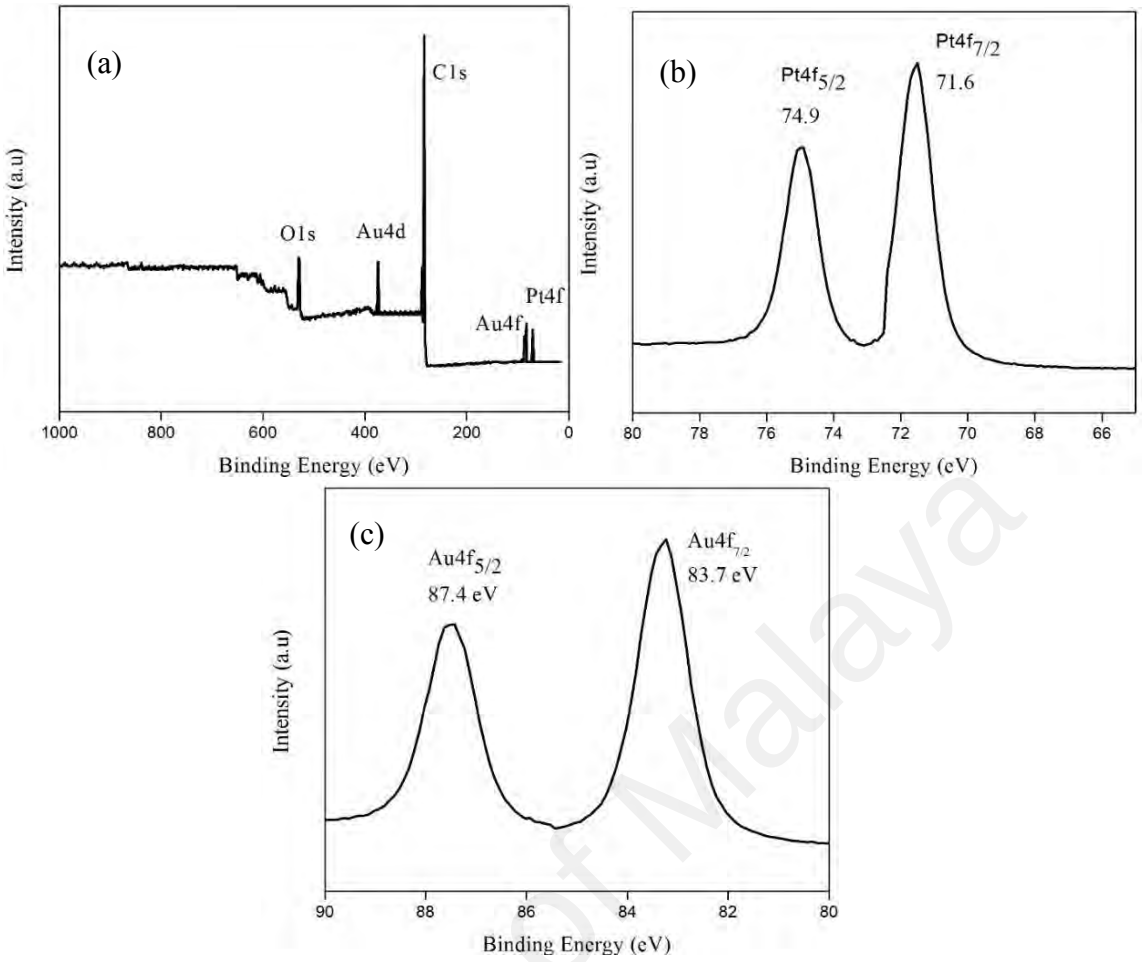

Figure 4.33: Images showing (a) XPS Survey scan spectra of AuW/Pt/ITO CE, High resolution spectra for (b) Pt and (c) Au and XRD spectra of fabricated AuW.

4.1.4.4 Electro-catalytic and J-V Characteristics of the CEs

To study the electro-catalytic activity of AuW/Pt/ITO for their use as CE in DSSCs, the CV curves were recorded in liquid electrolyte with Pt/ITO CE as reference, as shown in Figure 4.34. The shapes of the curves of the studied CEs are very similar to that of Pt/ITO CE, revealing that the AuW/Pt/ITO CE and Pt/ITO CE possess similar electro-catalytic activity. Two sets of redox peaks can be observed in the curves; redox peaks at the left were due to Reaction 1 (Equation 4.2), while redox peaks at the right were due to reduction Reaction 2 (Equation 4.3).

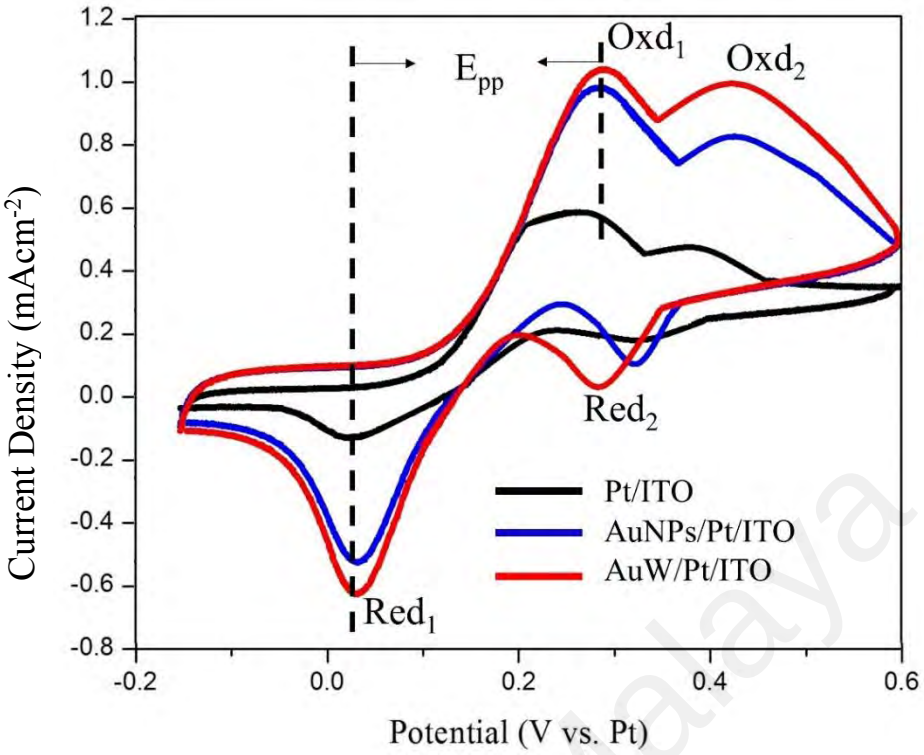

Figure 4.34: CV curves of Pt/ITO, AuNPs/Pt/ITO and AuW/Pt/ITO CEs at scan rate of 100 mVs^{-1}.

The CE catalyze the reduction of tri-iodide ions to iodide ions and the left pair of peaks (red_1) are critically important for performance of CEs (Dao et al., 2011). In this regard, peak current density is an important parameter to analyze the catalytic activity of the CE. High current at fixed voltage is indication of a stronger reaction (Veith et al., 2011). Notably, AuW/Pt/ITO CE possess maximum current density (Table 4.5). Another parameter to analyze the catalytic activity of the CEs is the peak-to-peak separation (E_{pp}). Electrochemical constant (k_s) and E_{pp} are inversely proportional to each other and therefore, smaller the E_{pp}, higher are the catalytic properties (Bolton & Kearns, 1978; Dao et al., 2011). J_{Red1} and E_{pp} values **(**Table 4.5) show that the presence of AuW on Pt/ITO CE has promotional effect on electro-catalytic activity of the CE. This could be attributed to the increase in the quantity of bonding sites which ensures rapid charge transfer, decrease in the I_3^- reduction over potential and enhancement in the reaction kinetics.

Table 4.5: Photovoltaic and Electro-catalytic parameters of DSSCs and CEs.

Sample	Solar cells characteristics				CEs	
	V_{oc} (V)	J_{sc} (mA)	FF	η (%)	J_{Red1} ($mAcm^{-2}$)	E_{pp} (V)
Pt/ITO	0.61	2.90	0.60	2.50±0.02	0.6	0.19
AuNPs/Pt/ITO	0.65	3.30	0.64	3.02±0.04	0.99	0.18
AuW/Pt/ITO	0.66	3.80	0.69	3.40±0.04	1.10	0.17

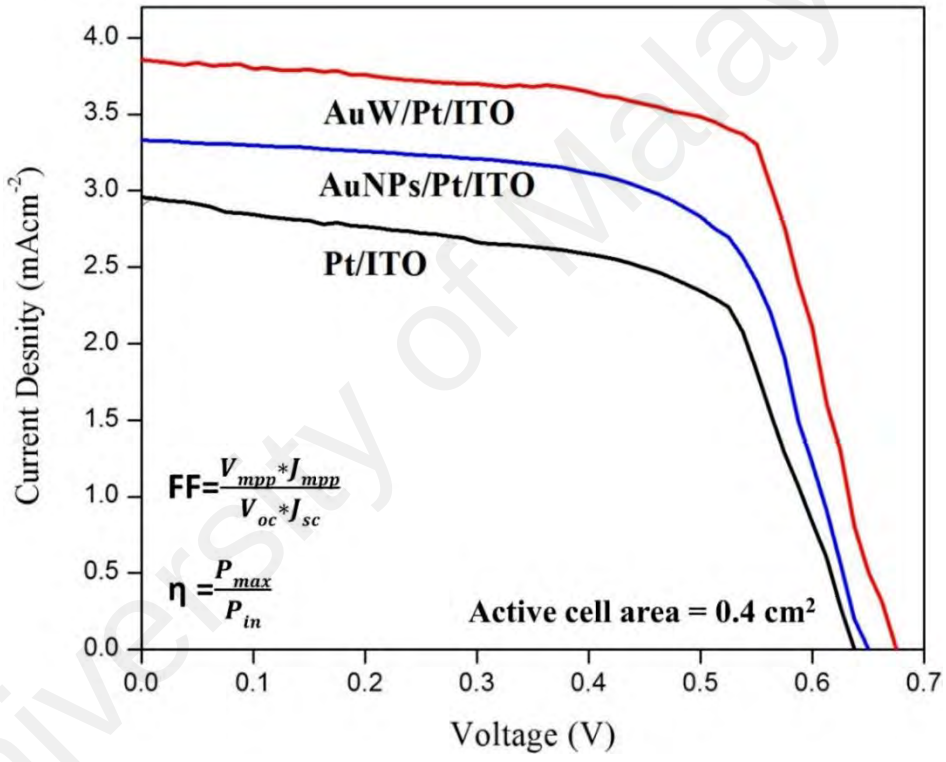

Figure 4.35: J-V curves of DSSCs with identical photoanodes and, Pt/ITO, AuNPs/Pt/ITO and AuW/PT/ITO CEs.

J-V characteristics of the DSSCs, fabricated using identical photoanodes and the modified CEs were studied to analyze the performance of solar cells, are summarized in Table 4.5. The J-V curves of the solar cells in Figure 4.35 shows that the cells fabricated using AuW/Pt/ITO CEs show the maximum efficiency and fill factor. The enhanced overall performance of AuW/Pt/ITO CE based solar cells can be attributed to higher

catalytic reduction of the iodide ions in the electrolyte and better electrochemical performance of the CEs.

4.1.5 Comparisons of the Results based on RNA/DNA Metal Templating on Si, ITO and Pt/ITO Substrates

Based on the studies discussed above, we noticed several physical and chemical mechanisms involved in fabrication of nucleic acid templating metal wires in sub-micron to nanometer range. We also studied the limitations of the capillary force assisted fabrication of RNA/DNA metal templating in terms of Marangoni effect and templated wire heights. The limitations were overcome by using a surfactant and annealing the studied samples. In this section, we have discussed the comparative results based on addition of surfactant, annealing and the findings based on scaffolding material (DNA or RNA). Moreover, the performance of different CEs has also been discussed and summarized.

So far it has been established that the self-assembly properties of DNA and RNA, arrange the metal NPs in connected network of metal wires, when dragged towards the scribed region due to capillary force action, or coffee-ring effect. As explained earlier, DNA and RNA, both tends to conjugate metal NPs into its structure due to specific metallic bonding. When a scribe is formed on the film, differential evaporation rates induce capillary force action causing water to evaporate from the edge of the scribe and the loss of water is replenished by the water in the bulk. Due to this energy, metal-nucleic acid complexes are dragged towards the scribe. Environmental heat provides enough energy for natural evaporation of water. However, the energy is not enough to externally remove the complexes hence deposition occurs at the edges of the scribe. Moreover, DNA and RNA act as a template to form active sites for nucleation of the metal wires. Thereby, it is necessary to understand the mechanisms of capillary force action resulting in the

coffee-ring effect and the Marangoni flow in order to understand the novel method described in this study. None of the DNA templating methods reported earlier, involve the use of a 'scribe' induced capillary force action to arrange the wires along the edges of the scribe. Such an arrangement is very important for their application in micro and nanoelectronics.

4.1.5.1 Morphological Comparisons

Morphological images obtained for all fabricated metal wires on various substrates depict wire like granular structure with almost completely continuous morphology. The morphologies of the metal wires observed in this study were notably different from the previously reported DNA templated Ag wires as well as other metal-nucleic acid templated structures (Deng & Mao, 2003; Ongaro et al., 2005; Pruneanu et al., 2008; Richter et al., 2000). Sparse distribution of nanoclusters could be observed along the template and the coatings are highly irregular and non-continuous. For example, Braun et al. observed 'beads on a string' morphology of DNA templated silver wires (Braun et al., 1998) while Richter et al. (2000) observed a structural transition from separated clusters to quasi-continuous metal coating of non-continuous and irregular Pd wires (Richter et al., 2000).

In our study, it was observed from the FESEM and AFM results that DNA/RNA played an important role in templating continuous wire-like structures. The self-assembly of DNA/RNA coupled with the coffee-ring effect significantly influenced the templating process, overcoming the short comings of other DNA templated studies. However, the influence of Marangoni flow affected the complete diffusion of the metal-nucleic acid towards the edges of the scribe, which was reversed by addition of a surfactant.

4.1.5.2 Effect of SDS Surfactant Addition

During evaporation of a liquid, there are two main competing evaporation driven phenomenon that takes place, Marangoni flow and the coffee-ring effect (Seo et al. 2017). Marangoni flow suppress the coffee-ring effect and vice-versa. Coffee- ring effect was first reported by Deegan et al. (1997) based on his observations on the drying of spilled drop of coffee (Deegan et al., 1997). Drying droplet of coffee on any solid surface forms dense deposits along the perimeter of the drop in the form of rings. Initially the dense particles in coffee is dispersed entirely over the drop, but with drying they concentrate to a tiny fraction. Any drying drop containing dispersed solid particles form such ring deposits influencing processes like washing, coating and printing. Coffee-ring effect is caused by non-uniform evaporation rate in radial direction. These ring deposits forms the base to "write" metal wire fine patterns on a solid surface in our studies. The coffee-ring effect is shown in Figure 4.36 **(**Deegan et al., 1997).

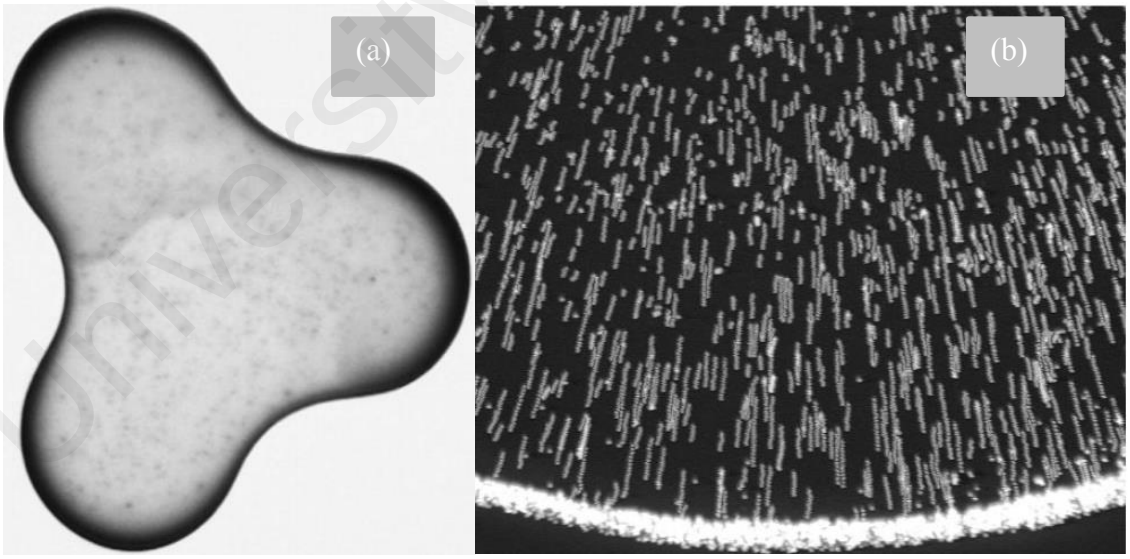

Figure 4.36: Images showing (a) a 2 cm diameter dried drop of coffee demonstrating high material density towards the end of the drop due to evaporation and (b) indication of motion of solid particles towards the high curvature (images taken from (Deegan et al., 1997)).

Marangoni effect, also known as Gibbs Marangoni effect, is a mass transfer that occurs due to surface tension gradient along an interface between two fluids. A liquid with low surface tension pulls less strongly on the surrounded liquid as compared to the liquid with high surface tension. Due to this surface tension gradient, the liquid with high surface tension naturally flows away from low surface tension regions. For example, if water is mixed with alcohol, a region with lower concentration of alcohol will have high surface tension and a region with a higher concentration of alcohol will have lower surface tension. High surface tension region will pull on the surrounding fluid strongly, thereby, causing the flow of the liquid away from the regions of low surface tension.

It was found in our study that the addition of surfactant in appropriate amounts reduced the Marangoni flow of the metal-DNA/RNA complexes resisting their deposition anywhere else than the scribe. This was due to the lowering of the surface tension and cohesive forces within the droplet (Miniewicz et al., 2016; Ogino et al., 1990).

4.1.5.3 Variations in Heights, Crystallite Sizes and the Effect of Annealing

Table 4.6 shows the mean crystallite sizes and heights of fabricated metal wires and the precursor metal NPs. The mean crystallite sizes of the fabricated metal wires for AgW/Si, AgW/ITO and AuW/Pt/ITO show a transition from microcrystalline to submicron-crystalline to nano-crystalline structure, respectively. These transitions are dependent on the annealing of the AuW on Pt/ITO substrate leading to forming the structures in nanocrystalline scale and the scaffold structure.

A decrease in height of the wire can be observed for AgW/Si, AgW/ITO and AuW/Pt/ITO samples. It is notable, that the heights of the fabricated wires depend upon the scaffold structure. Both DNA and RNA reduce the AgNPs on their surface where the nucleation and growth of the wires start. The structure difference in DNA and RNA plays an important role here in determining the growth of the wires and their size. Moreover,

the reduction in heights of the AuW/Pt/ITO can be observed as compared to AgW/Si and AgW/ITO which is attributed to the annealing.

Table 4.6: Summary of the metal NPs sizes, heights of the fabricated wires, mean crystallite sizes of NPs and mean crystallite sizes of fabricated wires calculated from FESEM, AFM and XRD results, respectively.

Sample	Average NP (seed) size (nm)	Maximum height of the wire (nm)	Mean crystallite size of the NPs (nm)	Mean crystallite size of wires (nm)
RNA templated AgW/Si	10	250	40	150
DNA templated AgW/ITO	10	110	40	100
DNA templated AuW/Pt/ITO	16	90	43	45

4.1.5.4 Performance Comparisons of the CEs and their Respective DSSCs

Table 4.7 shows the summary of the results based on CV and J-V characteristics of CEs and DSSCs, respectively. It has been well established up till now that presence of DNA/RNA templated metal wires significantly enhanced the catalytic properties of the substrates and therefore, enhanced the working of the DSSCs. However, the performance of the CE also depends on the type of substrate used (Si, ITO or Pt/ITO). Even though AgW/ITO CE possessed lower catalytic activity (J_{Red1}=0.39) as compared to that of AgW/Si (J_{Red1}=0.60), the efficiency obtained for AgW/ITO based DSSC is higher. Among all the studied CEs, AuW/Pt/ITO generated maximum value of J_{red1} and the DSSC based on this CE showed highest efficiency (3.40 %). The reason was attributed to the synergistic effect of Pt and AuW on ITO which enhances the properties of the CE material.

Table 4.7: Summary of the results based on CV and J-V characteristics of studied metal wires.

Sample	J_{Red1} ($mAcm^{-2}$)	V_{oc} (V)	J_{sc} (mA)	η (%)
RNA templated AgW/Si	0.60	0.49	3.5	0.96±0.03
DNA templated AgW/ITO	0.39	0.52	4.10	1.29±0.02
DNA templated AuW/Pt/ITO	1.10	0.66	3.80	3.40±0.04

4.1.5.5 The Replacement of Enzymatic Etching with Simple Hydro Cleaning

Fabricating sub-micron to nanosize metal wires using DNA, DNA residue was removed using enzymatic etching after the templating process was completed. It is very important to remove any amounts of DNA left on the substrate. Presence of small amount of residue could be detrimental for their use in electronic circuits and solar cells. Using RNA makes the process of fabricating micron to nano scaled electrode gaps more economical and facile as the step of scaffold removal becomes easy. The phosphate groups in sugar phosphate backbone of both RNA and DNA have a partial negative charge making them soluble in water. However, the ribose sugar in RNA has an extra –OH group, as shown in Figure 4.37, making it more soluble in water.

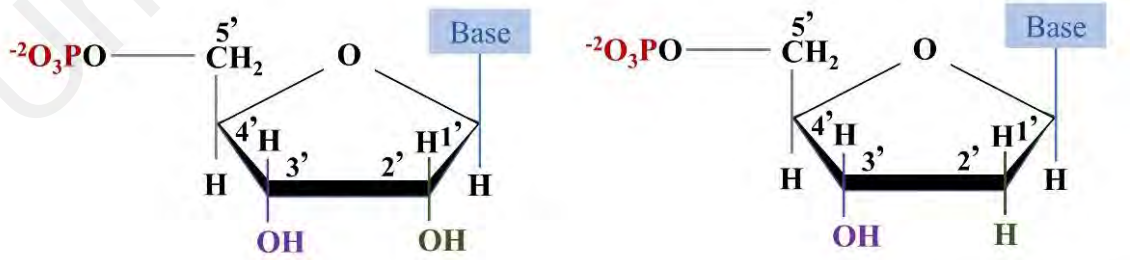

Ribonucleotides Deoxyribonucleotides

Figure 4.37: Diagram illustrating the presence of an extra OH bond in RNA making it more soluble in water.

Moreover, exposed bases present in RNA contain polar bonds. With increase in the number of polar bonds, the solubility in water also increases. Due to high solubility of RNA in water, samples were washed 3 times using DI water which resulted in complete removal of the RNA residue and clean electrode gaps were obtained.

CHAPTER 5: RESULTS AND DISCUSSION II: DEVELOPMENT OF PHOTOANODE

In this chapter, the research has been focused on increasing the efficiency of the DSSCs by developing photoanodes compatible with our modified CEs. Deposition methods such as AACVD and EPD were used to fabricate modified TiO_2 photoanodes. Studies were conducted on their morphological, optical and structural properties of the photoanodes and the effect of these properties on the efficiency of DSSCs was analyzed. Moreover, the performance of the DSSCs was also studied using modified photoanodes and modified CEs using J-V characteristics of the fabricated DSSCs. Therefore, the work presented in this chapter is based on the studies on the development of photoanodes for the DSSCs.

The basic working principle of DSSCs involves the generation of photo excited electrons by the dye molecules adsorbed on a semiconductor photoanode. Generated electrons are transferred to the CB of the semiconductor from where it is transported to the outer circuit. Meanwhile, the electron deficiency in dye molecules is regenerated by a redox electrolyte to avoid the back transfer of the photo generated electron (recombination) (Lee et al., 2008). Henceforth, photoanode is one of the most important components of DSSCs that highly influences the performance of the DSSC. Photoanode must allow fast electron injection and possess optimum porosity to allow complete adsorption of dye and electrolyte (Keshavarzi et al., 2015; Lu et al., 2012; Song et al., 2016). TiO_2 is an abundantly used semiconductor material for photoanode owing to its high availability, nontoxicity, high stability and low cost. However, weak absorption of TiO_2 in visible region of solar spectrum and high recombination rate hinders the performance of TiO_2 as a photoanode material (Qu et al., 2013). To enhance the performance of TiO_2 photoanode, surface modifications needs to be done by doping TiO_2

to extend the optical absorption of the semiconductor, decrease the charge recombination centers and improve charge carrier separation.

5.1 AACVD of Mg Doped TiO_2 Films

AACVD not only offers simple setup and requires low maintenance and costs but also deposit homogenous films. Despite having advantages over other deposition techniques, AACVD hasn't been studied extensively due to difficulties in controlling film porosity. In this section, we have morphologically and structurally analyzed TiO_2 and Mg doped TiO_2 films deposited using AACVD. The limitations of TiO_2 and the AACVD method have been addressed and solved using Mg as a dopant.

5.1.1 Morphological and Elemental Analysis

Surface morphology of the fabricated films was studied using FESEM and the images are shown in Figure 5.1. The films exhibited rough surfaces with crystalline nature. The morphology of the films exerts profound effect on the performance of the photoanode and hence the performance of the DSSC. High crystallinity and high porosity of films have positive effects on the overall efficiency of the solar cell (Lu et al., 1997). It can be observed that the films appear more porous and the pore network appears more interconnected with increase in doping concentration attributed to the addition of dopant into the anatase lattice of TiO_2.

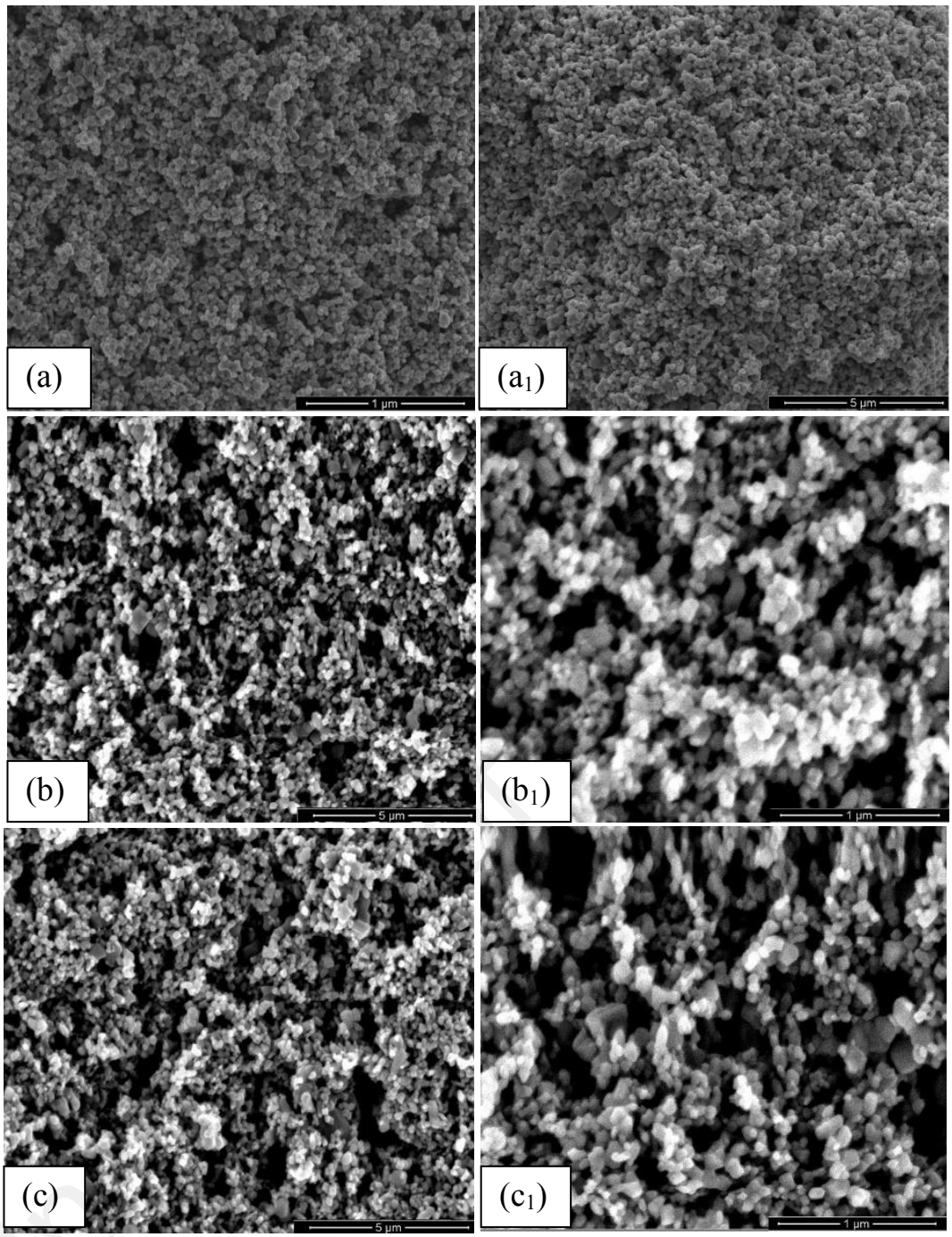

Figure 5.1: Low resolution (a) (b) (c), and high resolution (a_1), (b_1), (c_1) FESEM images showing morphology of TiO_2 film, 1 mol% Mg doped TiO_2 thin film and 2 mol% Mg doped TiO_2 thin film, respectively.

EDX analysis was performed to determine the concentration of elements and the contaminants in the films, shown in Figure 5.2 and summarized in Table 5.1. It can be observed that the Mg wt% increases with an increase in doping concentration, thereby, decreasing the concentration of Ti in the TiO_2 lattice. This can be attributed to the replacement of Ti cation by Mg^{2+} due to successful doping at the atomic level.

Figure 5.2: EDX spectra of (a) undoped TiO_2 film, (b) 1 mole% Mg doped TiO_2 film and (c) 2 mol% Mg doped TiO_2 film.

Table 5.1: Summary of doping concentrations of films estimated from EDX data and crystallite sizes calculated using (101) peak of XRD data.

Samples	Concentration (weight %)			Crystallite size (nm)
	Ti	O	Mg	
Undoped TiO_2	55.6	45.4	0.00	19
1 mol% Mg doped TiO_2	55.4	45.4	0.15	17
2 mol% Mg doped TiO_2	55.3	45.0	0.21	16

No significant change in concentration of O can be observed. This implies that no additional oxides were formed with Mg. Moreover, it can be assumed that Mg cations located at Ti^{4+} sites in TiO_2 lattice during doping. No other impurities were observed in the EDX spectra.

5.1.2 Crystal Phase and Crystallite Size Analysis

XRD pattern for all the fabricated films exhibited peaks that are consistent with anatase phase reflections (JCPDS No. 78-2486) (Stoyanova et al., 2013), as shown in Figure 5.3.

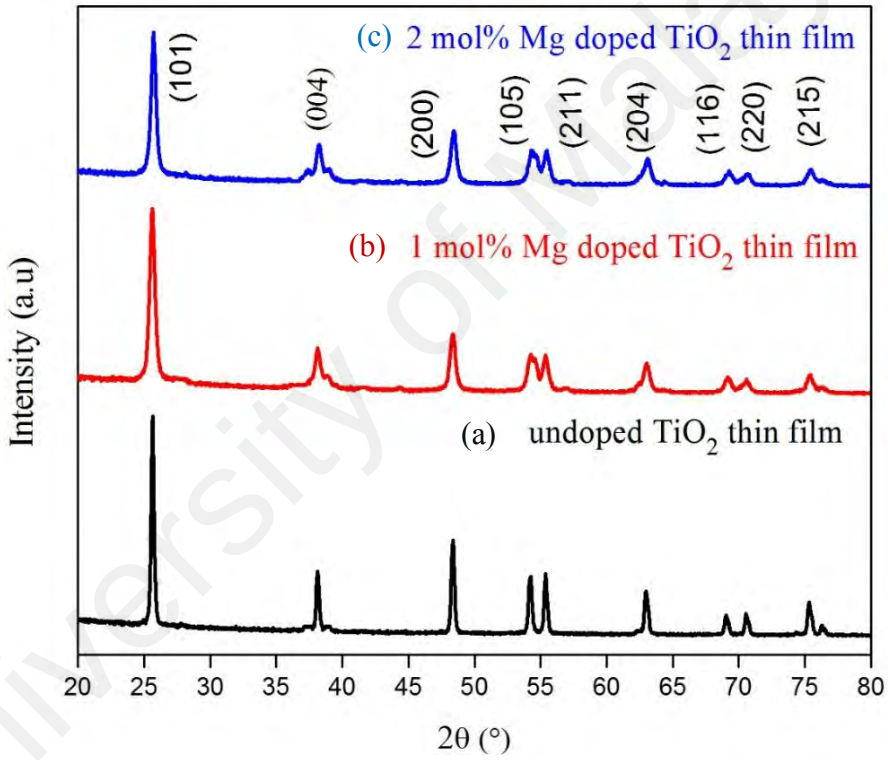

Figure 5.3: XRD patterns of (a) undoped TiO_2 film, (b) 1 mol% Mg doped TiO_2 film and (c) 2 mol% Mg doped TiO_2 film.

Undoped and doped films possess crystalline nature and pure tetragonal anatase phase with trigonal planar O^{-3} and octahedral Ti^{-6} coordination geometry (Dubey & Singh, 2017). No additional peaks of impurities, phases or oxides were observed with addition of the dopant. Anatase phase of TiO_2 is usually formed at lower annealing temperatures as compared to rutile phase. During the polymerization process of TiO_6 octahedral unit,

the dominant phase of TiO_2 is determined by its faster growth. Therefore, anatase is formed instead of rutile as initial crystalline phase of TiO_2 due to its less constrained molecular construction (Satoh et al., 2013). Moreover, anatase phase possess lower surface free energy favoring fast recrystallization of anatase polymorph (H. Li et al., 2015).

Upon doping, a reduction in intensity of the diffraction peaks can be noticed and with an increase in the concentration of Mg dopant, the intensity is further reduced. This indicates successful and uniform Mg doping into the lattice of TiO_2. Due to the similarity in ionic radii of Mg dopant and host Ti ions, Mg substitutes Ti from its lattice site via substitutional doping. Moreover, not all dopant ions enter the lattice of TiO_2 and some might remain on the surface creating grain boundaries. This affects the crystal growth of the lattice which cause a reduction in crystallite size, with increase in doping concentration. The crystallite sizes for undoped, 1 mol% Mg doped and 2 mol% Mg doped TiO_2 were calculated to be 19, 17 and 16 nm, respectively. The crystallite size was calculated using Scherer equation (Equation 4.1) on most prominent diffraction peak (101) and the data is summarized in Table 5.1. Although, a slight decrease in crystallite size was observed upon increasing doping concentration, a further increase in dopant amount could suppress crystal growth and increase grain boundaries which could be detrimental for its performance as a photoanode material. Henceforth, increasing doping concentration beyond a moderate level is not feasible.

5.1.3 Raman Analysis

To further probe the crystallinity of the films, Raman spectroscopy was performed in range 100 to 900 cm^{-1} and the results are shown in Figure 5.4. The peaks at 143, 195, 398, 512 and 632 cm^{-1} corresponds to the anatase phase (Lim et al., 2014). No peaks for rutile phase and Mg could be observed. The reason could be attributed to lower concentration

of Mg, its inclusion as a dopant in the lattice and its weak Raman scattering power. Absence of Mg oxide peaks indicated that no separate crystalline oxides of Mg were formed agreeing well with the XRD results. A reduction in the intensity of peaks of Raman spectra were observed indicating the interaction between TiO_2 and Mg affecting the Raman resonance of TiO_2. From combined results of EDX, XRD and Raman, it can be concluded that Mg was successfully doped into the TiO_2 matrix.

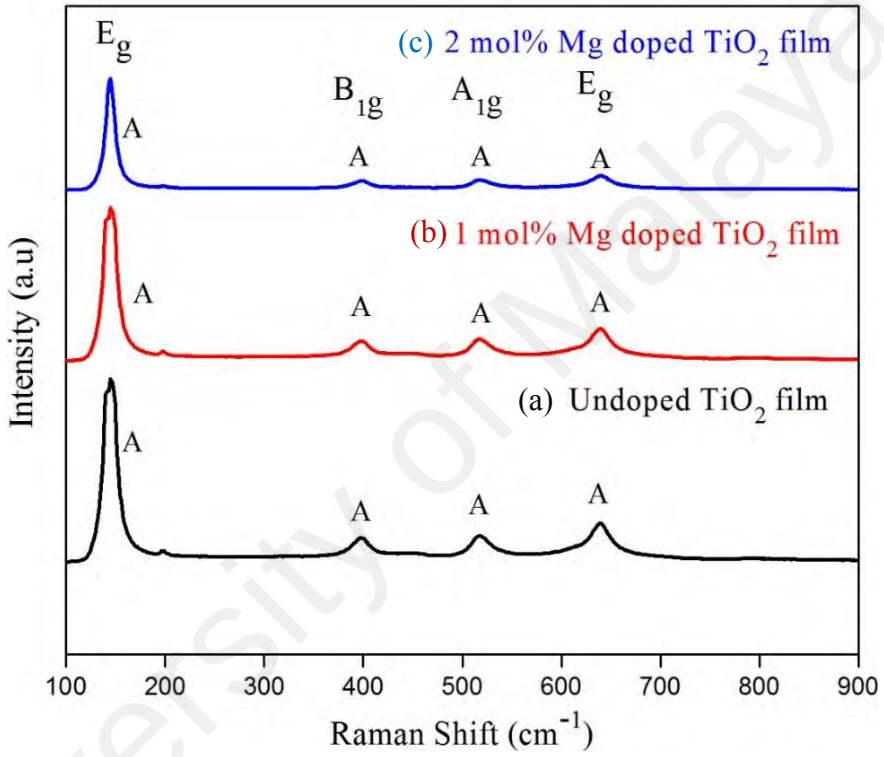

Figure 5.4: Raman spectra of (a) undoped TiO_2 film, (b) 1 mol% Mg doped TiO_2 film and (c) 2 mol% Mg doped TiO_2 film.

5.1.4 Optical Properties and Band Gap Estimation of the Films

The optical properties of films were studied using UV-vis spectrophotometry and the graph is shown in Figure 5.5. It can be observed that with increase in concentration of Mg dopant, the absorption gradually shifted towards the visible region. Usually, the absorption peaks in semiconductors correspond to the maximum absorption due to the excitation of electron from VB to the CB of the semiconductor. VB in TiO_2 comprises of

O 2p states and CB comprises of Ti 3d states. Absorption for undoped TiO_2 arises due to electronic transition from O 2p of VB to Ti 3d of CB. Shift of absorption in doped samples can be explained due to the formation of another state within TiO_2 lattice due to doping which leads to the lowering of band gap. Shift in peaks of doped samples arises due to charge transfer at the interface from O 2p VB to Mg (II) state attached to TiO_2 as proposed in Figure 5.6.

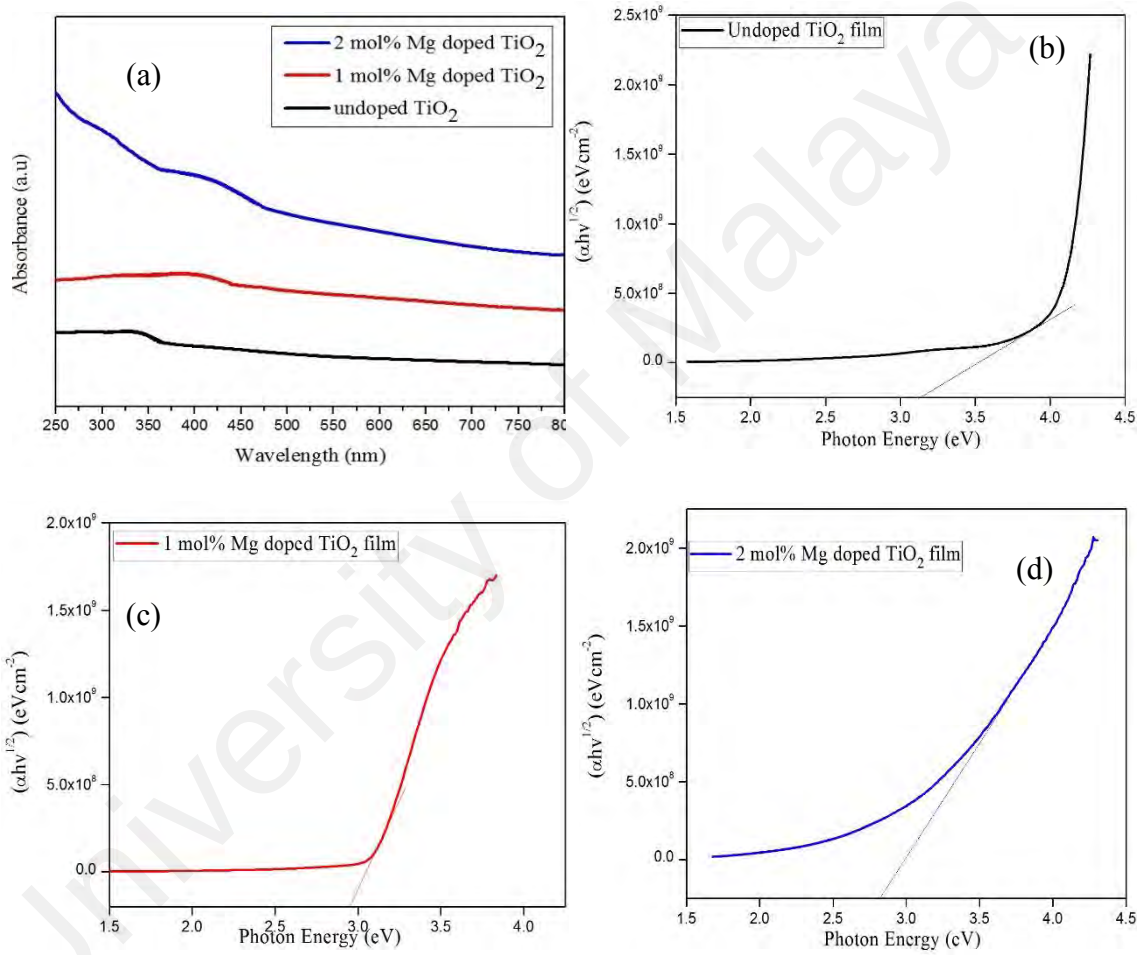

Figure 5.5: Images showing (a) UV-vis spectra of undoped, 1 mol% and 2 mol% Mg doped TiO_2, Tauc's plot and band gap estimation of (b) undoped TiO_2 film, (c) 1 mol% Mg doped TiO_2 film and (d) 2 mol% Mg doped TiO_2 film.

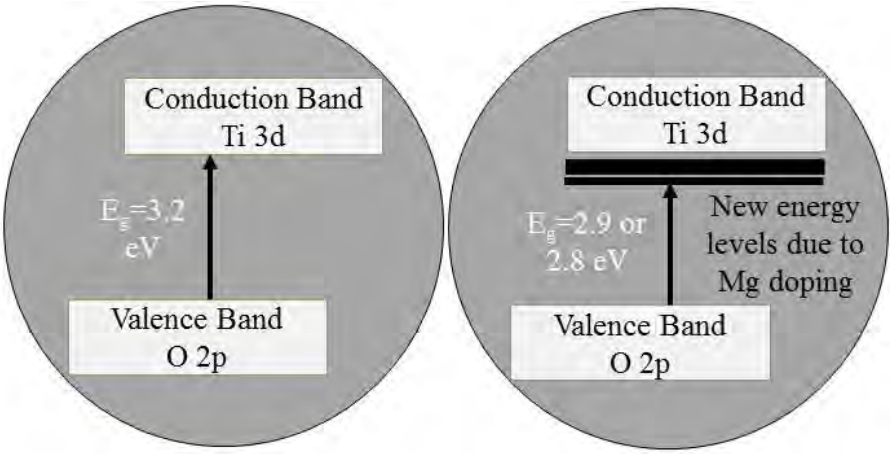

Figure 5.6: Schematic illustration of band gap narrowing due to Mg doping.

Tauc's formula, given below, was used to estimate the band gap of the films from UV-vis spectra;

$$(\alpha hv) = A(hv - E_g)^{\gamma} \tag{5.1}$$

where *α, hv, E_g* and *A* are the linear absorption coefficient, photon energy, band gap energy and proportionality constant, respectively and γ determines the characteristics of transition in a semiconductor. A value *γ*=1/2 is assigned for direct bandgap and *γ*=2 is assigned for indirect band gap.

Values of bandgap for undoped and doped films were obtained by extrapolation of the linear region in the plots of $(\alpha hv)^{1/2}$ to its intersection with energy axis (*E/eV*) (Jiménez-García et al., 2015), and the plots are shown in Figure 5.5 (b, c, d). The band gap for undoped TiO_2 was estimated to be 3.2 eV which is in good agreement with the reported value in literature (Jia et al., 2011). Upon doping TiO_2 with 1 mol% and 2 mol% Mg, the band gap is reduced to 2.9 and 2.8 eV, respectively. These results indicate an increase in photo absorption of the films due to the Mg doping. Enhanced photo absorption of the photoanode significantly enhances the performance of the DSSCs (Guo et al., 2013).

5.1.5 BET Surface Area and Pore Size Analysis

Nitrogen (N_2) adsorption-desorption isotherms of the films, shown in Figure 5.7, exhibit type IV curves for mesoporous structure (Bahramian, 2013; Reda et al., 2017).

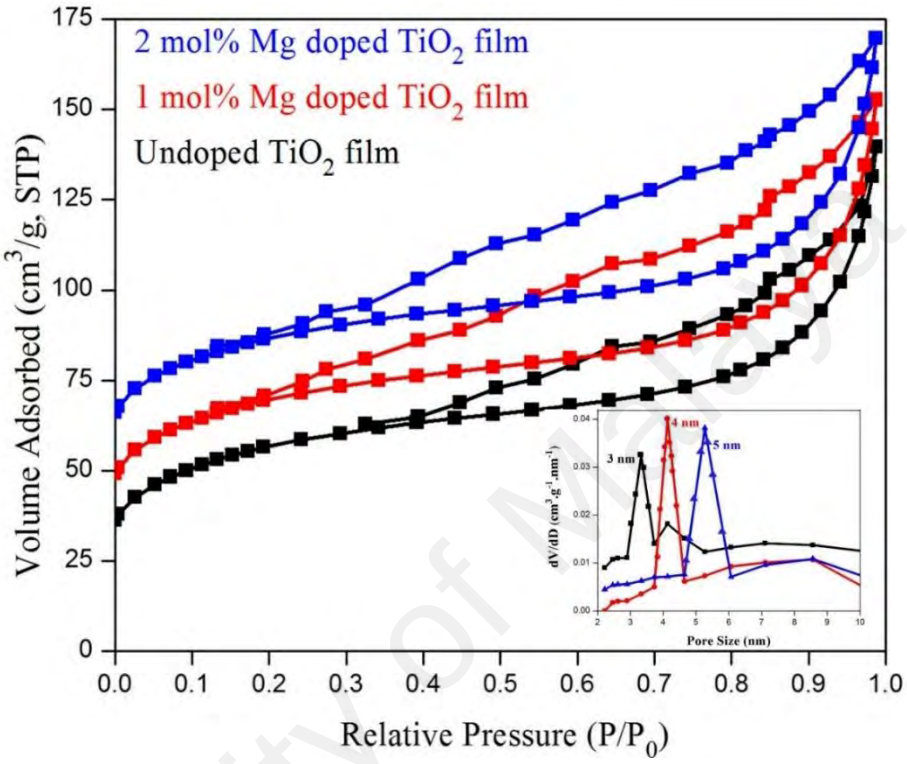

Figure 5.7: Nitrogen adsorption-desorption isotherms and inset pore size distribution of undoped, 1 mol% Mg doped and 2 mol% Mg doped TiO_2 films.

The BET surface area and average pore diameter of undoped, 1 mol% Mg doped and 2 mol% Mg doped TiO_2 films were measured to be 69.2 m^2g^{-1} and 3 nm, 67.5 m^2g^{-1} and 4 nm, 66.1 m^2g^{-1} and 5 nm, respectively (Table 5.2). Figure 5.7 (inset) shows the pore size distribution of the films from desorption curves. It can be observed that Mg doping enhanced the pore size of the films which without significantly decreasing the surface area of the films, is beneficial to enhance the J_{sc}. Larger pore size renders two main advantages to the films; it allows the dye molecules and the electrolyte to completely fill the porous films (Maleki et al., 2017; W. Song et al., 2016; Weisspfennig et al., 2014) and results in higher lifetime of generated electrons (Wang et al., 2013). Moreover, small

pore size inhibits the diffusion of dye and electrolyte, increasing the resistance at TiO_2/dye/electrolyte interface. This leads to lowering of the photocurrent. However, significantly large pore diameter could result in decrease in surface area which could limit the adsorption of dye.

Table 5.2: The average surface area and pore volume of undoped TiO_2, 1 mol% Mg doped TiO_2 and 2 mol % Mg doped TiO_2 films.

Film	Surface area (m^2g^{-1})	Average pore diameter (nm)
Undoped TiO_2	69.2	3
1 mol% Mg doped TiO_2	67.5	4
2 mol% Mg doped TiO_2	66.1	5

5.1.6 J-V Characteristics of the DSSCs

J-V curves of the fabricated DSSCs (Figure 5.8) with different photoanodes are shown in Figure 5.9 and the results are summarized in Table 5.3. From J-V curves, various photovoltaic characteristics of the DSSCs such as V_{oc}, J_{sc}, FF and η using the following equation;

$$\eta = \frac{V_{oc}J_{sc}FF}{P_{in}} \tag{5.2}$$

where, η is the efficiency of the solar cell, V_{oc} is the open circuit voltage, J_{sc} is short circuit current and FF is the fill factor.

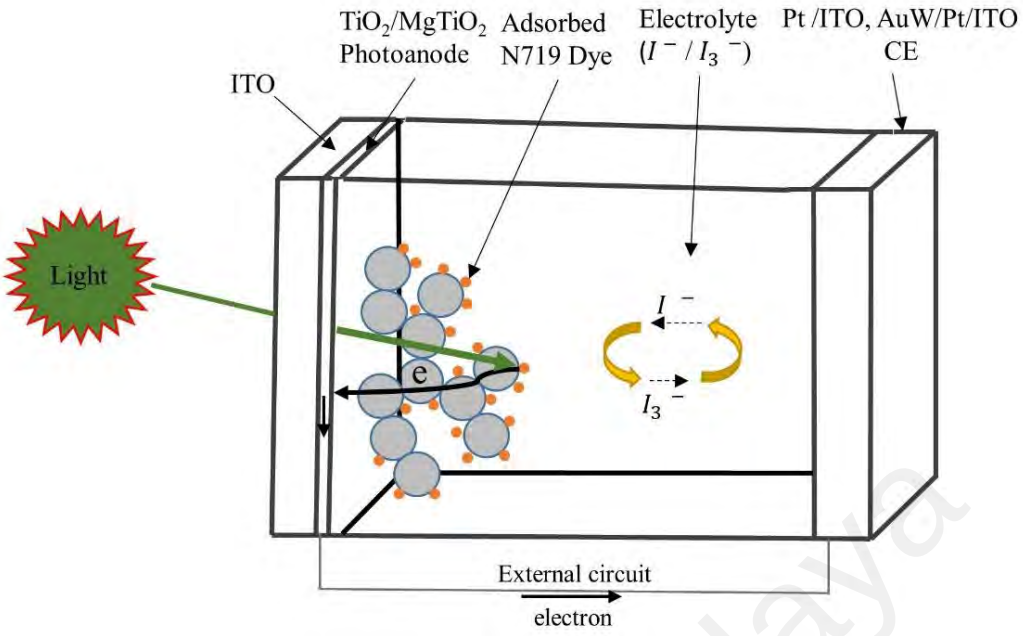

Figure 5.8: Schematic diagram of the fabricated DSSC.

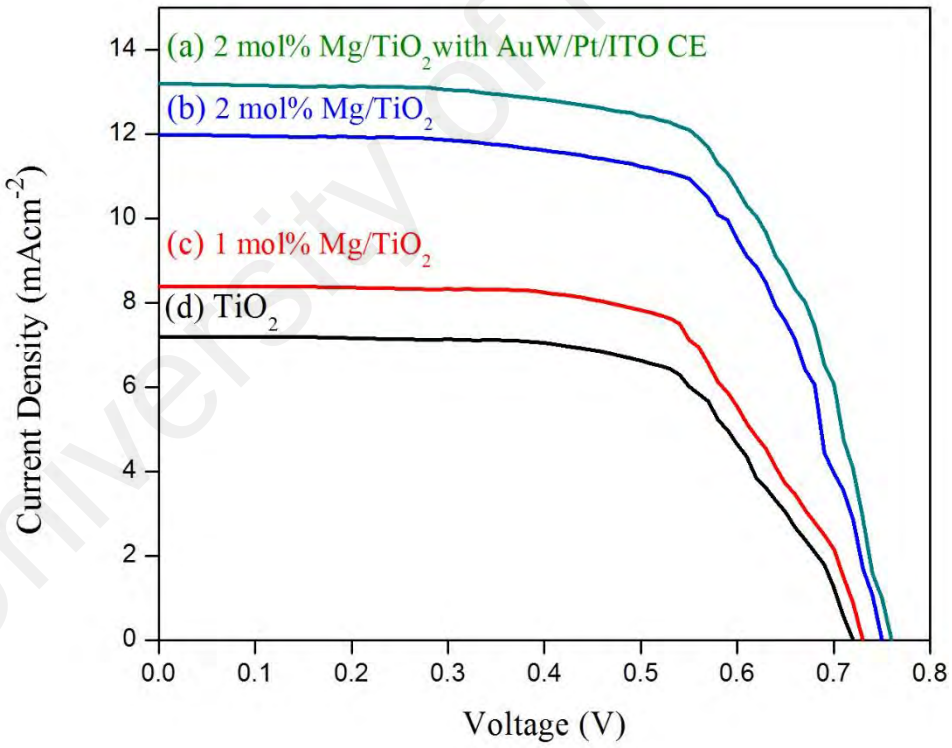

Figure 5.9: J-V characteristics of DSSCs based on (a) undoped TiO_2, (b) 1 mol % Mg doped TiO_2, (c) 2 mol% Mg doped TiO_2 photoanodes and (d) 2 mol% Mg doped TiO_2 photoanode with AuW/Pt/ITO CE.

Table 5.3: Summary of J-V characteristics of undoped and doped TiO_2 based DSSCs.

DSSC	V_{oc} (V)	J_{sc} (mA)	FF	η (%)
Undoped TiO_2 based DSSC	0.72	7.19	0.65	3.36±0.01
1 mol% Mg doped TiO_2 based DSSC	0.73	8.39	0.66	4.05±0.03
2 mol% Mg doped TiO_2 based DSSC	0.74	11.99	0.67	6.10±0.02
2 mol% Mg doped TiO_2 based DSSC with AuW/Pt/ITO CE	0.75	13.10	0.68	6.68±0.04

An increase in V_{oc} and J_{sc} can be observed with an increase in the doping concentration. The increase in V_{oc} is attributed to the increase in optical absorption. Synergistic effect of band gap reduction and complete diffusion of dye molecules into the photoanode caused an increase in optical absorption. Moreover, the presence of Mg retarded the charge recombination thereby, enhancing the photocurrent (Liu, 2014; Tanyi et al., 2015). The efficiencies of the DSSCs fabricated using undoped, 1 mol% Mg doped and 2 mol% Mg doped TiO_2 were calculated to be 3.41, 4.05 and 6.10 %, respectively. However, further increase in doping concentration could be detrimental for the performance of DSSCs due to formation of electron trapping sites and grain boundaries (Liu, 2014). It can also be observed that a further increase in efficiency of the DSSCs can be seen when the conventional Pt/ITO CE was replaced with modified AuW/Pt/ITO CE in 2 mol% Mg doped TiO_2 based DSSC. The AuW/Pt/ITO CE was selected for performance compatibility studies as it showed the maximum power conversion efficiency when compared to other modified CEs (AgW/Si and AgW/ITO).

5.2 Electrophoretically Deposited TiO_2 Films with Sn Surface Modification

EPD is a deposition technique in which electric field induced charged particles are electrochemically deposited (Raphael et al., 2017). The charged particles are present in a suspension of electrolyte, solvent and additives. Particles present in this suspension are first charged and then drifted towards the electrode or the substrate for deposition (Chang et al., 2010; Tsai et al., 2010). Additives were added and different electric fields were applied to gain control over the packing density of the films. Yum et al (2005) noticed that using the electrolysis of water, hydrogen gas is produced which forms pores in the films during deposition. This led to the deposition of films with lower packing density thereby, adding to the merits of EPD. High controllability, easy deposition process and ability to tune film characteristics are the few merits that EPD offers. In this section, fabrication of TiO_2 photoanode using EPD has been discussed and the compatibility of the best photoanode was studied with modified AuW/Pt/ITO CE.

5.2.1 Morphological and Elemental Analysis

A major drawback of using EPD for TiO_2 films is the cracking of the film. Hamadanian et al. (2012) noticed the size of cracks for one step EPD of TiO_2 increased with increase in layer thickness. The cracks reached to the substrate and significantly degraded the performance of DSSC. Figure 5.10 shows the SEM images of the films fabricated using single step EPD and multistep EPD at 20 V. Film deposited using single step EPD at 20 V contains high density of the cracks as shown in Figure 5.10(a,b). The formation of cracks was noticed during the evaporation of the solvent and the drying of the films. Meanwhile, the TiO_2 film fabricated using multistep EPD (Figure 5.10(c)) is homogenous and crack-free. During the fabrication of multistep EPD films, the films were dried after each step due to which the crack density was observed to be significantly reduced.

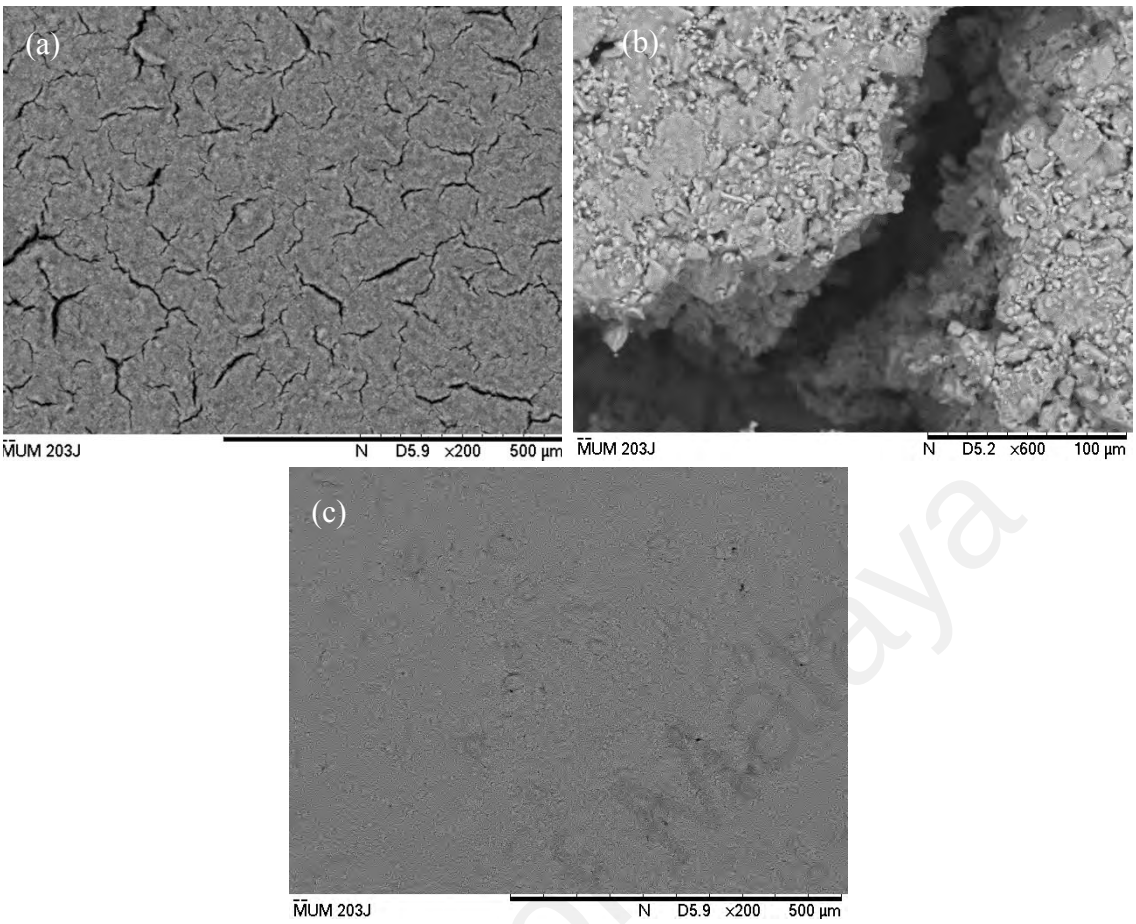

Figure 5.10: SEM images showing TiO_2 films fabricated using (a) single step EPD at 20 V, (b) magnified image of single step EPD at 20 V and (c) multistep EPD at 20 V.

The FESEM images of the TiO_2 films formed using multistep EPD at various electric fields are shown in Figure 5.11**.** It is evident from the figures that all almost crack-free films were obtained at all electric fields. The uniformity of the films increased and films became denser, as the electric field was increased from 10 to 20 V. This observation is in agreement with the previously reported results (Yum et al., 2005). The reason could be attributed to the drop in EPD current with a rise in electric field. During the deposition process, hydrolysis of water takes place at the cathode, which is directly proportional to the EPD current. The hydrolysis of water results in release of hydrogen (H_2) gas. When the EPD current is high, more H_2 gas releases disrupting the deposition process and creating pores in the film.

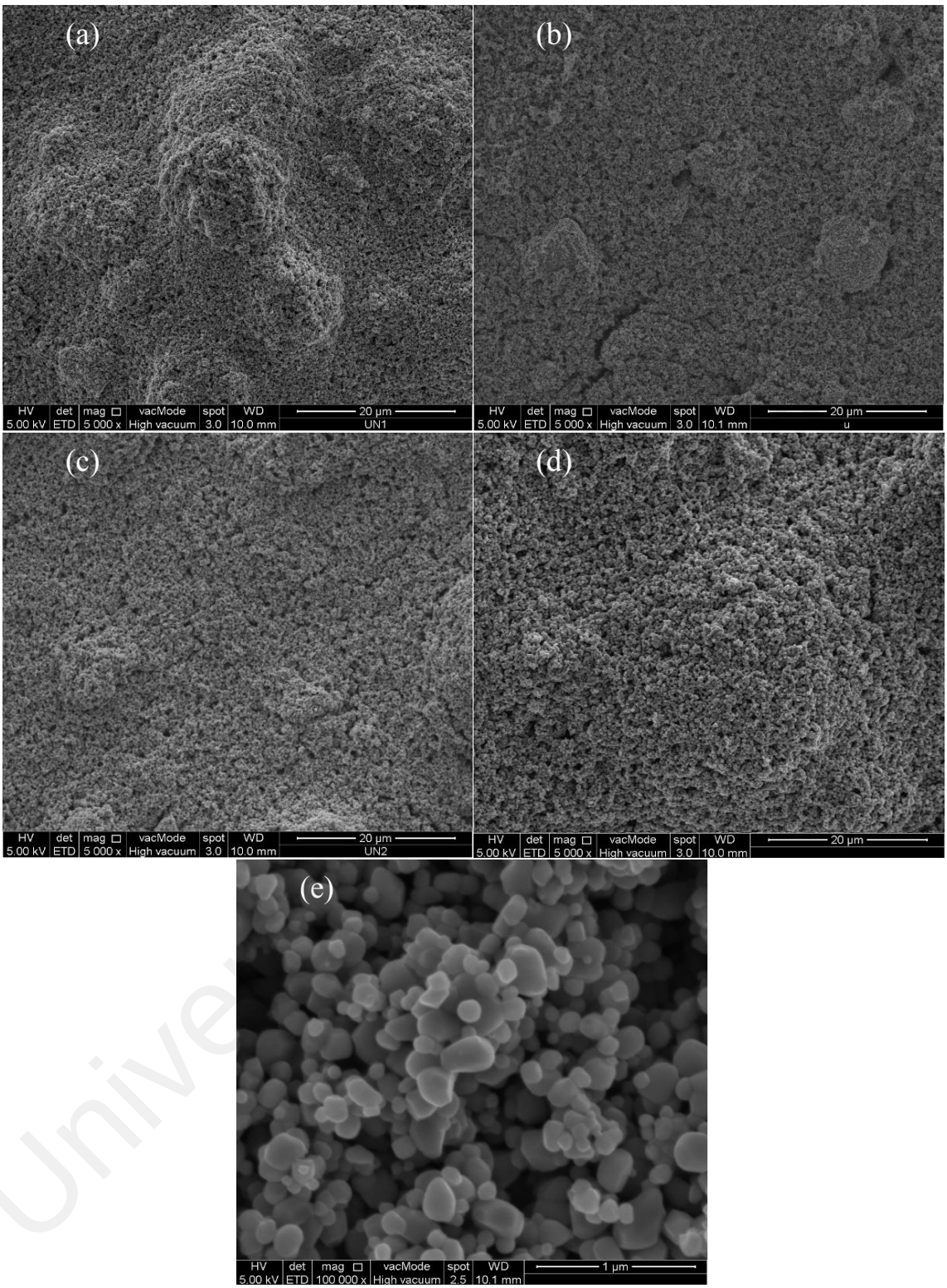

Figure 5.11: FESEM images of TiO_2 films deposited by EPD at (a) 10 V, (b) 15 V, (c) 20 V, (d) 20 V with Sn surface modification and (e) magnified image of 20 V with Sn surface modification.

An optimized dense nature of the films is very significant for performance of photoanode. Too dense film results in limited absorption of dye, while too porous film results in poor light absorption. Although, the film obtained at 20 V electric field appeared denser than the rest of the films, it was found to be more homogenous and was chosen for further surface modification. Bandy et al. (2011) observed similar results for film optimization (Bandy et al., 2011). The thickness of the films was measured using surface profiler and was found to be between 12-15 μm.

It can be observed from Figure 5.11(c, d) that on treatment of TiO_2 film deposited at 20 V with Sn, surface modification occurs. The morphology of the film appears more spherical and porous after the treatment. Presence of Sn on TiO_2 was also confirmed by EDX results, as shown in Figure 5.12. No impurities in any film could be observed confirming the complete removal of electrolyte and other elemental species during annealing, washing and drying. The nucleation and growth of Sn on TiO_2 are based on sono-chemical process in which TiO_2 particles act as a seed for Sn particles. Sonication process induces collapse of the bubbles resulting in excitation of the electrons in CB of TiO_2. Generation of these electrons cause an accumulation of negative charge on the surface of TiO_2 which attract Sn cations due to electrostatic interactions. The Sn cations are reduced to Sn particles. The electrons keep generating till the sonication process continues and attract more Sn cations, thereby leading to the growth of Sn particles.

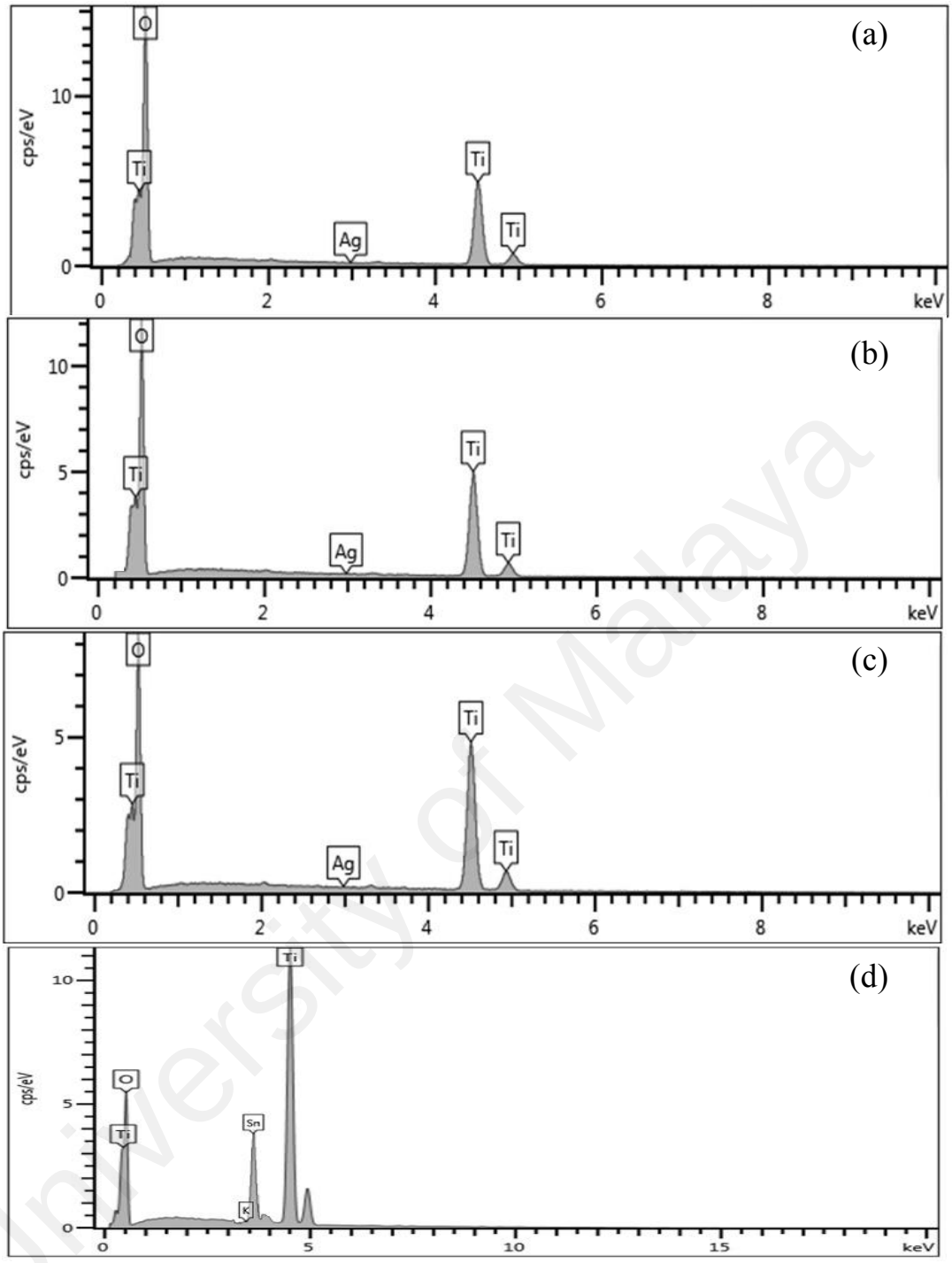

Figure 5.12: EDX spectra of TiO_2 films deposited using EPD at (a) 10 V, (b) 15 V, (c) 20 V and (d) 20 V with Sn surface modification.

5.2.2 Crystal Structure, Phase and Crystallite Size Analysis

To study the phases and purity of the films, XRD analysis was conducted and the spectra are shown in Figure 5.13. The diffraction peaks for anatase and rutile phases can be observed; anatase being the dominant phase. This shows that anatase and rutile phases co-exist in the films. Moreover, no peaks due to impurities were observed. As the electric field was increased, an increase in intensity of the peaks can be observed attributed to the increase in the crystallinity of the films. However, with Sn interaction, a slight decrease in peak intensity occurred. This implies that Sn interacted with TiO_2 which affected the XRD peak intensity. No peak for Sn metal or oxide was observed.

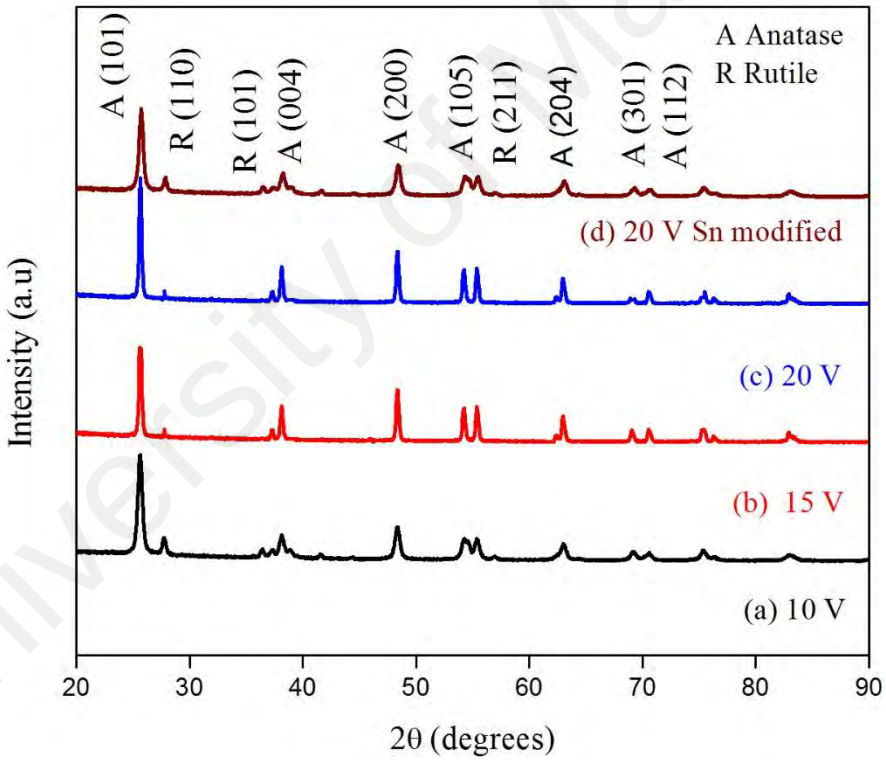

Figure 5.13: XRD spectra of for TiO_2 deposited films by EPD at (a) 10 V, (b) 15 V, (c) 20 V and (d) 20 V with Sn modification.

Crystallite size for films deposited at 10, 15, 20 and 20 V with Sn modification were calculated using Scherer equation (4.1) and estimated to be 21, 23, 24 and 19 nm, respectively. Films with higher crystallinity possess greater crystallite size (Caruntu et

al., 2006). This indicates that increasing the electric field for deposition had positive effect on the crystallinity of the films.

5.2.3 Raman Analysis

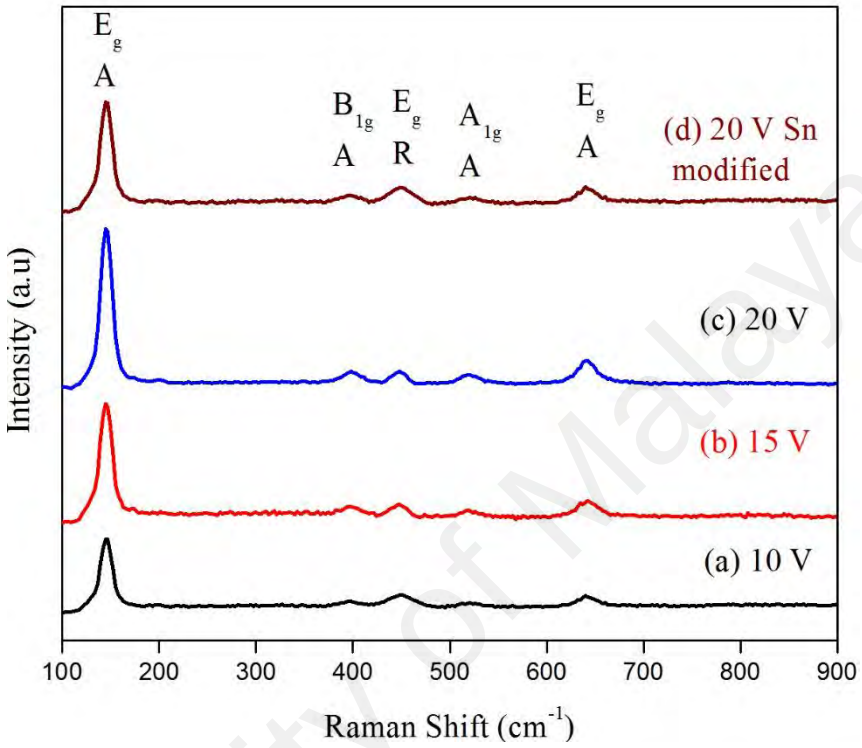

Figure 5.14: Raman Spectra for TiO_2 deposited films by EPD at (a) 10 V, (b) 15 V, (c) 20 V and (d) 20 V with Sn modification.

Raman spectroscopy was employed to further study the crystalline nature of the TiO_2 films deposited at various electric fields and the spectra are shown in Figure 5.14. The Raman active modes originate due to the vibration of molecular bonds. Each molecular bond on different crystal facets have characteristic Raman active mode. According to factor group analysis, six Raman transitions are allowed; $3E_g$, $2B_{1g}$ and $1A_{1g}$ for anatase phase of TiO_2 and five Raman transitions are allowed for rutile phase: E_g, A_{1g}, B_{1g}, B_{2g} and multi proton process (Yan et al., 2013). In our films, 2 Eg, B_{1g} and A_{1g} Raman active modes can be observed at 140 cm^{-1}, 635 cm^{-1}, 395 cm^{-1} and 515 cm^{-1}, respectively, for the anatase phase of TiO_2. One active mode for rutile phase was observed for E_g at 445 cm^{-1}.

It can be deduced from these results that the anatase and rutile phases of TiO_2 remained well preserved for the deposition at different electric field intensities. No change in Raman shift was observed for the studied films. However, with increase in the electric field intensity, an increase in intensity of Raman spectra can be observed, attributed to the increase in crystallinity of the films. On surface modification with Sn, a shift in the intensity of Raman peaks can be observed confirming the interaction of Sn with TiO_2 film.

5.2.4 BET Surface Area and Pore Size Analysis of the Films

Figure. 5.15 shows the N_2 adsorption-desorption curves for the films fabricated at various electric fields and the Sn modified film and the surface area and average pore size diameter are summarized in Table 5.4. It can be observed that upon increasing the electric field, the average pore diameter of the films increases. A slight decrease in surface area can be observed. These results are consistent with the morphological analysis using FESEM. On interaction with Sn, the surface area and the average pore diameter almost remains the same with a slight increase in the surface area. The pore diameter of the film significantly affects the performance of the DSSCs. In order to enhance the durability of DSSCs, t is important that the dye molecules and the electrolyte diffuse through the surface of the film and fill the porous films completely (Benedetti et al., 2010; Weisspfennig et al., 2014). Moreover, large pores also result in higher electron lifetime (Wang et al., 2013). The high diffusion of dye molecules and electrolyte in the film decreases the resistance at the interface of TiO_2/dye/electrolyte leading to increased J_{sc}. Small pore size inhibits the complete diffusion of dye and electrolyte.

Table 5.4: The average pore volume and the surface area of films deposited at various electric fields.

TiO_2 Film electric field	Surface area (m^2g^{-1})	Average pore diameter (nm)
10 V	78.4	5.2
15 V	77.2	6.5
25 V	75.6	7.5
25 V with Sn modification	75.9	7.3

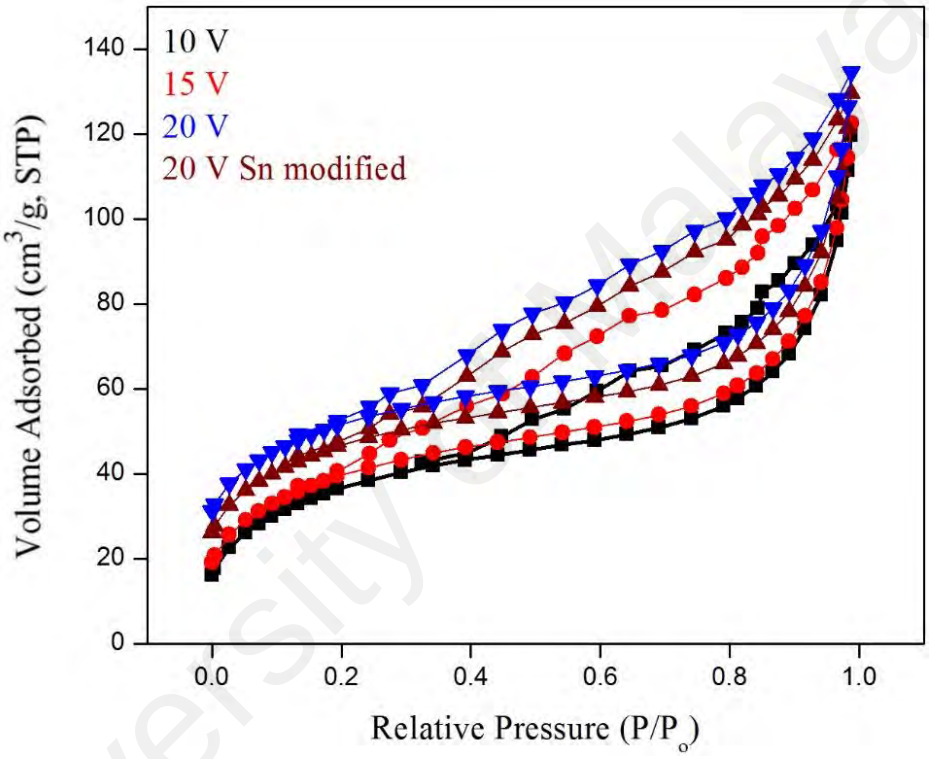

Figure 5.15: Nitrogen adsorption-desorption curves for the TiO_2 films deposited at 10 V, 15 V, 20 V and 20 V with Sn modification.

5.2.5 Optical Properties of the Films

UV-vis absorption spectra, shown in Figure 5.16, for TiO_2 film deposited at 20 V and the film with Sn modification was obtained in order to study the effect of Sn modification on optical properties and the band gap of the film. On Sn modification, a red shift in absorbance spectra can be observed.

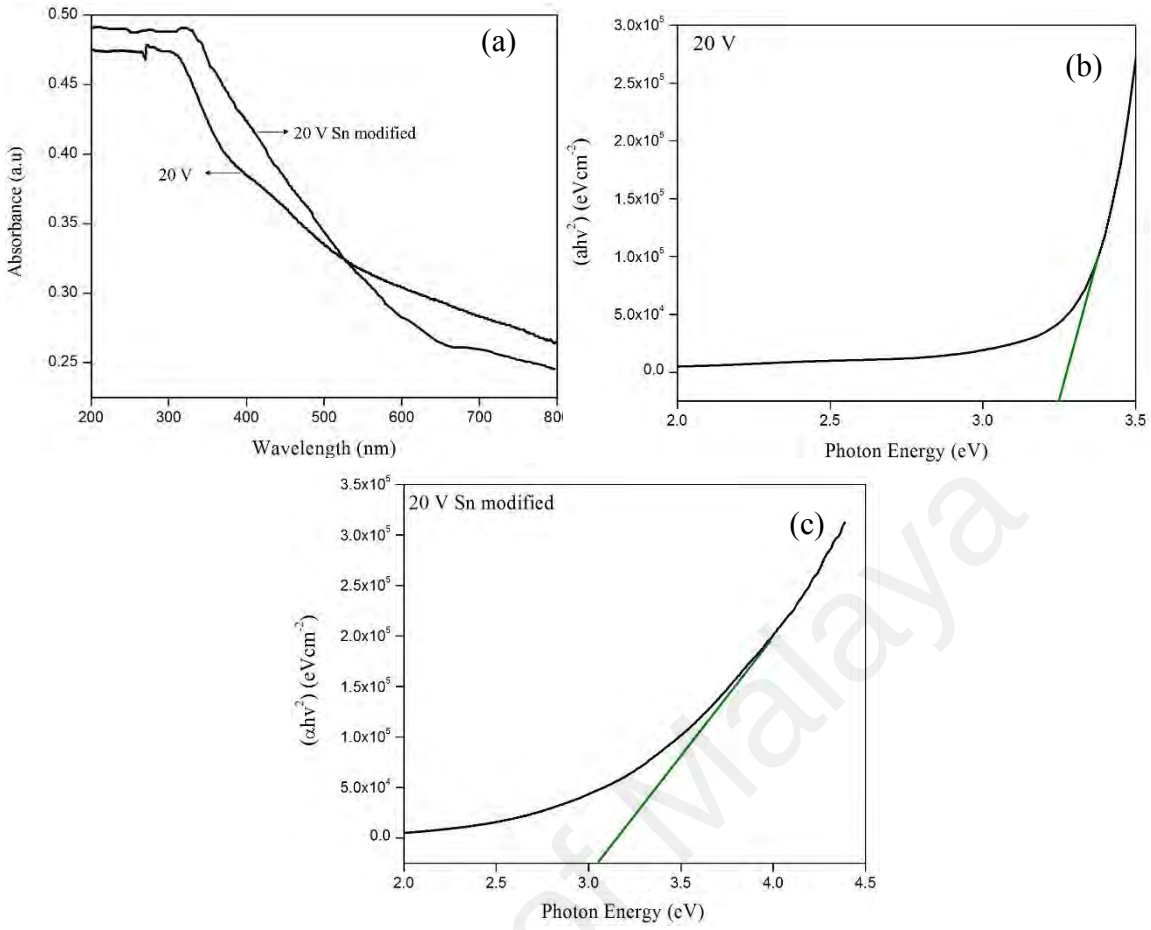

Figure 5.16: Images showing (a) UV-vis spectra of film deposited at 20 V before and after Sn modification (b) Tauc's plot for the film deposited at 20 V (b) before and (c) after Sn modification.

Band gap energies were estimated using Tauc's plot [$(\alpha hv)^{\gamma}$ *v/s* hv], where α, hv, E_g and A are the linear absorption coefficient, photon energy, band gap energy and proportionality constant, respectively and γ determines the characteristics of transition in a semiconductor. A value γ=1/2 is assigned for direct bandgap and γ=2 is assigned for indirect band gap (López & Gómez, 2012; Sönmezoğlu et al., 2011). Values of band gap for undoped and doped films were obtained by extrapolation of the linear region in the plots of $(\alpha hv)^{1/2}$ to its intersection with energy axis (hv/eV). The band gap energy for TiO_2 film deposited at 20 V was estimated to be 3.3 eV, which is consistent with previously reported band gap value (G. Wang et al., 2012). A decrease in band gap energy of the film was observed on Sn modification (3.1 eV).

5.2.6 J-V Characteristics of the DSSCs

J-V characteristics of the DSSCs fabricated using studied photoanodes are shown in Figure 5.17 and summarized in Table 5.5.

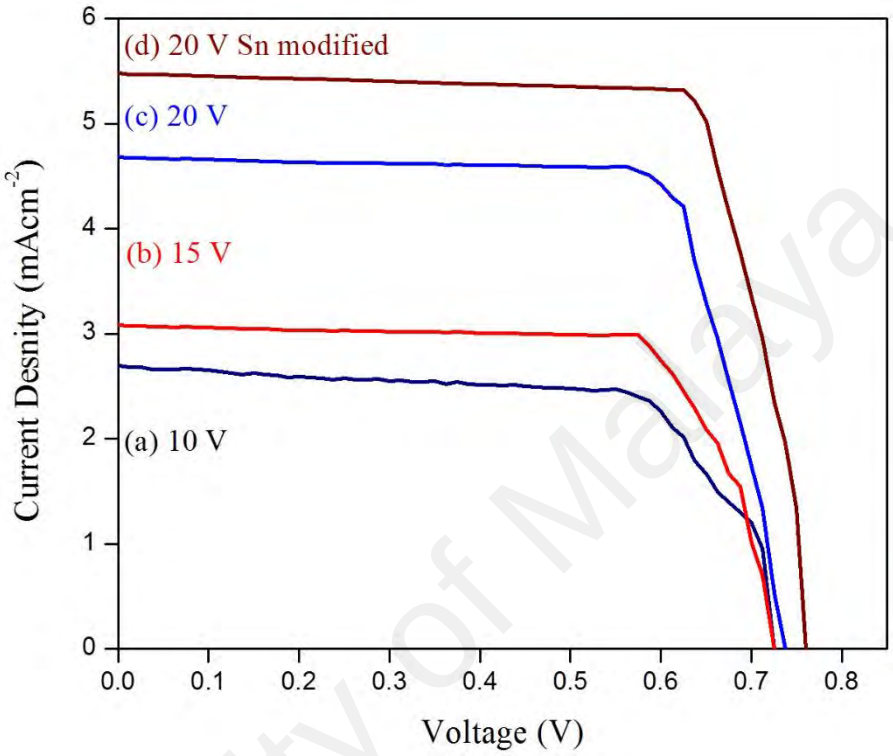

Figure 5.17: J-V characteristics of DSSCs fabricated using TiO_2 photoanodes deposited using EPD at 10 V, 15 V, 20 V, 20 V with Sn modification.

Table 5.5: Summary of the parameters from J-V curves.

DSSC based on photoanode film deposited at	V_{oc} (V)	J_{sc} $mAcm^{-2}$	FF	η (%)
10 V TiO_2 film	0.67	2.69	0.67	1.28±0.05
15 V TiO_2 film	0.71	3.07	0.77	1.71±0.03
20 V TiO_2 film	0.72	4.67	0.77	2.65±0.04
20 V with Sn modification TiO_2 film	0.76	5.48	0.78	3.32±0.03
20 V Sn modification based DSSC with AuW/Pt/ITO CE	0.75	5.20	0.56	2.20±0.02

An enhancement in η of the DSSCs can be observed with an increase in the electric field owing to the increased homogeneity and porosity of the film. TiO_2/dye/electrolyte interface exhibited lower resistance due to large pore diameter. Sn modification further enhanced the photovoltaic characteristics attributed to the lowering of the band gap and enhancement in photoabsorption.

Sn interaction with TiO_2 lattice caused a change in the Fermi level of the TiO_2. Therefore, the generated electron in CB of TiO_2 was captured by the Sn. Meanwhile, the Fermi level equilibrium was attained. The capture of the generated electron by Sn, increased the lifetime of the holes, thereby, suppressing the hole-electron recombination. However, using AuW/Pt/ITO CE unexpectedly decreased the photovoltaic performance of the DSSC (Figure 5.18). A significant decrease in fill factor and efficiency can be observed in DSSCs where conventional Pt/ITO CE was replaced with AuW/Pt/ITO CE. This could be attributed to an unknown reaction occurring in the DSSC due to presence of Sn on the surface of photoanode.

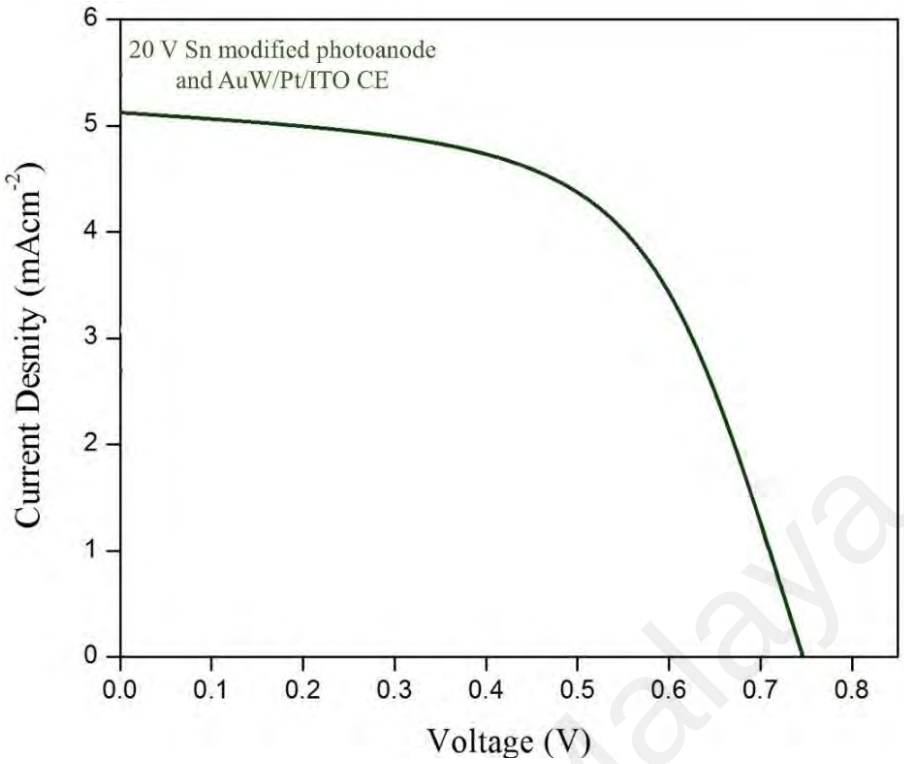

Figure 5.18: J-V curves for DSSC based on Sn modified-20 V EPD deposited photoanode and AuW/Pt/ITO CE.

5.3 Comparison of the Results based on Photoanode Studies

In this section, the performance of DSSCs have been compared on the bases of different modified photoanodes and modified CE (AuW/Pt/ITO).

5.3.1 Morphological Comparison of Films Deposited using AACVD and EPD

The morphological analysis of the films fabricated using AACVD and EPD revealed that EPD films were denser as compared to films deposited using AACVD thereby, having higher surface area and lower porosity. These results were supported by N_2 adsorption-desorption curves and the acquired data of the films deposited using AACVD and EPD are summarized in Table 5.6.

Table 5.6: Summary of BET surface area and average pore diameter of films deposited using AACVD and EPD methods.

TiO_2 film		Surface area (m^2g^{-1})	Average pore diameter (nm)
Deposition Method	**Variant**		
AACVD	Undoped TiO_2	69.2	3.0
AACVD	1 mol% Mg doped TiO_2	67.5	4.0
AACVD	2 mol% Mg doped TiO_2	66.1	5.0
EPD	Electric field 10 V	78.4	5.2
EPD	Electric field 15 V	77.2	6.5
EPD	Electric field 25 V	75.6	7.5
EPD	Electric field 25 V with Sn modification	75.9	7.3

5.3.2 Device Performance Comparison based on Modified Photoanodes and CEs

The maximum performance efficiency of DSSC device among all the studied samples was for the DSSCs fabricated using AACVD 2 mol% Mg doped TiO_2 photoanode and AuW/Pt/ITO cathode with an efficiency of 6.68 %. This indicates that these modified CE and photoanodes were compatible with each other in a single device. The enhanced photoabsorption, reduction in recombination and quick electron transfer from CE to electrolyte caused an increase in the photovoltaic performance of the DSSC.

CHAPTER 6: CONCLUSIONS AND FUTURE WORKS

6.1 Conclusions

It is concluded that conductive and well-connected Ag and Au wires can be fabricated using DNA and RNA templating methods on various substrates, which can be used as CE in DSSCs due to their enhanced catalytic properties. The novel technique employed in this study demonstrates the promising prospects of an easy and highly controllable method for fabricating conductive metal wires. The results demonstrate the successful removal of the RNA residue using simple and cost-effective cleaning method to yield clean Ag wires. Moreover, we have successfully fabricated well-connected DNA templated Ag wires on ITO and Au wires on Pt/ITO substrates to be used as a modified CE in DSCCs. Fabrication of RNA templated Ag wires on Si wafer and DNA templated Au and Ag wires on ITO and conventional Pt/ITO CE, respectively, enhanced the catalytic activity of the CEs thereby, enhancing the reaction kinetics and reducing the I_3^- reduction over potential. This substitution enhanced the overall performance of the DSSCs as shown by the increased efficiency of the cells fabricated using AuW/Pt/ITO CEs. Addition of appropriate amounts of SDS surfactant significantly reduced Marangoni flow of the Ag-DNA complexes to avoid the deposition of Ag wires anywhere less than the edges of the scribe. Another important conclusion observed was the dependency of heights of the wires on the scaffold. When using DNA as a scaffold it was observed that the average height of the wires decreased. Annealing also significantly reduced the average height of the wire and the crystallite size as well making the material in nanoscale. Among these fabricated wires on various substrates, DSSCs assembled using AuW/Pt/ITO CE showed the maximum photovoltaic performance.

In order to develop more compatible photoanodes with our modified CEs, AACVD and EPD methods were used with Mg doping and Sn modification of TiO_2 films,

respectively. Mg doping and Sn modification enhanced the optical absorption and reduced the band gaps of the TiO_2 films. The modifications were beneficial for the working of the photoanode which enhanced the performance of the DSSCs. These modified electrodes were assembled with AuW/Pt/ITO CEs which showed that these CEs were highly compatible with Mg doped AACVD photoanode. However, with EPD deposited-Sn modified TiO_2 films, a decrease in efficiency was observed when the conventional Pt/ITO CE was replaced with our modified CE. The maximum performance efficiency of DSSC device among all the studied samples was for the ones fabricated using AACVD 2 mol% Mg doped TiO_2 photoanode and AuW/Pt/ITO cathode with an efficiency of 6.68 %.

6.2 Future Works

Improvements in the process by optimization of physical conditions and concentrations of RNA and metal NPs could lead to further controllable printing of the metal wires and nano-patterns. Future research using programmable ion or electron beam writing methods could eventually pave the way forward for integration within an industrial environment for mass-produced nano-circuits for applications in nano electronics. Furthermore, high precision scribing methods like electron beam lithography could be used in future to fabricate DNA templated Au nanostructures with high controllability, which can be expected to further enhance the photovoltaic properties of the DSSCs.

REFERENCES

Aberle, A. G. (2009). Thin-film solar cells. *Thin Solid Films, 517*(17), 4706-4710.

Al-Hinai, M. N., Hassanien, R., Wright, N. G., Horsfall, A. B., Houlton, A., & Horrocks, B. R. (2013). Networks of DNA-templated palladium nanowires: structural and electrical characterisation and their use as hydrogen gas sensors. *Faraday Discussions, 164*, 71-91.

Al-Said, S. A. F., Hassanien, R., Hannant, J., Galindo, M. A., Pruneanu, S., Pike, A. R., Horrocks, B. R. (2009). Templating Ag on DNA/polymer hybrid nanowires: Control of the metal growth morphology using functional monomers. *Electrochemistry Communications, 11*(3), 550-553.

Andersen, E. S., Dong, M., Nielsen, M. M., Jahn, K., Subramani, R., Mamdouh, W., Oliveira, C. L. (2009). Self-assembly of a nanoscale DNA box with a controllable lid. *Nature, 459*(7243), 73.

Arakawa, H., Ahmad, R., Naoui, M., & Tajmir-Riahi, H.-A. (2000). A comparative study of calf thymus DNA binding to Cr (III) and Cr (VI) ions evidence for the guanine N-7-chromium-phosphate chelate formation. *Journal of Biological Chemistry, 275*(14), 10150-10153.

Arakawa, H., Neault, J., & Tajmir-Riahi, H. (2001). Silver (I) complexes with DNA and RNA studied by Fourier transform infrared spectroscopy and capillary electrophoresis. *Biophysical Journal, 81*(3), 1580-1587.

Bahramian, A. (2013). High conversion efficiency of dye-sensitized solar cells based on coral-like TiO_2 nanostructured films: synthesis and physical characterization. *Industrial & Engineering Chemistry Research, 52*(42), 14837-14846.

Bai, X., Liao, S., Huang, Y., Song, J., Liu, Z., Fang, M., Wu, H. (2017). Continuous Draw Spinning of Extra-Long Silver Submicron Fibers with Micrometer Patterning Capability. *Nano Letters, 17*(3), 1883-1891.

Bates, A. D., Callen, B. P., Cooper, J. M., Cosstick, R., Geary, C., Glidle, A., Xu, C. (2006). Construction and Characterization of a Gold Nanoparticle Wire Assembled Using Mg2+-Dependent RNA− RNA Interactions. *Nano Letters, 6*(3), 445-448.

Becerril, H. A., Ludtke, P., Willardson, B. M., & Woolley, A. T. (2006). DNA-templated nickel nanostructures and protein assemblies. *Langmuir, 22*(24), 10140-10144.

Benedetti, J. E., Gonçalves, A. D., Formiga, A. L., De Paoli, M.-A., Li, X., Durrant, J. R., & Nogueira, A. F. (2010). A polymer gel electrolyte composed of a poly (ethylene oxide) copolymer and the influence of its composition on the dynamics and performance of dye-sensitized solar cells. *Journal of Power Sources, 195*(4), 1246-1255.

Bensimon, D., Simon, A., Croquette, V., & Bensimon, A. (1995). Stretching DNA with a receding meniscus: experiments and models. *Physical Review Letters,* 74(23), 4754.

Ben-Romdhane, N., Zhao, W. S., Zhang, Y., Klein, J. O., Wang, Z. H., & Ravelosona, D. (2014). Design and analysis of racetrack memory based on magnetic domain wall motion in nanowires. In Proceedings of the 2014 IEEE/ACM International Symposium on Nanoscale Architectures, 71-76.

Binnig, G., Quate, C. F., & Gerber, C. (1986). Atomic force microscope. *Physical Review Letters, 56*(9), 930.

Bolton, P., & Kearns, D. (1978). Hydrogen bonding of the 2′ OH in RNA. *Biochimica et Biophysica Acta (BBA)-Nucleic Acids and Protein Synthesis, 517*(2), 329-337.

Braun, E., Eichen, Y., Sivan, U., & Ben-Yoseph, G. (1998). DNA-templated assembly and electrode attachment of a conducting silver wire. *Nature, 391*(6669), 775.

Brinton, C. C. (1965). The structure, function, synthesis and genetic control of bacterial pili and a molecular model for DNA and RNA transport in gram negative bacteria. *Transactions of the New York Academy of Sciences, 27*(8 Series II), 1003-1054.

Brumlik, C. J., Menon, V. P., & Martin, C. R. (1994). Template synthesis of metal microtubule ensembles utilizing chemical, electrochemical, and vacuum deposition techniques. *Journal of Materials Research, 9*(5), 1174-1183.

Bumbrah, G. S., & Sharma, R. M. (2016). Raman spectroscopy–Basic principle, instrumentation and selected applications for the characterization of drugs of abuse. *Egyptian Journal of Forensic Sciences, 6*(3), 209-215.

Burnham, N., Cruceanu, F., Dong, Q., & Thompson, N. (2004). An introduction to atomic force microscopy. *Computer, 10*, 800V.

Butt, H.-J., Cappella, B., & Kappl, M. (2005). Force measurements with the atomic force microscope: Technique, interpretation and applications. *Surface Science Reports, 59*(1), 1-152.

Cao, G. (2004). *Nanostructures and nanomaterials: synthesis, properties and applications*: *Imperial College Press*.

Caruntu, G., Rarig Jr, R., Dumitru, I., & O'Connor, C. J. (2006). Annealing effects on the crystallite size and dielectric properties of ultrafine $Ba_{1-x}Sr_xTiO_3$ ($0< x< 1$) powders synthesized through an oxalate-complex precursor. *Journal of Materials Chemistry, 16*(8), 752-758.

Cate, J. H., Gooding, A. R., Podell, E., Zhou, K., Golden, B. L., Kundrot, C. E., Doudna, J. A. (1996). Crystal structure of a group I ribozyme domain: principles of RNA packing. *Science, 273*(5282), 1678-1685.

Cavallo, C., Di Pascasio, F., Latini, A., Bonomo, M., & Dini, D. (2017). Nanostructured semiconductor materials for dye-sensitized solar cells. *Journal of Nanomaterials, 2017*.

Chang, H., Chen, T.-L., Huang, K.-D., Chien, S.-H., & Hung, K.-C. (2010). Fabrication of highly efficient flexible dye-sensitized solar cells. *Journal of Alloys and Compounds, 504*, S435-S438.

Chan, C. K., Peng, H., Liu, G., McIlwrath, K., Zhang, X. F., Huggins, R. A., & Cui, Y. (2008). High-performance lithium battery anodes using silicon nanowires. Nature Nanotechnology, 3(1), 31.

Chen, F.-C., Lu, J.-P., & Huang, W.-K. (2009). Using ink-jet printing and coffee ring effect to fabricate refractive microlens arrays. *IEEE Photonics Technology Letters, 21*(10), 648-650.

Chen, L.-C., Hsieh, C.-T., Lee, Y.-L., & Teng, H. (2013). Electron Transport Dynamics in TiO_2 Films Deposited on Ti Foils for Back-Illuminated Dye-Sensitized Solar Cells. *ACS Applied Materials & Interfaces, 5*(22), 11958-11964.

Cheng, W., Campolongo, M. J., Tan, S. J., & Luo, D. (2009). Freestanding ultrathin nano-membranes via self-assembly. *Nano Today, 4*(6), 482-493.

Chong, S. K., Goh, B. T., Dee, C. F., & Rahman, S. A. (2013). Effect of substrate to filament distance on formation and photoluminescence properties of indium catalyzed silicon nanowires using hot-wire chemical vapor deposition. *Thin Solid Films, 529*, 153-158.

Chworos, A., Severcan, I., Koyfman, A. Y., Weinkam, P., Oroudjev, E., Hansma, H. G., & Jaeger, L. (2004). Building programmable jigsaw puzzles with RNA. S*cience, 306*(5704), 2068-2072.

Colinge, J. P., Lee, C. W., Afzalian, A., Akhavan, N. D., Yan, R., Ferain, I., & Kelleher, A. M. (2010). Nanowire transistors without junctions. Nature Nanotechnology, 5(3), 225.

Dablemont, C., Lang, P., Mangeney, C., Piquemal, J.-Y., Petkov, V., Herbst, F., & Viau, G. (2008). FTIR and XPS study of Pt nanoparticle functionalization and interaction with alumina. *Langmuir, 24*(11), 5832-5841.

Dai, S., Zhang, X., Li, T., Du, Z., & Dang, H. (2005). Preparation of silver nanopatterns on DNA templates. *Applied Surface Science, 249*(1), 346-353.

Dao, V.-D., & Choi, H.-S. (2015). Pt nanourchins as efficient and robust counter electrode materials for dye-sensitized solar cells. *ACS Applied Materials & Interfaces, 8*(1), 1004-1010.

Dao, V.-D., Kim, S.-H., Choi, H.-S., Kim, J.-H., Park, H.-O., & Lee, J.-K. (2011). Efficiency enhancement of dye-sensitized solar cell using Pt hollow sphere counter electrode. *The Journal of Physical Chemistry C, 115*(51), 25529-25534.

Deegan, R. D., Bakajin, O., Dupont, T. F., & Huber, G. (1997). Capillary flow as the cause of ring stains from dried liquid drops. *Nature, 389*(6653), 827.

Deegan, R. D., Bakajin, O., Dupont, T. F., Huber, G., Nagel, S. R., & Witten, T. A. (2000). Contact line deposits in an evaporating drop. *Physical Review E, 62*(1), 756.

Deng, Z., & Mao, C. (2003). DNA-templated fabrication of 1D parallel and 2D crossed metallic nanowire arrays. *Nano Letters, 3*(11), 1545-1548.

Desilvestro, J., Graetzel, M., Kavan, L., Moser, J., & Augustynski, J. (1985). Highly efficient sensitization of titanium dioxide. *Journal of the American Chemical Society, 107*(10), 2988-2990.

Dey, V., Kachala, R., Bonakdar, A., & Mobasher, B. (2015). Mechanical properties of micro and sub-micron wollastonite fibers in cementitious composites. *Construction and Building Materials, 82*, 351-359.

Dibrov, S. M., McLean, J., Parsons, J., & Hermann, T. (2011). Self-assembling RNA square. *Proceedings of the National Academy of Sciences, 108*(16), 6405-6408.

Donghi, D., & Sigel, R. K. (2012). Metal ion–RNA interactions studied via multinuclear NMR. *Ribozymes: Methods and Protocols*, 253-273.

Doria, G., Conde, J., Veigas, B., Giestas, L., Almeida, C., Assunção, M., Baptista, P. V. (2012). Noble metal nanoparticles for biosensing applications. *Sensors, 12*(2), 1657-1687.

Dubey, R., & Singh, S. (2017). Investigation of structural and optical properties of pure and chromium doped TiO_2 nanoparticles prepared by solvothermal method. *Results in Physics, 7*, 1283-1288.

Duguid, J., Bloomfield, V. A., Benevides, J., & Thomas, G. (1993). Raman spectroscopy of DNA-metal complexes. I. Interactions and conformational effects of the divalent cations: Mg, Ca, Sr, Ba, Mn, Co, Ni, Cu, Pd, and Cd. *Biophysical journal, 65*(5), 1916-1928.

Eber, F. J., Eiben, S., Jeske, H., & Wege, C. (2015). RNA-controlled assembly of tobacco mosaic virus-derived complex structures: from nanoboomerangs to tetrapods. *Nanoscale, 7*(1), 344-355.

Ehira, M., & Egami, A. (1995). Mechanical properties and microstructures of submicron cermets. *International Journal of Refractory Metals and Hard Materials, 13*(5), 313-319.

Eichhorn, G. L., & Shin, Y. A. (1968). Interaction of metal ions with polynucleotides and related compounds. XII. The relative effect of various metal ions on DNA helicity. *Journal of the American Chemical Society, 90*(26), 7323-7328.

Eisinger, J., Shulman, R., & Szymanski, B. (1962). Transition metal binding in DNA solutions. *The Journal of Chemical Physics, 36*(7), 1721-1729.

Enache-Pommer, E., Liu, B., & Aydil, E. S. (2009). Electron transport and recombination in dye-sensitized solar cells made from single-crystal rutile TiO_2 nanowires. *Physical Chemistry Chemical Physics, 11*(42), 9648-9652.

Engelhard, M. H., Droubay, T. C., & Du, Y. (2017). X-Ray Photoelectron Spectroscopy Applications A2 - Lindon, John C. In G. E. Tranter & D. W. Koppenaal (Eds.), *Encyclopedia of Spectroscopy and Spectrometry, 3,* 716-724.

Frank, L., Hovorka, M., Mikmeková, Š., Mikmeková, E., Müllerová, I., & Pokorná, Z. (2012). Scanning electron microscopy with samples in an electric field. *Materials, 5*(12), 2731-2756.

Frankel, R., & Aitken, D. (1970). Energy-dispersive x-ray emission spectroscopy. *Applied Spectroscopy, 24*(6), 557-566.

Freisinger, E., & Sigel, R. K. (2007). From nucleotides to ribozymes—a comparison of their metal ion binding properties. *Coordination Chemistry Reviews, 251*(13), 1834-1851.

Fujishima, A. (1972). Electrochemical photolysis of water at a semiconductor electrode. *Nature, 238*, 37-38.

Gazit, E. (2007). Use of biomolecular templates for the fabrication of metal nanowires. *The FEBS Journal, 274*(2), 317-322.

Gleiter, H. (1992). Materials With Ultrafine Microstructures: Retrospective and Perspectives. *NanoStructured Materials*, 1(1), 1-19.

Goetzberger, A., Hebling, C., & Schock, H.-W. (2003). Photovoltaic materials, history, status and outlook. *Materials Science and Engineering: R: Reports, 40*(1), 1-46.

Grabow, W. W., Zakrevsky, P., Afonin, K. A., Chworos, A., Shapiro, B. A., & Jaeger, L. (2011). Self-assembling RNA nanorings based on RNAI/II inverse kissing complexes. *Nano Letters, 11*(2), 878-887.

Grätzel, M. (2001). Photoelectrochemical cells. *Nature, 414*(6861), 338-344.

Grätzel, M. (2003). Dye-sensitized solar cells. *Journal of Photochemistry and Photobiology C: Photochemistry Reviews, 4*(2), 145-153.

Gu, Q., Cheng, C., Gonela, R., Suryanarayanan, S., Anabathula, S., Dai, K., & Haynie, D. T. (2005). DNA nanowire fabrication. *Nanotechnology, 17*(1), R14.

Guo, K., Li, M., Fang, X., Liu, X., Sebo, B., Zhu, Y., Zhao, X. (2013). Preparation and enhanced properties of dye-sensitized solar cells by surface plasmon resonance of Ag nanoparticles in nanocomposite photoanode. *Journal of Power Sources, 230*, 155-160.

Hackl, E. V., Kornilova, S. V., & Blagoi, Y. P. (2005). DNA structural transitions induced by divalent metal ions in aqueous solutions. *International Journal of Biological Macromolecules, 35*(3), 175-191.

Hamadanian, M., Sayahi, H., & Zolfaghari, A. R. (2012). Modified multistep electrophoretic deposition of TiO_2 nanoparticles to prepare high quality thin films for dye-sensitized solar cell. *Journal of Materials Science, 47*(15), 5845-5851.

Hamley, I. (2003). Nanotechnology with soft materials. *Angewandte Chemie International Edition, 42*(15), 1692-1712.

Hara, K., & Arakawa , H. (2005). Dye-Sensitized Solar Cells. *Handbook of Photovoltaic Science and Engineering*, 1, 663-700.

Haugstad, G. (2012). *Atomic force microscopy: understanding basic modes and advanced applications*: *John Wiley & Sons*, 2012, 1-32.

Haurwitz, R. E., Jinek, M., Wiedenheft, B., Zhou, K., & Doudna, J. A. (2010). Sequence- and structure-specific RNA processing by a CRISPR endonuclease. S*cience, 329*(5997), 1355-1358.

He, B., Tang, Q., Liang, T., & Li, Q. (2014). Efficient dye-sensitized solar cells from polyaniline–single wall carbon nanotube complex counter electrodes. *Journal of Materials Chemistry A, 2*(9), 3119-3126.

Heddle, J. G. (2013). Gold nanoparticle-biological molecule interactions and catalysis. *Catalysts, 3*(3), 683-708.

Hercules, D. M. (2004). Electron spectroscopy: Applications for chemical analysis. *Journal of Chemical Education, 81*(12), 1751.

Hsiao, P.-T., Tung, Y.-L., & Teng, H. (2010). Electron transport patterns in TiO_2 nanocrystalline films of dye-sensitized solar cells. *The Journal of Physical Chemistry C, 114*(14), 6762-6769.

Huang, S., Sun, H., Huang, X., Zhang, Q., Li, D., Luo, Y., & Meng, Q. (2012). Carbon nanotube counter electrode for high-efficient fibrous dye-sensitized solar cells. *Nanoscale Research Letters, 7*(1), 1-7.

Hud, N. V. (2009). Nucleic acid-metal ion interactions. *Royal Society of Chemistry, 14, 154-170.*

Jackson, P., Hariskos, D., Lotter, E., Paetel, S., Wuerz, R., Menner, R., Powalla, M. (2011). New world record efficiency for Cu (In, Ga) Se_2 thin-film solar cells beyond 20%. *Progress in Photovoltaics: Research and Applications, 19*(7), 894-897.

Jia, L., Wu, C., Han, S., Yao, N., Li, Y., Li, Z., Jian, L. (2011). Theoretical study on the electronic and optical properties of (N, Fe)-codoped anatase TiO_2 photocatalyst. *Journal of Alloys and Compounds, 509*(20), 6067-6071.

Jiménez-García, F., Segura-Giraldo, B., Restrepo-Parra, E., & López-López, G. (2015). Synthesis of TiO_2 thin films by the SILAR method and study of the influence of annealing on its structural, morphological and optical properties. *Ingeniare. Revista Chilena de Ingeniería, 23*(4), 622-629.

Joy, D. C. (2009). Scanning electron microscopy: Second best no more. *Nature Materials, 8*(10), 776-777.

Kasim, A., Hayaty, N., Govindasamy, V., Gnanasegaran, N., Musa, S., Pradeep, P. J., Aziz, Z. A. C. A. (2015). Unique molecular signatures influencing the biological function and fate of post-natal stem cells isolated from different sources. *Journal of Tissue Engineering and Regenerative Medicine, 9*(12), 252-266.

Keshavarzi, R., Mirkhani, V., Moghadam, M., Tangestaninejad, S., & Mohammadpoor-Baltork, I. (2015). Performance Enhancement of Dye-Sensitized Solar Cells Based on TiO_2 Thick Mesoporous Photoanodes by Morphological Manipulation. *Langmuir, 31*(42), 11659-11670.

Khan, M., Hou, S., Farooq, K., & Yi, X. (2013). Single photon reflection and transmission in optomechanical system. *International Journal of Quantum Information, 11*(02), 1350017.

Khan, M. A. M., Kumar, S., Ahamed, M., Alrokayan, S. A., & AlSalhi, M. S. (2011). Structural and thermal studies of silver nanoparticles and electrical transport study of their thin films. *Nanoscale Research Letters, 6*(1), 434.

Kim, Y. S., Yu, B.-K., Kim, J. W., Suh, Y.-H., Kim, D.-Y., & Kim, W. B. (2013). Building a hybrid nanocomposite assembly of gold nanowires and thienyl-derivative fullerenes to enhance electron transfer in photovoltaics. *Journal of Materials Chemistry A, 1*(16), 5015-5020.

Ko, S. H., Su, M., Zhang, C., Ribbe, A. E., Jiang, W., & Mao, C. (2010). Synergistic self-assembly of RNA and DNA molecules. *Nature Chemistry, 2*(12), 1050-1055.

Kudo, H., & Fujihira, M. (2006). DNA-templated copper nanowire fabrication by a two-step process involving electroless metallization. *IEEE Transactions on Nanotechnology, 5*(2), 90-92.

Kumar, A., & Gupta, K. (2017). RNA-mediated fluorescent colloidal CdSe nanostructures in aqueous medium–analysis of Cd^{2+} induced folding of RNA associated with morphological transformation (0D to 1D), change in photophysics and selective Hg^{2+} sensing. *Journal of Materials Chemistry A, 5*(13), 6146-6163.

Kumar, D., Singh, K., Verma, V., & Bhatti, H. (2015). Microwave-assisted synthesis and characterization of silver nanowires by polyol process. *Applied Nanoscience, 5*(7), 881-890.

Kupec, J., Stoop, R. L., & Witzigmann, B. (2010). Light absorption and emission in nanowire array solar cells. *Optics Express*, *18*(26), 27589-27605.

Kvítek, O., Siegel, J., Hnatowicz, V., & Švorčík, V. (2013). Noble metal nanostructures influence of structure and environment on their optical properties. *Journal of Nanomaterials, 2013*, 111.

Lagref, J.-J., Nazeeruddin, M. K., & Grätzel, M. (2008). Artificial photosynthesis based on dye-sensitized nanocrystalline TiO_2 solar cells. *Inorganica Chimica Acta, 361*(3), 735-745.

Langridge, R., & Gomatos, P. J. (1963). The structure of RNA. S*cience, 141*(3585), 1024-1024.

Lee, J. B., Hong, J., Bonner, D. K., Poon, Z., & Hammond, P. T. (2012). Self-assembled RNA interference microsponges for efficient siRNA delivery. *Nature Materials, 11*(4), 316.

Lee, W. J., Ramasamy, E., Lee, D. Y., & Song, J. S. (2008). Performance variation of carbon counter electrode based dye-sensitized solar cell. *Solar Energy Materials and Solar Cells, 92*(7), 814-818.

Léon, J. C., Stegemann, L., Peterlechner, M., Litau, S., Wilde, G., Strassert, C. A., & Müller, J. (2016). Formation of silver nanoclusters from a DNA template containing Ag (I)-mediated base pairs. *Bioinorganic Chemistry and Applications, 2016*.

Li, H., Guo, Y., & Robertson, J. (2015). Calculation of TiO2 surface and subsurface oxygen vacancy by the screened exchange functional. *The Journal of Physical Chemistry C, 119*(32), 18160-18166.

Li, Y., Shi, W., Gupta, A., & Chopra, N. (2015). Morphological evolution of gold nanoparticles on silicon nanowires and their plasmonics. *RSC Advances, 5*(61), 49708-49718.

Lim, S., Huang, N., Lim, H., & Mazhar, M. (2014). Aerosol assisted chemical vapour deposited (AACVD) of TiO_2 thin film as compact layer for dye-sensitised solar cell. *Ceramics International, 40*(6), 8045-8052.

Lim, S., Huang, N. M., Lim, H. N., & Mazhar, M. (2014). Surface modification of aerosol-assisted CVD produced TiO_2 thin film for dye sensitised solar cell. *International Journal of Photoenergy, 2014*.

Lin, C., Liu, Y., Rinker, S., & Yan, H. (2006). DNA Tile Based Self-Assembly: Building Complex Nanoarchitectures. *ChemPhysChem, 7*(8), 1641-1647.

Lin, L., Wang, W., Huang, J., Li, Q., Sun, D., Yang, X., Wang, Y. (2010). Nature factory of silver nanowires: Plant-mediated synthesis using broth of Cassia fistula leaf. *Chemical Engineering Journal, 162*(2), 852-858.

Lin, X., & Wang, S. (2005). Electrochemical generation of silver nanowires.

Lipfert, J., Doniach, S., Das, R., & Herschlag, D. (2014). Understanding nucleic acid–ion interactions. *Annual Review of Biochemistry, 83*, 813-841.

Liu, D., Gugliotti, L. A., Wu, T., Dolska, M., Tkachenko, A. G., Shipton, M. K., Feldheim, D. L. (2006). RNA-mediated synthesis of palladium nanoparticles on Au surfaces. *Langmuir, 22*(13), 5862-5866.

Liu, Q. (2014). Photovoltaic performance improvement of dye-sensitized solar cells based on Mg-doped TiO_2 thin films. *Electrochimica Acta, 129*, 459-462.

Liu, Z., Ren, Z., Liu, H., Sahraei, N., Lin, F., Stangl, R., Peters, I. M. (2017). A modeling framework for optimizing current density in four-terminal tandem solar cells: A case study on GaAs/Si tandem. *Solar Energy Materials and Solar Cells, 170*, 167-177.

López, R., & Gómez, R. (2012). Band-gap energy estimation from diffuse reflectance measurements on sol–gel and commercial TiO_2: a comparative study. *Journal of Sol-gel Science and Technology, 61*(1), 1-7.

Lott, P. F. (1968). Recent Instrumentation for UV-Visible Spectrophotometry-Part 1: Dual-Beam Spectrophotometers. *Journal of Chemical Education, 45*(3), A169.

Lu, L., Xia, X., Luo, J., & Shao, G. (2012). Mn-doped TiO_2 thin films with significantly improved optical and electrical properties. *Journal of Physics D: Applied Physics, 45*(48), 485102.

Lu, Y., Ganguli, R., Drewien, C. A., & Anderson, M. T. (1997). Continuous formation of supported cubic and hexagonal mesoporous films by sol-gel dip-coating. *Nature, 389*(6649), 364.

Ma, N., Dooley, C. J., & Kelley, S. O. (2006). RNA-templated semiconductor nanocrystals. *Journal of the American Chemical Society, 128*(39), 12598-12599.

Mabbott, G. A. (1983). An introduction to cyclic voltammetry. *Journal of Chemical Education, 60*(9), 697.

Maleki, K., Abdizadeh, H., Golobostanfard, M. R., & Adelfar, R. (2017). Hierarchical porous photoanode based on acid boric catalyzed sol for dye sensitized solar cells. *Applied Surface Science, 394*, 37-46.

Mäntele, W., & Deniz, E. (2017). UV–VIS absorption spectroscopy: Lambert-Beer reloaded. *Spectrochimica Acta Part A:Molecular an Biomolecular Spectroscopy*, 17(3), 965-968.

Mao, H., Feng, J., Ma, X., Wu, C., & Zhao, X. (2012). One-dimensional silver nanowires synthesized by self-seeding polyol process. *Journal of Nanoparticle Research, 14*(6), 887.

Marken, F., Neudeck, A., & Bond, A. M. (2010). Cyclic Voltammetry. In F. Scholz, A. M. Bond, R. G. Compton, D. A. Fiedler, G. Inzelt, H. Kahlert, Š. Komorsky-Lovrić, H. Lohse, M. Lovrić, F. Marken, A. Neudeck, U. Retter, F. Scholz & Z. Stojek (Eds.), *Electroanalytical Methods: Guide to Experiments and Applications*, 57-106

Martin, C. R. (1994). Nanomaterials: a membrane-based synthetic approach. S*cience*, 1961-1966.

Mikolajick, T., Heinzig, A., Trommer, J., Pregl, S., Grube, M., Cuniberti, G., & Weber, W. M. (2013). Silicon nanowires–a versatile technology platform. *physica status solidi (RRL)-Rapid Research Letters*, *7*(10), 793-799.

Miniewicz, A., Bartkiewicz, S., Orlikowska, H., & Dradrach, K. (2016). Marangoni effect visualized in two-dimensions Optical tweezers for gas bubbles. *Scientific Reports, 6, 34787*.

Mogilevsky, G., Borland, L., Brickhouse, M., & Fountain III, A. W. (2012). Raman spectroscopy for homeland security applications. *International Journal of Spectroscopy, 2012*.

Mohamed, H. D. A., Watson, S. M., Horrocks, B. R., & Houlton, A. (2012). Magnetic and conductive magnetite nanowires by DNA-templating. *Nanoscale, 4*(19), 5936-5945.

Monson, C. F., & Woolley, A. T. (2003). DNA-templated construction of copper nanowires. *Nano Letters, 3*(3), 359-363.

Moras, J. D., Strandberg, B., Suc, D., & Wilson, K. (1996). Semiconductor clusters, nanocrystals, and quantum dots. *Science, 271*, 933.

Movasaghi, Z., Rehman, S., & ur Rehman, D. I. (2008). Fourier transform infrared (FTIR) spectroscopy of biological tissues. *Applied Spectroscopy Reviews, 43*(2), 134-179.

Narayanan, R., & El-Sayed, M. A. (2004). Shape-dependent catalytic activity of platinum nanoparticles in colloidal solution. *Nano Letters, 4*(7), 1343-1348.

Neault, J., & Tajmir-Riahi, H. (1997). RNA− Aspirin Interaction Studied by FTIR Difference Spectroscopy. *The Journal of Physical Chemistry B, 101*(1), 114-116.

Nie, Z., Petukhova, A., & Kumacheva, E. (2010). Properties and emerging applications of self-assembled structures made from inorganic nanoparticles. *Nature Nanotechnology, 5*(1), 15-25.

Niu, Z., Liu, J., Lee, L. A., Bruckman, M. A., Zhao, D., Koley, G., & Wang, Q. (2007). Biological templated synthesis of water-soluble conductive polymeric nanowires. *Nano Letters, 7*(12), 3729-3733.

Ogino, K., Onoe, Y., Abe, M., Ono, H., & Bessho, K. (1990). Reduction of surface tension by novel polymer surfactants. *Langmuir, 6*(7), 1330-1330.

Ongaro, A., Griffin, F., Beecher, P., Nagle, L., Iacopino, D., Quinn, A., Fitzmaurice, D. (2005). DNA-templated assembly of conducting gold nanowires between gold electrodes on a silicon oxide substrate. *Chemistry of Materials, 17*(8), 1959-1964.

Park, S. H., Prior, M. W., LaBean, T. H., & Finkelstein, G. (2006). Optimized fabrication and electrical analysis of silver nanowires templated on DNA molecules. *Applied Physics Letters, 89*(3), 033901.

Pate, J., Zamora, F., Watson, S. M., Wright, N. G., Horrocks, B. R., & Houlton, A. (2014). Solution-based DNA-templating of sub-10 nm conductive copper nanowires. *Journal of Materials Chemistry C, 2*(43), 9265-9273.

Periasamy, V., Ciniciato, G. P., Yunus, K., & Fisher, A. C. (2015). Fabrication of capillary-force-induced DNA-templated Ag wires assisted by enzymatic etching. *Applied Physics Express, 8*(2), 027002.

Periasamy, V., Rizan, N., Al-Ta'ii, H. M. J., Tan, Y. S., Tajuddin, H. A., & Iwamoto, M. (2016). Measuring the Electronic Properties of DNA-Specific Schottky Diodes Towards Detecting and Identifying Basidiomycetes DNA. *Scientific Reports, 6*, 29879.

Periasamy, V., Rizan, N., Talebi, S. and Rajampour, M.N. (2016). RNA Profiling Device and Method, Patent Pending (PI 2017701978).

Poizot, P., Laruelle, S., Grugeon, S., Dupont, L., & Tarascon, J. (2000). Nano-sized transition-metal oxides as negative-electrode materials for lithium-ion batteries. *Nature, 407*(6803), 496.

Poralan Jr, G., Gambe, J., Alcantara, E., & Vequizo, R. (2015). X-ray diffraction and infrared spectroscopy analyses on the crystallinity of engineered biological hydroxyapatite for medical application. Paper presented at the IOP Conference Series: *Materials Science and Engineering.*

Pruneanu, S., Al-Said, S. A. F., Dong, L., Hollis, T. A., Galindo, M. A., Wright, N. G., Horrocks, B. R. (2008). Self-Assembly of DNA-Templated Polypyrrole Nanowires: Spontaneous Formation of Conductive Nanoropes. *Advanced Functional Materials, 18*(16), 2444-2454.

Qu, D., Zheng, M., Du, P., Zhou, Y., Zhang, L., Li, D., Sun, Z. (2013). Highly luminescent S, N co-doped graphene quantum dots with broad visible absorption bands for visible light photocatalysts. *Nanoscale, 5*(24), 12272-12277.

Rades, S., Hodoroaba, V.-D., Salge, T., Wirth, T., Lobera, M. P., Labrador, R. H., Unger, W. E. (2014). High-resolution imaging with SEM/T-SEM, EDX and SAM as a combined methodical approach for morphological and elemental analyses of single engineered nanoparticles. *RSC Advances, 4*(91), 49577-49587.

Ramasamy, E., & Lee, J. (2010). Ferrocene-derivatized ordered mesoporous carbon as high performance counter electrodes for dye-sensitized solar cells. *Carbon, 48*(13), 3715-3720.

Raphael, E., Jara, D. H., & Schiavon, M. A. (2017). Optimizing photovoltaic performance in $CuInS_2$ and CdS quantum dot-sensitized solar cells by using an agar-based gel polymer electrolyte. *RSC Advances, 7*(11), 6492-6500.

Reda, S., Khairy, M., & Mousa, M. (2017). Photocatalytic activity of nitrogen and copper doped TiO_2 nanoparticles prepared by microwave-assisted sol-gel process. *Arabian Journal of Chemistry,* (Corrected proof).

Reyes, D., Biziere, N., Warot-Fonrose, B., Wade, T., & Gatel, C. (2016). Magnetic configurations in Co/Cu multilayered nanowires: evidence of structural and magnetic interplay. *Nano Letters, 16*(2), 1230-1236.

Richter, J., Mertig, M., Pompe, W., Mönch, I., & Schackert, H. K. (2001). Construction of highly conductive nanowires on a DNA template. *Applied Physics Letters, 78*(4), 536-538.

Richter, J., Seidel, R., Kirsch, R., Mertig, M., Pompe, W., Plaschke, J., & Schackert, H. K. (2000). Nanoscale palladium metallization of DNA. *Nanoscale, 94*, 8720.

Roduner, E. (2006). Size matters: why nanomaterials are different. *Chemical Society Reviews, 35*(7), 583-592.

Saadeh, Y., & Vyas, D. (2014). Nanorobotic applications in medicine: Current proposals and designs. *American Journal of Robotic Surgery*, 1(1), 4-11.

Sathishkumar, M., Sneha, K., Won, S., Cho, C.-W., Kim, S., & Yun, Y.-S. (2009). Cinnamon zeylanicum bark extract and powder mediated green synthesis of nano-crystalline silver particles and its bactericidal activity. *Colloids and Surfaces B: Biointerfaces, 73*(2), 332-338.

Sato, H., Murakami, R., Zhang, J., Ozaki, Y., Mori, K., Takahashi, I., Noda, I. (2006). X-Ray diffraction and infrared spectroscopy studies on crystal and lamellar structure and CHO hydrogen bonding of biodegradable poly (hydroxyalkanoate). *Macromolecular Research, 14*(4), 408-415.

Satoh, N., Nakashima, T., & Yamamoto, K. (2013). Metastability of anatase: size dependent and irreversible anatase-rutile phase transition in atomic-level precise titania. *Scientific Reports, 3, 1959*.

Scharf, P., & Müller, J. (2013). Nucleic Acids With Metal-Mediated Base Pairs and Their Applications. *ChemPlusChem, 78*(1), 20-34.

Schurr, J. M., & Smith, S. B. (1990). Theory for the extension of a linear polyelectrolyte attached at one end in an electric field. *Biopolymers, 29*(8-9), 1161-1165.

Seeman, N. C. (1998). DNA nanotechnology: novel DNA constructions. *Annual Review of Biophysics and Biomolecular Structure, 27*(1), 225-248.

Seeman, N. C. (2005). From genes to machines: DNA nanomechanical devices. *Trends in Biochemical Sciences, 30*(3), 119-125.

Seo, C., Jang, D., Chae, J., & Shin, S. (2017). Altering the coffee-ring effect by adding a surfactant-like viscous polymer solution. *Scientific Reports, 7*(1), 500.

Shakir, S., Khan, Z. S., Ali, A., Akbar, N., & Musthaq, W. (2015). Development of copper doped titania based photoanode and its performance for dye sensitized solar cell applications. *Journal of Alloys and Compounds, 652*, 331-340.

Sigel, R. K. (2005). Group II intron ribozymes and metal ions–a delicate relationship. *European Journal of Inorganic Chemistry, 2005*(12), 2281-2292.

Sinden, R. R. (2012). DNA structure and function. *Academic Press*, 1, 108-135.

Smestad, G. P. (1998). Education and solar conversion:: demonstrating electron transfer. *Solar Energy Materials and Solar Cells, 55*(1), 157-178.

Smith, B. C. (2011). Fundamentals of Fourier transform infrared spectroscop*y*. *CRC Press, 2, 90-120.*

Smith, K., & Oatley, C. (1955). The scanning electron microscope and its fields of application. *British Journal of Applied Physics, 6*(11), 391.

Sohn, J. S., Kwon, Y. W., Jin, J. I., & Jo, B. W. (2011). DNA-templated preparation of gold nanoparticles. *Molecules, 16*(10), 8143-8151.

Song, J., Hwang, S., Park, S., Kim, T., Im, K., Hur, J., Park, N. (2016). DNA templated synthesis of branched gold nanostructures with highly efficient near-infrared photothermal therapeutic effects. *RSC Advances, 6*(57), 51658-51661.

Song, W., Gong, Y., Tian, J., Cao, G., Zhao, H., & Sun, C. (2016). Novel Photoanode for Dye-Sensitized Solar Cells with Enhanced Light-Harvesting and Electron-Collection Efficiency. *ACS Applied Materials & Interfaces, 8*(21), 13418-13425.

Sönmezoğlu, S., Arslan, A., Serin, T., & Serin, N. (2011). The effects of film thickness on the optical properties of TiO_2–SnO_2 compound thin films. *Physica Scripta, 84*(6), 065602.

Späth, M., Sommeling, P., Van Roosmalen, J., Smit, H., Van der Burg, N., Mahieu, D., Kroon, J. (2003). Reproducible manufacturing of dye-sensitized solar cells on a semi-automated baseline. *Progress in Photovoltaics: Research and Applications, 11*(3), 207-220.

Šponer, J. E., Burda, J. V., Leszczynki, J., & Šponer, J. (2006). Interaction of metal cations with Nucleic Acids and their building units. *Computational Studies of RNA and DNA*, 389-410.

Šponer, J. E., Špačková, N. a., Leszczynski, J., & Šponer, J. (2005). Principles of RNA base pairing: structures and energies of the trans Watson− Crick/sugar edge base pairs. *The Journal of Physical Chemistry B, 109*(22), 11399-11410.

Stanjek, H., & Häusler, W. (2004). Basics of X-ray Diffraction. *Hyperfine Interactions, 154*(1-4), 107-119.

Stoyanova, A., Hitkova, H., Bachvarova-Nedelcheva, A., Iordanova, R., Ivanova, N., & Sredkova, M. (2013). Synthesis and antibacterial activity of TiO_2/ZnO nanocomposites prepared via nonhydrolytic route. *Journal of Chemical Technology and Metallurgy, 48*(2), 154-161.

Suman, T., Rajasree, S. R., Ramkumar, R., Rajthilak, C., & Perumal, P. (2014). The Green synthesis of gold nanoparticles using an aqueous root extract of Morinda citrifolia L. *Spectrochimica Acta Part A: Molecular and Biomolecular Spectroscopy, 118*, 11-16.

Tachan, Z., Shalom, M., Hod, I., Rühle, S., Tirosh, S., & Zaban, A. (2011). PbS as a highly catalytic counter electrode for polysulfide-based quantum dot solar cells. *The Journal of Physical Chemistry C, 115*(13), 6162-6166.

Tang, Z., Wu, J., Zheng, M., Huo, J., & Lan, Z. (2013). A microporous platinum counter electrode used in dye-sensitized solar cells. *Nano Energy, 2*(5), 622-627.

Tanyi, A. R., Rafieh, A. I., Ekaneyaka, P., Tan, A. L., Young, D. J., Zheng, Z., Chandrakanthi, R. (2015). Enhanced efficiency of dye-sensitized solar cells based on Mg and La co-doped TiO_2 photoanodes. *Electrochimica Acta, 178*, 240-248.

Taton, T. A. (2003). Bio-nanotechnology: Two-way traffic. *Nature Materials, 2*(2), 73-74.

Tennakone, K., Kumara, G., Kottegoda, I., Wijayantha, K., & Perera, V. (1998). A solid-state photovoltaic cell sensitized with a ruthenium bipyridyl complex. *Journal of Physics D: Applied Physics, 31*(12), 1492.

Tissue, B. M. (2002). Ultraviolet and Visible Absorption Spectroscopy *Characterization of Materials*: John Wiley & Sons, Inc.

Tributsch, H., & Gerischer, H. (1969). The use of semiconductor electrodes in the study of photochemical reactions. *Berichte der Bunsengesellschaft Für Physikalische Chemie, 73*(8-9), 850-854.

Tsai, C.-C., Chu, Y.-Y., & Teng, H. (2010). A simple electrophoretic deposition method to prepare TiO_2–B nanoribbon thin films for dye-sensitized solar cells. *Thin Solid Films, 519*(2), 662-665.

Tsukamoto, R., Muraoka, M., Seki, M., Tabata, H., & Yamashita, I. (2007). Synthesis of CoPt and FePt3 nanowires using the central channel of tobacco mosaic virus as a biotemplate. *Chemistry of Materials, 19*(10), 2389-2391.

Van de Lagemaat, J., Park, N.-G., & Frank, A. (2000). Influence of electrical potential distribution, charge transport, and recombination on the photopotential and photocurrent conversion efficiency of dye-sensitized nanocrystalline TiO_2 solar cells: a study by electrical impedance and optical modulation techniques. *The Journal of Physical Chemistry B, 104*(9), 2044-2052.

Varghese, N., Mogera, U., Govindaraj, A., Das, A., Maiti, P. K., Sood, A. K., & Rao, C. (2009). Binding of DNA nucleobases and nucleosides with graphene. *ChemPhysChem, 10*(1), 206-210.

Veith, M., Bubel, C., & Zimmer, M. (2011). A novel precursor system and its application to produce tin doped indium oxide. *Dalton Transactions, 40*(22), 6028-6032.

Vengadesh, P., Ciniciato, G., Zhijian, C., Musoddiq, M., Fisher, A., & Yunus, K. (2015). Capillary force assisted fabrication of DNA templated silver wires. *RSC Advances, 5*(11), 8163-8166.

Wang, B., Chang, S., Lee, L. T. L., Zheng, S., Wong, K. Y., Li, Q., Chen, T. (2013). Improving pore filling of gel electrolyte and charge transport in photoanode for high-efficiency quasi-solid-state dye-sensitized solar cells. *ACS Applied Materials & Interfaces, 5*(17), 8289-8293.

Wang, G., Xu, L., Zhang, J., Yin, T., & Han, D. (2012). Enhanced photocatalytic activity of powders (P25) via calcination treatment. *International Journal of Photoenergy, 2012*.

Wang, H., & Hu, Y. H. (2012). Graphene as a counter electrode material for dye-sensitized solar cells. *Energy & Environmental Science, 5*(8), 8182-8188.

Wang, N., Cai, Y., & Zhang, R. (2008). Growth of nanowires. *Materials Science and Engineering: R: Reports, 60*(1), 1-51.

Wang, Z. L., & Song, J. (2006). Piezoelectric nanogenerators based on zinc oxide nanowire arrays. *Science*, *312*(5771), 242-246.

Watson, J., & Crick, F. (1993). Molecular structure of nucleic acids: a structure for deoxyribose nucleic acid. *JAMA, 269*(15), 1966-1967.

Watson, J. D. (2008). Molecular biology of the gene, *Pearson,* 7, 55-160.

Watson, S. M., Wright, N. G., Horrocks, B. R., & Houlton, A. (2009). Preparation, characterization and scanned conductance microscopy studies of DNA-templated one-dimensional copper nanostructures. *Langmuir, 26*(3), 2068-2075.

Weber, K., & Osborn, M. (1969). The reliability of molecular weight determinations by dodecyl sulfate-polyacrylamide gel electrophoresis. *Journal of Biological Chemistry, 244*(16), 4406-4412.

Weerasinghe, H. C., Huang, F., & Cheng, Y.-B. (2013). Fabrication of flexible dye sensitized solar cells on plastic substrates. *Nano Energy, 2*(2), 174-189.

Weisspfennig, C. T., Hollman, D. J., Menelaou, C., Stranks, S. D., Joyce, H. J., Johnston, M. B., Herz, L. M. (2014). Dependence of Dye Regeneration and Charge Collection on the Pore-Filling Fraction in Solid-State Dye-Sensitized Solar Cells. *Advanced Functional Materials, 24*(5), 668-677.

Whelan, D. R., Bambery, K. R., Heraud, P., Tobin, M. J., Diem, M., McNaughton, D., & Wood, B. R. (2011). Monitoring the reversible B to A-like transition of DNA in eukaryotic cells using Fourier transform infrared spectroscopy. *Nucleic Acids Research, 39*(13), 5439-5448.

Willett, E. (2004). The Basics of Quantum Physics: Understanding the Photoelectric Effect and Line Spectr*a*: *Rosen Publishing Group, 4-48*.

William A. Vallejo L., C. A. Q. o. S. a. J. A. H. S., Prof. Leonid A. Kosyachenko (Ed.). (2011). *The Chemistry and Physics of Dye-Sensitized Solar Cells, a chapter in Solar Cells - Dye-Sensitized Devices* (Vol. ISBN: 978-953-307-735-2, InTech).

Winnacker, E.-L. (1978). Adenovirus DNA: structure and function of a novel replicon. *Cell, 14*(4), 761-773.

Xu, M., Xia, D., & Sheng, Y. (2006). Thin-film solar cells. *Material Review, 20*(9), 109-111.

Yan, J., Wu, G., Guan, N., Li, L., Li, Z., & Cao, X. (2013). Understanding the effect of surface/bulk defects on the photocatalytic activity of TiO_2: anatase versus rutile. *Physical Chemistry Chemical Physics, 15*(26), 10978-10988.

Yum, J.-H., Kim, S.-S., Kim, D.-Y., & Sung, Y.-E. (2005). Electrophoretically deposited TiO_2 photo-electrodes for use in flexible dye-sensitized solar cells. *Journal of Photochemistry and Photobiology A: Chemistry, 173*(1), 1-6.

Yunker, P. J., Still, T., Lohr, M. A., & Yodh, A. (2011). Suppression of the coffee-ring effect by shape-dependent capillary interactions. *Nature, 476*(7360), 308-311.

Zalas, M., & Klein, M. (2012). The Influence of Titania Electrode Modification with Lanthanide Ions Containing Thin Layer on the Performance of Dye-Sensitized Solar Cells. *International Journal of Photoenergy, 2012*.

Zeng, J., Zhang, Q., Chen, J., & Xia, Y. (2009). A comparison study of the catalytic properties of Au-based nanocages, nanoboxes, and nanoparticles. *Nano Letters, 10*(1), 30-35.

Zhou, J., Yu, L., Liu, W., Zhang, X., Mu, W., Du, X., ... & Deng, Y. (2015). High performance all-solid supercapacitors based on the network of ultralong manganese dioxide/polyaniline coaxial nanowires. *Scientific Reports*, *5*, 17858.

Zucchiatti, P., Mitri, E., Kenig, S. a., Billè, F., Kourousias, G., Bedolla, D. E., & Vaccari, L. (2016). Contribution of Ribonucleic Acid (RNA) to the Fourier Transform Infrared (FTIR) Spectrum of Eukaryotic Cells. *Analytical Chemistry, 88*(24), 12090-12098.

LIST OF PUBLICATIONS AND PAPERS PRESENTED

Published Papers

1. **Shakir, S**., Saravanan, J., Rizan, N., Babu, K. J., Aziz, M. A., Moi, P. S., Periasamy, V., & Kumar, G. G. (2017). Fabrication of capillary force induced DNA template Ag nanopatterns for sensitive and selective enzyme-free glucose sensors. *Sensors and Actuators B: Chemical*, 256, 820-827.

2. **Shakir. S.**, Yiing Y. F., Rizan. N., Abd-ur-Rehman, H. M., Yunus, K., Moi P. S., Periasamy,V. (2017). Electro-catalytic and structural studies of DNA templated gold wires on platinum/ITO as modified counter electrode in dye sensitized solar cells, *Journal of Material Science;Materials in Electronics*, 29(6), 4602-4611.

3. **Shakir. S.**, Abd-ur-Rehman, H.M., Yunus, K., Moi P.S., Iwamoto, M., Periasamy, V. (2018). Fabrication of un-doped and magnesium doped TiO_2 films by aerosol assisted chemical vapor deposition for dye sensitized solar cells, *Journal of Alloys and Compounds*, 737, 740-747.

Conference Papers Presented

1. **Shakir, S**., Yunus, K., Vengadesh, P. (2017), Electrochemical properties of RNA templated Au nanowires to be used as a counter electrode in dye sensitized solar cells. *6th international Conference on Functional Materials and Devices*, 2017 (ICFMD-2017), 15-18 August 2017, Bayview Hotel, Melaka, Malaysia.